Walther Meißner Institut
Bayerische Akademie der Wissenschaften
Technische Universität München

Magnon-phonon interactions in ferromagnetic thin films

Mathias Weiler

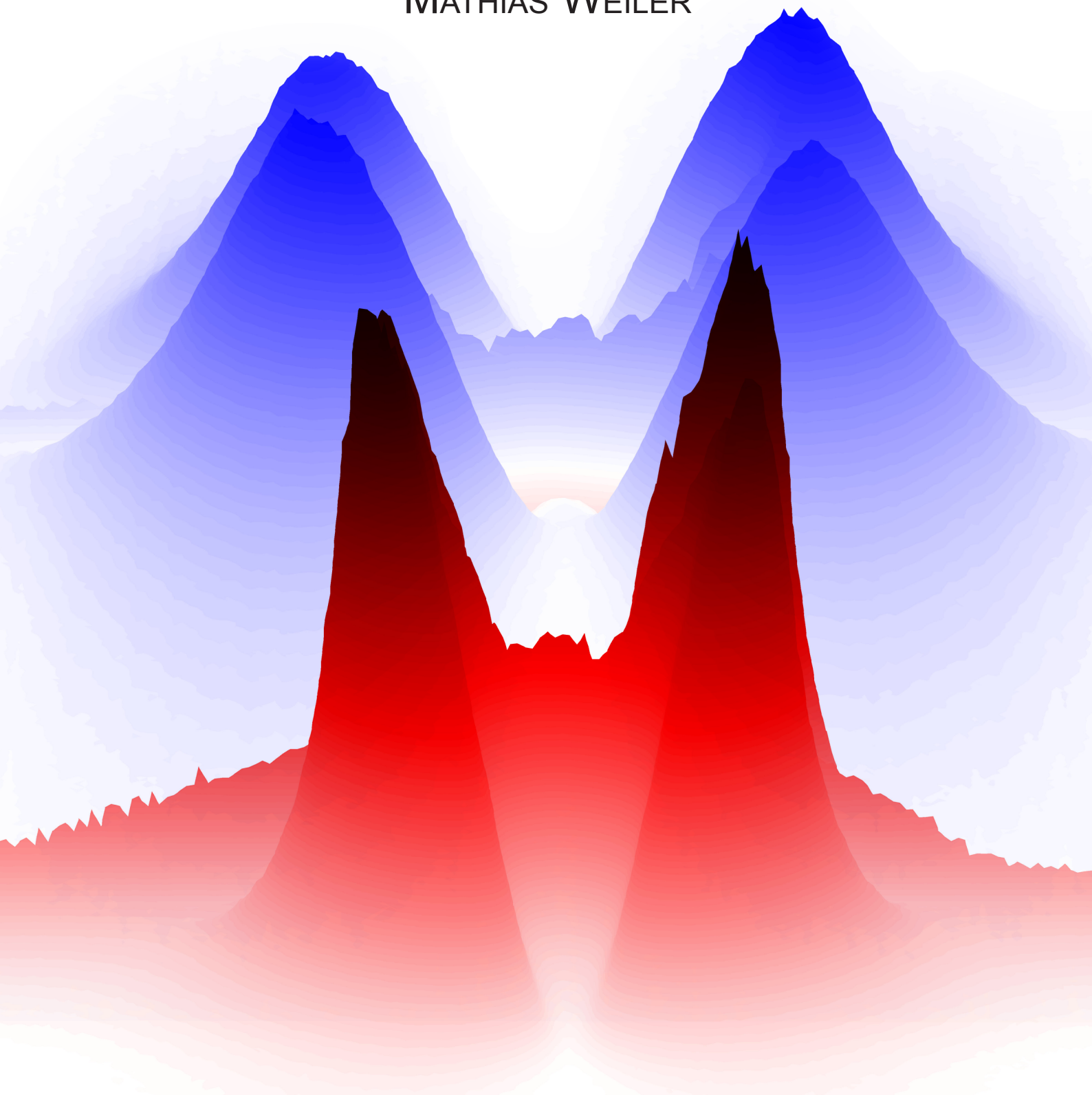

TECHNISCHE UNIVERSITÄT MÜNCHEN

Lehrstuhl E23 für Technische Physik

Walther-Meißner-Institut für Tieftemperaturforschung
der Bayerischen Akademie der Wissenschaften

Magnon-phonon interactions in ferromagnetic thin films

Mathias Weiler

Vollständiger Abdruck der von der Fakultät für Physik der Technischen Universität München zur Erlangung des akademischen Grades eines

Doktors der Naturwissenschaften

genehmigten Dissertation.

Vorsitzender:		Univ.-Prof. Dr. H. Friedrich
Prüfer der Dissertation:	1.	Univ.-Prof. Dr. R. Gross
	2.	apl. Prof. Dr. M. S. Brandt

Die Dissertation wurde am 22.03.2012 bei der Technischen Universität München eingereicht und durch die Fakultät für Physik am 25.05.2012 angenommen.

to Astrid and Reto

Abstract

Today's electronic devices rely on electric charge in order to transport, process and store data. However, the storage density and processing speed of charge-based electronics are rapidly approaching fundamental limits due to Joule heating. This issue could be overcome using information technology concepts that are based on spin and heat currents. Such concepts thus are are vigorously sought after in the emerging field of spin caloritronics.

This thesis is concerned with a particularly promising spin caloritronic approach centered around the interaction of magnons and phonons for spin current generation. We experimentally demonstrate resonant magnon-phonon interaction in the GHz frequency range by studying the magnetoelastically driven magnetization precession induced by a sound wave in ferromagnetic thin films at room temperature.

Our findings open the path for the investigation of angular momentum transport driven by acoustic phonons. In particular, we experimentally demonstrate that pure spin currents can be generated by the resonant interaction of magnons and coherent phonons. This establishes resonant acoustic spin pumping as a novel means for spin current generation.

Finally, we show that thermal phonons generated in spatially confined temperature gradients can be used to convey angular momentum in ferromagnetic thin films. Our experiments demonstrate that the local charge and/or spin currents that arise due to the anomalous Nernst and spin Seebeck effects depend on the local magnetization configuration. This establishes magnetothermal imaging of magnetic texture as well as local, bipolar, magnetically controlled charge and spin current sources.

Kurzfassung

Die heutige Informationstechnologie basiert auf dem Transport, der Verarbeitung und der Speicherung von elektrischer Ladung. Die dabei erreichbaren Speicherdichten und Verarbeitungsgeschwindigkeiten sind durch Ohmsche Verluste fundamental begrenzt. Neuartige Technologien, die auf Wärme- und Spinströmen basieren, könnten diese Grenze umgehen und werden daher im Forschungsfeld der "Spin Caloritronics" erforscht.

Diese Arbeit beschäftigt sich mit dem dahingehend besonders vielversprechenden Ansatz der Kopplung von Magnonen und Phononen zur Spinstromerzeugung. Wir weisen diese Kopplung im GHz-Bereich experimentell nach, indem wir die schallwelleninduzierte Magnetisierungsdynamik in einem ferromagnetischen Dünnfilm bei Raumtemperatur untersuchen.

Darauf basierend demonstrieren wir experimentell, dass diese resonante Magnon-Phonon Kopplung dazu genutzt werden kann, einen akustisch getriebenen reinen Spinstrom von einem Ferromagneten in ein Normalmetall zu induzieren.

Schließlich untersuchen wir die Ladungs- und Spinströme, die durch thermische Phononen in lokalen Temperaturgradienten in ferromagnetischen Dünnfilmen erzeugt werden. Unsere experimentellen Ergebnisse zeigen, dass diese lokalen Ströme, die durch den anomalen Nernst- und den Spin-Seebeck-Effekt entstehen, von der lokalen Magnetisierung abhängen. Wir etablieren damit ein neuartiges magnetothermisches Abbildungsverfahren, sowie lokale, bipolare, magnetisch kontrollierbare Ladungs- und Spinstromquellen.

Contents

List of Figures

Introduction

The discovery of the electric battery as a voltage source by Alessandro Volta in 1800 [1] sparked the vigourous investigation of galvanic processes. In 1827, Georg Simon Ohm established the relation between voltage and electric current [2] and in 1865, James Clerk Maxwell's theory [3] unified magnetism and electricity. Electricity had entered and revolutionized everyday's life by the beginning of the 20^{th} century.

With the availability of electric currents, the foundation of modern computer technology was established by the invention of the transistor by Shockley, Bardeen and Brattain who were awarded the Nobel Prize in Physics for their discovery in 1956. Ever since, the rapid progression of information processing technology has been a fundamental cornerstone of the modern age. However, as the transistor size in today's computer processors is approaching the physical limit, Joule heat due to dissipative charge currents is becoming an increasing problem. Thus, future concepts for computer technology are presently vigorously sought after.

A promising approach thereby is based on exploiting the electron spin degree of freedom - rather than its charge - to process data. Pure spin currents, i.e., a directed flow of angular momentum, are predicted to be dissipationless [4]. In analogy to the electric battery as a charge current source, a source of pure spin currents could again revolutionize today's technology by enabling the transition from electronics to spintronics. In the present understanding of spin current generation schemes, the relaxation of collectively excited magnetic moments (Chapter 2) and thermal gradients in ferromagnetic media (Chapter 3) appear to be promising candidates for spin current sources.

The field of spintronics is however not limited to the investigation of spin currents. It rather includes a broad range of interactions of spin and electronic properties. In this context, the macroscopic ordering of magnetic moments in ferromagnetic materials provides a viable foundation for applications and fundamental research. For instance, the discovery of the giant magnetoresistance (GMR) by Peter Grünberg [5] and Albert Fert [6] was awarded with the Nobel Prize in 2007 for making today's magnetic data

storage technology possible. The GMR is observed in thin-film structures composed of alternating ferromagnetic and non-magnetic layers, where the manipulation of the relative magnetization orientations of the ferromagnetic constituents results in a giant change of the multilayer's electrical resistivity.

An important field in magnetism deals with magnetization orientation control schemes for applications in such multifunctional magnetic structures. A key goal thereby is to achieve a control of magnetic degrees of freedom via non-magnetic parameters. In particular, an electric field control of the magnetization offers intriguing perspectives for novel spintronic devices. To realize such a control scheme, a coupling of the magnetic ordering parameter to the electric field is necessary. While this is difficult to achieve in single-phase multiferroic materials [7], one can exploit a combination of the piezoelectric and the magnetoelastic effect for a strain-mediated electric field control of magnetization in piezoelectric/ferromagnetic bilayers.

This "spin-mechanical" approach is well established in the limit of a static elastic deformation [8–13] and even applicable to systems of uncoupled electron spins [14,15]. However, for possible applications of spin-mechanical devices, the investigation of radio frequency magnon-phonon interactions (Chapter 1) is fundamentally important to allow for fast processing speeds.

Taken together, magnon-phonon interaction phenomena may pave the way for future spintronic devices by providing versatile methods for spin current generation and magnetization orientation control schemes.

This thesis aims to provide an experimental approach towards a fundamental understanding of the interaction of magnons and phonons and is organized as follows:

In Chapter 1, a resonant excitation of magnetic moments, or magnons, is demonstrated via the coherent phonons of an acoustic wave. We provide unambiguous experimental evidence for this acoustically driven ferromagnetic resonance (FMR) and quantitatively model our results in a modified magnetoelastic Landau-Lifshitz-Gilbert approach. In our experiments, we inject surface acoustic waves (SAWs) into ferromagnetic thin films. We discuss the generation and detection of SAWs in piezoelectric crystals by means of interdigital transducers. The fabrication of our piezoelectric substrate / ferromagnetic thin film hybrid samples and the experimental setup are introduced. We demonstrate the actual launching and detection of SAWs in an acoustic delay line and their separation from spurious electromagnetic crosstalk and triple

transit signals in the time domain. The measurement results obtained by recording the SAW transmission through ferromagnetic thin films as a function of the external magnetic field magnitude and orientation are discussed. A phenomenological model of the acoustically driven FMR observed in the experiments is derived and a quantitative comparison of simulation and experimental data is performed.

In Chapter 2, we show that a pure spin current can be generated by resonant magnon-phonon interaction. An overview of the fundamental physical concepts involved in this acoustic spin pumping is given: We discuss spin pumping as a general phenomenon and the spin Hall effect and its inverse for spin current detection. We experimentally demonstrate the time-resolved detection of spin currents pumped by the insertion of a SAW into a Co/Pt thin film bilayer. Thereby, we separate photon and phonon-driven contributions to the measurands in the time domain. The experimental data obtained as a function of the external in-plane magnetic field magnitude and orientation are discussed and we find conclusive evidence for resonant spin current generation. Calculations based on models that represent the present understanding of the spin pumping effect are performed and reveal that we indeed observe elastically driven spin pumping.

In Chapter 3, we investigate spin and charge currents generated by a non-resonant interaction of magnons and thermal phonons using a spatially resolved technique. We discuss the magnetothermal control of charge and spin degrees of freedom in conductive ferromagnets and insulating ferromagnet / normal metal hybrids. In our experiments, we use the thermal gradient due to a scannable laser beam and an externally applied magnetic field to investigate local and integral magnetothermal charge and spin current generation. The thermal gradients induced into the thin film samples are calculated and we derive the anomalous Nernst and spin Seebeck coefficients of the investigated samples.

Finally, the obtained experimental results are summarized and put into a broad perspective. In the outlook, we encourage further investigation of magnon-phonon coupling in a set of experimental approaches that, amongst other things, consolidate the concepts for resonant and non-resonant magnon-phonon interactions discussed in this thesis.

Chapter 1

Phonon-driven magnetization dynamics

Below the Curie temperature, ferromagnetic media exhibit a spontaneous ordering of magnetic moments, resulting in a macroscopic magnetization. The resonant precession of this magnetization around an effective magnetic field can be driven by microwave photons. This interaction of coherent photons with collective magnetic excitations is termed ferromagnetic resonance (FMR). FMR is a fundamental and well established principle of solid state physics and provides a powerful tool for the investigation of magnetic anisotropy and magnetic damping [16–25]. We here show that the concept of FMR is not limited to the interaction of microwave *photons* and magnons. Rather, also microwave *phonons* can be used to all-elastically drive FMR. We exploit surface acoustic waves (SAWs) as a source of coherent microwave phonons and investigate the interaction of this SAWs with ferromagnetic thin films. This radio frequency (rf) magnetoelastic interaction has been studied predominantly on theoretical grounds to date [26–29], while experimental evidence for acoustically driven FMR has proven elusive [30] in previous experiments with acoustic waves and ferromagnets [31–35]. Here, a detailed study of the magneto-transmission of a SAW propagating at a ferroelectric/ferromagnetic interface is performed. In our room-temperature experiments in a $LiNbO_3$/Ni heterostructure, we can unambiguously identify acoustically driven FMR at SAW frequencies ranging from 860 MHz to 2.24 GHz. Using a modified Landau-Lifshitz-Gilbert approach, the SAW magnetotransmission is quantitatively simulated and excellent agreement between experiments and theory is found. Our results open intriguing perspectives for the investigation of magnon-phonon interactions. In particular, the acoustic FMR enables studies of the magnonic and phononic dispersions,

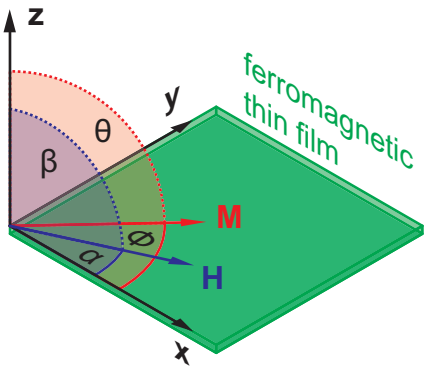

Figure 1.1: Cartesian coordinate system $\{\boldsymbol{x}, \boldsymbol{y}, \boldsymbol{z}\}$ with respect to a ferromagnetic thin film with magnetization $\boldsymbol{M}$ oriented at an angle ϕ to the $\boldsymbol{x}$ axis and θ to the $\boldsymbol{z}$ axis. An external magnetic field $\boldsymbol{H}$ is applied at an angle α to the $\boldsymbol{x}$ axis and β to the $\boldsymbol{z}$ axis.

of the anticrossing of these branches and mechanical spin pumping [36]. A concise report of the key results presented in this chapter was published in Ref. [37].

1.1 Magnetoelastic magnetization dynamics

We start by giving a brief introduction to phonon-driven magnetization dynamics in this section. In a free energy approach, the magnetoelastic FMR driving field is derived. We investigate the anisotropy of this driving field with respect to the magnetization orientation to identify the characteristic fingerprint of acoustically driven FMR.

Consider a ferromagnetic thin film with saturation magnetization M_s in a cartesian coordinate system $\{\boldsymbol{x}, \boldsymbol{y}, \boldsymbol{z}\}$ with $\boldsymbol{z}$ pointing along the thin film normal as shown in Fig. 1.1. The magnetization $\boldsymbol{M}$ is oriented at an angle ϕ to the $\boldsymbol{x}$ axis and at an angle θ to the $\boldsymbol{z}$ axis, while an external magnetic field $\boldsymbol{H}$ can be applied at an angle α to the $\boldsymbol{x}$ axis and an angle β to the $\boldsymbol{z}$ axis. The equilibrium orientation $\{\phi_0, \theta_0\}$ of $\boldsymbol{M}$ can be calculated by minimizing the thin film's magnetic free energy density. We divide the magnetic free energy density by M_s which - for a uniaxial polycrystalline thin film - yields the total anisotropy field [38]:

$$F^\mathrm{DC} = -\mu_0 \boldsymbol{H} \cdot \boldsymbol{m} + B_\mathrm{d} m_z^2 + B_\mathrm{u} (\boldsymbol{u} \cdot \boldsymbol{m})^2 \,, \tag{1.1}$$

where $\boldsymbol{m} = \{m_x, m_y, m_z\} = \boldsymbol{M}/M_\mathrm{s}$ is the magnetization orientation. B_u is a uniaxial

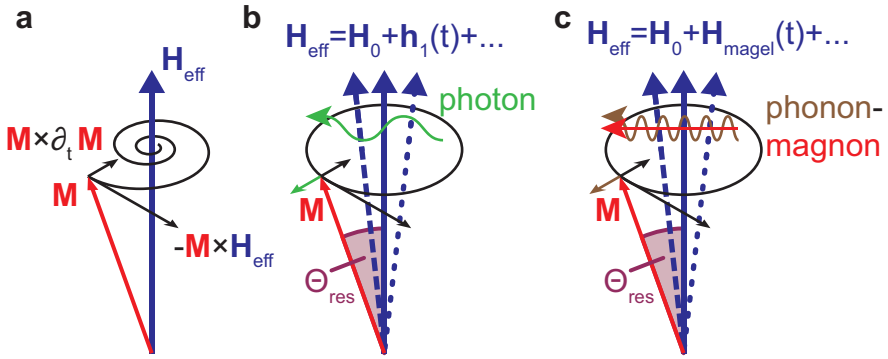

Figure 1.2: **a** The magnetization $\boldsymbol{M}$ precesses around the effective magnetic field $\boldsymbol{H}_{\text{eff}}$. **b** Photon-driven ferromagnetic resonance. **c** Phonon-driven ferromagnetic resonance

in plane anisotropy field along $\boldsymbol{u} = \{u_x, u_y, 0\}$ and B_{d} is the anisotropy field along the film normal, the main contribution of which is the demagnetization field $\mu_0 \frac{M_{\text{s}}}{2}$. In equilibrium, the magnetization $\boldsymbol{M}$ is aligned along the energetically most favorable direction which can be found by minimizing F^{DC} with respect to $\boldsymbol{M}$ orientation.

One can now define an effective magnetic field [39, 40]

$$\mu_0 \boldsymbol{H}_{\text{eff}} = -\nabla_{\boldsymbol{m}} F^{\text{DC}} = \mu_0 \left(\boldsymbol{H} + \boldsymbol{H}_{\text{aniso}} \right) \ , \tag{1.2}$$

so that $\boldsymbol{M} \parallel \boldsymbol{H}_{\text{eff}}$ in equilibrium. Here, $\boldsymbol{H}_{\text{aniso}}$ is a purely virtual anisotropy field while $\boldsymbol{H}$ is the real, externally applied magnetic field. With Eq. (1.1) we can now calculate the effective magnetic field and equilibrium orientation $\{\phi_0, \theta_0\}$ of $\boldsymbol{M}$ for any anisotropy and external magnetic field configuration. In the context of this thesis, we are however interested not only in the equilibrium orientation of $\boldsymbol{M}$ but rather in magnetization dynamics. Starting from a non-equilibrium state with a finite angle enclosed by $\boldsymbol{M}$ and $\boldsymbol{H}_{\text{eff}}$, the time-evolution of the magnetization direction $\boldsymbol{m}$ is described by its classical equation of motion, the Landau-Lifshitz-Gilbert equation [41, 42]:

$$\partial_t \boldsymbol{m} = -\gamma \boldsymbol{m} \times \mu_0 \boldsymbol{H}_{\text{eff}} + a \boldsymbol{m} \times \partial_t \boldsymbol{m} \ . \tag{1.3}$$

Here, $a > 0$ is a dimensionless damping parameter and $\gamma = g\mu_{\text{B}}/\hbar$ is the gyromagnetic ratio. With the Bohr magneton μ_{B} and $\hbar$ being the Planck constant divided by 2π, γ is a material constant with the g-factor $g \approx 2$ for the elemental ferromagnets. Solving the Landau-Lifshitz-Gilbert equation (LLG) yields a precessional motion of

$\boldsymbol{M}$ around $\boldsymbol{H}_{\text{eff}}$, the angular frequency ω_{res} of which is given by

$$\omega_{\text{res}} = \gamma\mu_0 H_{\text{eff}} \ . \tag{1.4}$$

One finds, that for typical effective magnetic fields in the range $10\,\text{mT} \leq \mu_0 H_{\text{eff}} \leq 1\,\text{T}$, $\nu_{\text{res}} = \omega_{\text{res}}/2\pi$ is in the GHz frequency regime. This precessional motion is described by the first term in Eq. (1.3) and is illustrated in Fig. 1.2a. Furthermore it can be seen from Fig. 1.2a that the term proportional to a describes a damping of this precession that causes $\boldsymbol{M}$ to be aligned parallel to $\boldsymbol{H}_{\text{eff}}$ in equilibrium. So far, the LLG describes the evolution of $\boldsymbol{m}$ as a function of time in the absence of an external driving force. Such a driving force can be applied to counteract the damping and to eventually cause a resonant precessional motion of $\boldsymbol{M}$ around $\boldsymbol{H}_{\text{eff}}$. Conventionally, this so called ferromagnetic resonance (FMR) is achieved by applying an external time dependent magnetic field $\boldsymbol{h}_1(t)$, so that Eq (1.2) becomes

$$\mu_0 \boldsymbol{H}_{\text{eff}}(t) = \mu_0 \left(\boldsymbol{H}_0 + \boldsymbol{H}_{\text{aniso}} + \boldsymbol{h}_1(t)\right) \ . \tag{1.5}$$

From the geometry of the cross product illustrated in Fig. 1.2a, it can be seen that $\boldsymbol{h}_1$ needs to be orthogonal to $\boldsymbol{H}_{\text{eff}}$ to counteract the damping and thus enable ferromagnetic resonance. In conventional FMR studies, $\boldsymbol{h}_1(t) = \boldsymbol{h}_1 \cos(\omega t)$ is provided by the magnetic field of microwave photons. Ferromagnetic resonance is observed for $\omega = \omega_{\text{res}}$ (cf. Eq. (1.4)). This photon-driven FMR is schematically depicted in Fig. 1.2b, and describes a precessional motion of $\boldsymbol{m}$ around $\boldsymbol{H}_{\text{eff}}(t)$ with a static, finite precession cone angle Θ_{res}. FMR has found widespread applications to investigate magnetic anisotropy ($\boldsymbol{H}_{\text{aniso}}$ in Eq. (1.2)) and magnetic damping (a in Eq. (1.3)) in ferromagnetic media [16–25]. From a fundamental physics point of view, FMR constitutes a resonantly coupled photon-magnon interaction.

We now proceed to show that FMR can not only be driven by *photons* but as well by *phonons*. To this end, $\boldsymbol{h}_1$ in Eq. (1.5) is replaced by a magnon-phonon effective field $\boldsymbol{H}_{\text{magel}}$ that drives the FMR as illustrated in Fig. 1.2c. To achieve phonon-magnon coupling, we exploit the fact that in most ferromagnetic media, lattice distortion described by the strain tensor $\hat{\boldsymbol{\varepsilon}}$ is linked to magnetic anisotropy. This phenomenon is called magnetoelasticity or inverse magnetostriction [38]. In the static limit, magnetoelasticity is known to provide a tool for magnetization orientation control in various ferromagnetic materials [7–13]. This spin-mechanical interaction prevails at radio fre-

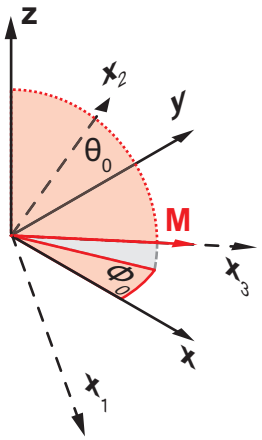

Figure 1.3: Coordinate system transformation to $\{\boldsymbol{x}_1, \boldsymbol{x}_2, \boldsymbol{x}_3\}$, where $\boldsymbol{x}_3$ points along the $\boldsymbol{m}$ equilibrium orientation ϕ_0 found from minimizing the F^{DC} contour (Eq. (1.1)) in the film plane (green).

quencies (rf), so that magnonic and phononic degrees of freedom become coupled, as discussed theoretically in Refs. [26–29]. While both, shear and pure strains, give rise to magnetoelastic phenomena, we will restrain the discussion to pure strains in this section for illustrative purposes. We thus only consider the diagonal elements of the strain tensor $\hat{\boldsymbol{\varepsilon}}$ and depict these by the vector $\boldsymbol{\varepsilon}$. Assuming a time-dependent pure strain $\boldsymbol{\varepsilon}(t)$, magnetoelasticity yields an additional, time-dependent contribution to the anisotropy field F^{DC} introduced in Eq. (1.1). For simplicity of the following calculations, we assume $\boldsymbol{\varepsilon} = \{\varepsilon_x, 0, 0\} \parallel \boldsymbol{x}$ without loss of generality. Furthermore, it is advantageous to use a cartesian coordinate system $\{x_1, x_2, x_3\}$ where x_3 is aligned along the $\boldsymbol{m}$ equilibrium orientation $\{\phi_0, \theta_0\}$ as illustrated in Fig. 1.3. This frame of reference is related to the coordinate system shown in Fig. 1.1 by

$$\begin{pmatrix} x \\ y \\ z \end{pmatrix} = \begin{pmatrix} \cos\theta_0 \cos\phi_0 & -\sin\phi_0 & \sin\theta_0 \cos\phi_0 \\ \cos\theta_0 \sin\phi_0 & \cos\phi_0 & \sin\theta_0 \sin\phi_0 \\ -\sin\theta_0 & 0 & \cos\theta_0 \end{pmatrix} \cdot \begin{pmatrix} x_1 \\ x_2 \\ x_3 \end{pmatrix}, \tag{1.6}$$

where x_2 is in the film plane ($\boldsymbol{xy}$ plane).

In this coordinate system, the magnetoelastic AC contribution to the anisotropy

field is given by [38]:

$$\begin{aligned} F^{\mathrm{AC}}(t) &= B_1 \varepsilon_x(t) m_x^2 \\ &= B_1 \varepsilon_x(t) \left(\cos\theta_0 \cos\phi_0 m_1 - \sin\phi_0 m_2 + \sin\theta_0 \cos\phi_0 m_3\right)^2 \ , \end{aligned} \tag{1.7}$$

where $m_3 \approx 1$ while m_1 and m_2 are small deviations from equilibrium and B_1 is the magnetoelastic coupling constant [38]. Hence, acoustically driven FMR can be observed in materials with $B_1 \neq 0$. Here, only the magnetoelastic coupling constant for cubic symmetry [38] and the pure strain ε_x are considered for simplicity. The AC driving field for acoustically driven FMR is given by

$$\mu_0 \boldsymbol{H}_{\mathrm{magel}}(t) = -\nabla_{\boldsymbol{m}} F^{\mathrm{AC}}(t) \ . \tag{1.8}$$

Now, this driving field needs to be evaluated to find its components perpendicular to $\boldsymbol{H}_{\mathrm{eff}}$, as only these contribute to FMR as discussed before (cf. Fig. 1.2). Due to the geometry of the coordinate system used in Eq. (1.7), the relevant contributions are those found for $-\nabla_{m_1,m_2} F^{\mathrm{AC}}$, which for evaluation at $\boldsymbol{m} = \{m_1 = 0, m_2 = 0, m_3 = 1\}$ yields:

$$\begin{aligned} \mu_0 H_{\mathrm{magel},1}(t) &= -2 B_1 \varepsilon_x(t) \sin\theta_0 \cos\theta_0 \cos^2\phi_0 \\ \mu_0 H_{\mathrm{magel},2}(t) &= 2 B_1 \varepsilon_x(t) \sin\theta_0 \cos\phi_0 \sin\phi_0 \ . \end{aligned} \tag{1.9}$$

With this expression we have derived a rf magnetoelastic field which in the case of acoustically driven FMR replaces the conventionally used rf electromagnetic field $\boldsymbol{h}_1(t)$. We now can write the total effective magnetic field for magnetoelastic excitation as:

$$\mu_0 \boldsymbol{H}_{\mathrm{eff}}(t) = \mu_0 \left(\boldsymbol{H}_0 + \boldsymbol{H}_{\mathrm{aniso}} + \boldsymbol{H}_{\mathrm{magel}}(t)\right) \ , \tag{1.10}$$

an expression which can be formally treated analogous to Eq. (1.5) when solving the LLG. However, while $\boldsymbol{h}_1$ is a real, externally applied magnetic field, $\boldsymbol{H}_{\mathrm{magel}}$ is an internal, virtual anisotropy field due to magnetoelastic phonon-magnon interaction. This has far-reaching consequences as, in particular, the driving field $\boldsymbol{H}_{\mathrm{magel}}$ is a function of both, strain $\boldsymbol{\varepsilon}$ and magnetization orientation $\boldsymbol{m}$. Hence, in phonon-driven FMR, the driving field $\boldsymbol{H}_{\mathrm{magel}}$ itself already stems from a coupling of phonons and magnons.

To establish a qualitative picture of such a magnetoelastic drive, we again assume

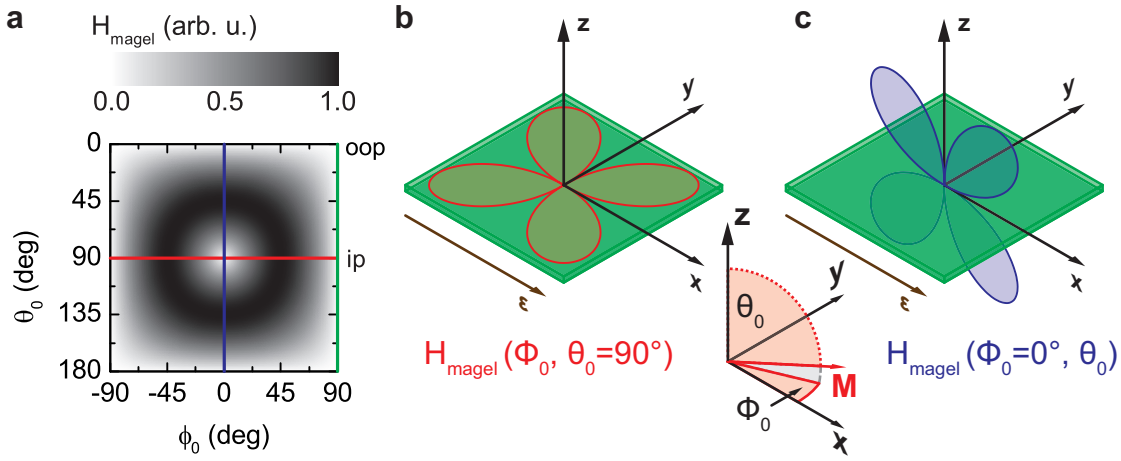

Figure 1.4: **a** H_{magel} as a function of the equilibrium $\boldsymbol{M}$ orientation $\{\phi_0, \theta_0\}$ for $\boldsymbol{\varepsilon} \parallel \boldsymbol{x}$. **b** H_{magel} for rotation of $\boldsymbol{M}$ within the film plane. **c** H_{magel} for rotation of $\boldsymbol{M}$ in the $\boldsymbol{xz}$ plane.

$\boldsymbol{\varepsilon} \parallel \boldsymbol{x}$ and plot $H_{\mathrm{magel}} = \sqrt{H_{\mathrm{magel},1}^2 + H_{\mathrm{magel},2}^2}$ as a function of ϕ_0 and θ_0 in Fig. 1.4a. One observes that H_{magel} reaches a maximum (black) whenever $\boldsymbol{M}$ is oriented at 45° to the $\boldsymbol{x}$ axis which is located at the intersection of the blue and the red line in Fig. 1.4a. The driving field furthermore vanishes (white) for $\boldsymbol{M}$ being oriented either parallel or perpendicular to $\boldsymbol{\varepsilon}$. We now turn to the anisotropy of H_{magel} for an in-plane (red line) and out-of-plane (blue line) rotation of $\boldsymbol{M}$, assuming a ferromagnetic thin film in the $\boldsymbol{xy}$-plane. H_{magel} is shown for a rotation of $\boldsymbol{M}$ within the film plane in Fig. 1.4b and for rotation of $\boldsymbol{M}$ in the $\boldsymbol{xz}$ plane in Fig. 1.4c, respectively. In both cases, a four-fold symmetry of H_{magel} is observed with respect to $\boldsymbol{M}$ orientation. Note that for rotation of $\boldsymbol{M}$ in the $\boldsymbol{yz}$ plane, $H_{\mathrm{magel}} = \text{const.} = 0$ as shown by the green line in Fig. 1.4a.

Taken together, Fig. 1.4 shows that no acoustically driven FMR can be observed for equilibrium orientations of $\boldsymbol{M}$ that are either parallel or perpendicular to the pure strain. This unique dependence of the virtual rf driving field on the $\boldsymbol{M}$ orientation is the characteristic fingerprint of acoustically driven FMR. Accordingly, a detailed experimental investigation of this phenomenon will be the focus of this chapter. As a first step to investigate phonon-driven FMR, one needs an appropriate source of phonons at microwave frequencies. In the next section, we discuss the use of surface acoustic waves as such a coherent radio frequency phonon source.

1.2 Surface acoustic waves

Already in 1885, Lord Rayleigh described an elastic wave that does not propagate within the bulk of a solid, but on its surface [43]. These sound waves are therefore called surface acoustic waves (SAWs). SAWs are particularly appealing for phonon-driven FMR, as they provide coherent phonons at the interface of a substrate carrying the SAW and a thin ferromagnetic film deposited on top. Furthermore, the generation and detection of SAWs with frequencies ν the MHz to GHz regime is well established, since SAW devices are commonly used for signal-processing applications [44]. In this section, we will focus on one particular type of SAW, which is called the Rayleigh wave.

We will now investigate the properties of Rayleigh SAWs in piezoelectric solids and refer to them simply as SAWs in the following. The sound velocity c_s of a SAW is in the order of 3000 m/s and with $\lambda = c_\mathrm{s}/\nu$ it follows that the wavelength of a SAW at 1 GHz is approximately 3 µm, which is a convenient length scale for UV photolithography. Any elastic wave with wave-vector $\boldsymbol{k}$ can be compressional, i.e. show a displacement $\boldsymbol{u}$ of lattice atoms which is parallel to $\boldsymbol{k}$, or it can be of the shear type where $\boldsymbol{k}$ and $\boldsymbol{u}$ are orthogonal - or any combination of both. SAWs are of the latter type.

While deriving an expression for the displacement of lattice atoms within the bulk of a piezoelectric exposed to a SAW requires a rather lengthy calculation [44], the displacements directly at the surface follow straightforward criteria [45]. As we will use the SAW to exert stress onto a thin film deposited on top of the piezoelectric crystal carrying the sound wave, we will restrain the discussion of the SAW to the displacements and strains directly at the ferroelectric/ferromagnetic interface.

We consider a SAW with wavelength λ and wavevector $\boldsymbol{k}_\mathrm{SAW}$ which propagates along the $\boldsymbol{x}$-axis of a cartesian coordinate system in an isotropic solid. At the crystal surface, the lattice shows displacements $u_x \propto \sin(2\pi x/\lambda)$ and $u_z \propto \cos(2\pi x/\lambda)$ [45] as illustrated in Fig. 1.5a for a snapshot in time. One notable property of the SAW is the 90° phase shift of the transversal (u_z) and longitudinal (u_x) displacements. In Fig. 1.5a, we denote the pure strain caused by the longitudinal displacement u_x as ε and identify regions with $\varepsilon > 0$ (dark shading) and $\varepsilon < 0$ (light shading) by a color code. Taken together, the lattice displacements u_x and u_z periodic in space and time result in a surface acoustic wave as schematically depicted in Fig. 1.5b.

For applications of SAWs, they need to be generated and detected. This can be achieved all-electrically in piezoelectric materials. Piezoelectric media have crystal

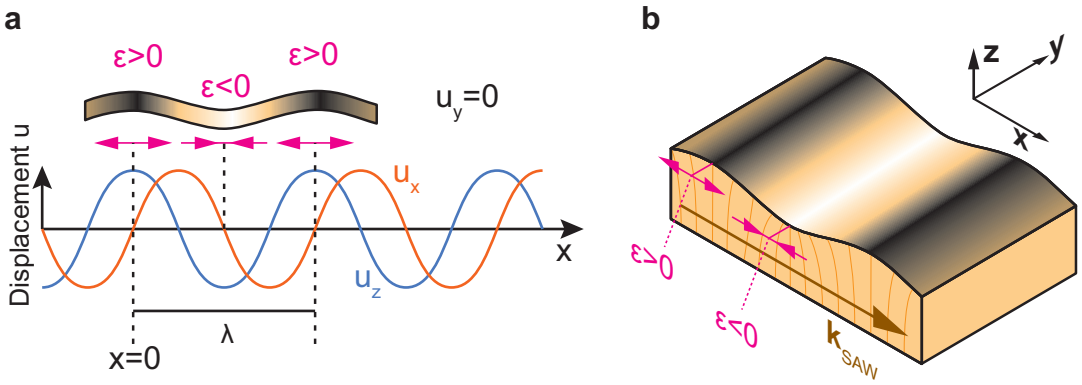

Figure 1.5: A SAW generates (at a snapshot in time) regions with compressive ($\varepsilon < 0$) and dilative ($\varepsilon > 0$) strain at the solid surface. **a** Surface lattice displacement u as a function of x reveals that the SAW has a transversal component u_z and a longitudinal component u_x. **b** Schematic illustration of a SAW propagating on a solid.

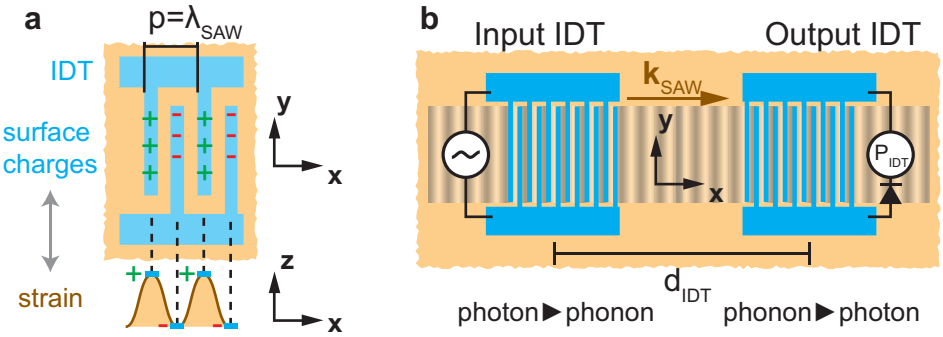

Figure 1.6: **a** SAWs can be generated and detected electrically on piezoelectric substrates by IDTs. The electrodes of an IDT are alternatingly charged, resulting in periodic polarization and thus deformation of the piezoelectric substrate. The SAW wavelength λ_{SAW} is identical to the IDT finger periodicity p. **b** Interdigital transducers (IDTs) are used for an interconversion of photons and phonons via piezoelectricity.

structures lacking inversion symmetry, and the displacement of lattice atoms is linked to internal electric fields. This opens the path for the interconversion of strain ε and electric fields $\boldsymbol{E}$. Formally, this interconversion is governed by the following tensor relations [46]:

$$\sigma_{ij} = \sum_{k,l} c_{ijkl}\varepsilon_{kl} - \sum_{k} e^{\mathrm{T}}_{ijk}E_k \tag{1.11}$$

$$D_i = \varepsilon_0 \sum_{j} d_{ij}E_j + \sum_{j,k} e_{ijk}\varepsilon_{jk} \ , \tag{1.12}$$

where σ_{ij} is the stress tensor, c_{ijkl} the stiffness tensor, D_i the electric displacement, d_{ij} the dielectric tensor and e_{ijk} the piezoelectric tensor. Due to the interconversion of strain and electric field, the application of a periodically varying electric field to the surface of a piezoelectric material will periodically distort its lattice. As schematically depicted in Fig. 1.6a, the periodic potential can be applied by thin conductive strips deposited on the surface of the piezoelectric material. The resulting conductive structure is called interdigital transducer (IDT) and its periodicity p is equal to the periodicity of the surface displacement that is caused by applying a potential difference to the two interdigitated electrode arrays forming the IDT. To launch a SAW, one no longer applies a static, but an alternating voltage to the IDT at its fundamental frequency $\nu_0 = c_\mathrm{s}/p$ as shown for the input IDT in Fig. 1.6b. As the SAW carries an electric potential along with its elastic deformation in a piezoelectric material, it can be detected by an IDT as well. Thus, either IDT shown in Fig. 1.6b can be used to excite or detect the SAW. In total, the input IDT is used for the conversion of microwave photons to microwave phonons at a frequency determined by IDT geometry and SAW velocity. The output IDT is used for the reverse process and enables an electrical detection of the acoustic wave. We now briefly discuss the expected frequency response of the structure shown in Fig. 1.6b which is commonly referred to as a SAW delay line due to the relatively slow sound velocity.

We consider the IDT shown in Fig. 1.6a but assume each finger to be only a line charge along $\boldsymbol{y}$ for simplicity. In this so called delta-function model of the IDT [44], the surface potential is a succession of delta functions with alternating polarity as shown in Fig. 1.7a. For illustrative purposes, only $N_\mathrm{e} = 5$ IDT electrodes are shown and we assume $x = 0$ to be the position of the central electrode of the IDT. We now regard the time domain evolution of the electric amplitude of a SAW that is launched

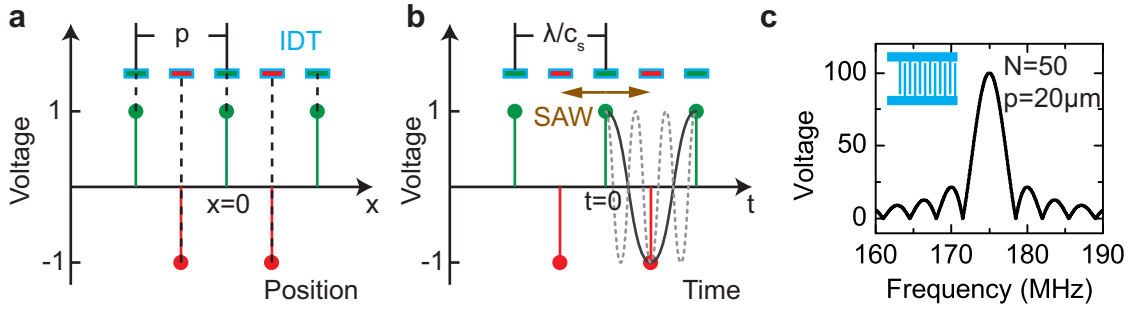

Figure 1.7: **a** In the delta function model, each IDT finger is assumed to be a line charge. **b** In the time domain, a SAW wavefront is launched at $x = t = 0$. Negative times denote the SAW traveling to the left and positive times the SAW traveling to the right. If the SAW wavelength λ is an odd multiple of p, its electric potential is amplified at each IDT finger. **c** Calculated transmission of a single IDT as a function of frequency for $p = 20\,\mu\text{m}$ and $N = 50$ finger pairs.

at the central finger at $x = 0$ at a time $t = 0$. Note that due to piezoelectricity, the electric potential carried by the SAW is linked to the lattice displacement it causes. As shown in Fig. 1.7b, if the wavelength λ of the SAW is equal to the IDT periodicity p, the SAW's electric surface potential will be amplified each time the wavefront passes an IDT finger. Note that the same holds true for p being an odd multiple of λ as shown by the dashed wave in Fig. 1.7b. Hence, IDTs can be operated at odd harmonic frequencies of their fundamental frequency ν_0.

We now discuss the frequency response of the IDT around ν_0 - the same considerations apply for all odd harmonics. A transition from the time to the frequency domain is required to derive the frequency response of the time-dependent impulse response shown in Fig. 1.7b. This transition can be achieved via Fourier transform. To calculate the frequency response of a discrete series of amplitudes A_n we apply the discrete-time Fourier transformation defined as

$$X(\nu) = \sum_n A_n e^{-in2\pi\nu T}\,, \tag{1.13}$$

with the sampling time T and coefficients A_n. We can now calculate the frequency response of the IDT by using $T = \frac{p}{2c_\text{s}}$ as the sampling time of a SAW traveling along the discrete IDT electrodes shown in Fig. 1.7b. The sampling time thus corresponds to the finger spacing in the time domain picture in Fig. 1.7b. For N_e IDT electrodes

this yields

$$X_{\mathrm{IDT}}(\nu) = \sum_{n=0}^{N_\mathrm{e}-1} A_n e^{-in\pi\nu p/c_\mathrm{s}} \,. \tag{1.14}$$

The factor A_n thereby describes the excitation amplitude at the n^{th} IDT electrode. In the simple case considered here, $A_n = (-1)^n$ to account for the alternating unity potential shown in Fig. 1.7b. Evaluation of $X_{\mathrm{IDT}}(\nu)$ yields the complex frequency response of a single typical IDT. From this response, one can extract the magnitude $|X_{\mathrm{IDT}}(\nu)|$ and the phase $\arg\left(X_{\mathrm{IDT}}(\nu)\right)$. $|X_{\mathrm{IDT}}(\nu)|$ is plotted in Fig. 1.7c for an IDT featuring $p = 20\,\mu\mathrm{m}$, $c_\mathrm{s} = 3500\,\mathrm{m/s}$ and $N = N_\mathrm{e}/2 = 50$ finger pairs. A center frequency $\nu_0 = 175\,\mathrm{MHz}$ is obtained as expected from the relation $\nu = c_\mathrm{s}/p$.

The evolution of $|X_{\mathrm{IDT}}(\nu)|$ closely mimics a sinc function response given by [44]

$$|X_{\mathrm{IDT}}(\nu)| \approx N_\mathrm{e} \left| \frac{\sin\left(N\pi(\nu-\nu_0)/\nu_0\right)}{N\pi(\nu-\nu_0)/\nu_0} \right| \,. \tag{1.15}$$

This can be understood as the sinc function is just the fourier transformation of the rectangular function representing the impulse response of the IDT which is discretized by the delta functions shown in Fig. 1.7a. In general, the frequency response of an IDT is hence given by the fourier transform of its impulse response which again is determined by IDT geometry. The design of elaborate IDTs that achieve almost arbitrary frequency responses is a key element in modern telecommunication applications where SAW filters are widely applied [44, 45, 47]. These filters are used, e.g., as bandpass filters in mobile phones for their performance, low cost, ease of miniaturization and integration into electronic circuitry. For this work, we will use the simple IDT design already introduced. Note, however, that varying A_n by means of non-uniform IDT finger overlap (achieved by adjusting the IDT finger length on a per-electrode basis) opens the path for more advanced IDT designs. The most commonly found example of this so-called apodization process is shaping the finger overlap according to a sinc-function. This results in a rectangular frequency response which is particularly desirable for bandpass filters.

So far we have discussed only a single IDT launching a SAW. However, for signal processing applications, one generally wants to electrically read out the amplitude of the generated SAW by a second IDT. Due to the reciprocity of the piezoelectric effect, identical considerations apply for this conversion. Hence, for an acoustic delay line featuring two IDTs, IDT1 and IDT2, the magnitude of the total frequency transmis-

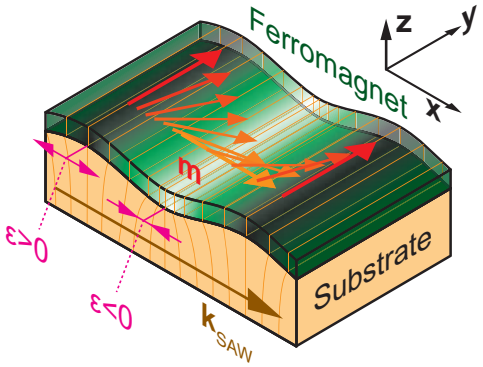

Figure 1.8: The local strain ε due to the SAW influences the local $\boldsymbol{M}$ orientation in a ferromagnetic thin film via magnetoelastic coupling.

sion is given by $|H(\nu)| = |X_{\mathrm{IDT1}}(\nu)| \cdot |X_{\mathrm{IDT2}}(\nu)|$. As we investigate SAW delay lines consisting of two identical IDTs, we thus expect the transmission magnitude to mimic a sinc^2 function.

Taken together, SAWs can be excited and detected using conductive IDTs on a piezoelectric substrate. The IDT geometry thereby determines the wavelength and thus the operation frequency of the SAW device. The fundamental frequency ν_0 is given by $\nu_0 = c_\mathrm{s}/\lambda$ and operation at odd multiples of ν_0 is possible.

We now consider a ferromagnetic thin film deposited on top of the piezoelectric crystal carrying the SAW. As the SAW typically decays within one wavelength $\lambda \geq 1\,\mu\mathrm{m}$ into the bulk of the crystal, we can consider the thin film with thickness smaller than 100 nm to be infinitely thin such that only the surface lattice displacements u_x and u_z already discussed need to be considered. Such a piezoelectric/ferromagnetic hybrid is depicted schematically in Fig. 1.8 for a snapshot in time. For simplicity, we consider only the pure strain ε along $\boldsymbol{x}$ which is again indicated by the color code. Due to magnetoelasticity, locally different strains ε will induce locally different effective fields $\boldsymbol{H}_{\mathrm{magel}}$ into the ferromagnet, resulting in different local equilibrium orientations $\boldsymbol{m}$ of the magnetization. Hence, the SAW allows to manipulate the magnetization at radio frequency (rf). To achieve such a rf magnetoelastic coupling, we fabricated acoustic delay lines on piezoelectric $LiNbO_3$ substrates and deposited ferromagnetic Ni thin films within the SAW propagation path. The actual sample fabrication is discussed in the next section.

1.3 Sample fabrication and experimental setup

Two basic elements need to be considered to investigate the interaction of phonons and magnons in a piezoelectric/ferromagnetic hybrid. First, appropriately designed IDTs have to be fabricated, and second, a ferromagnetic thin film has to be deposited within the SAW propagation path. Both steps are carried out via a lithography process followed by electron beam metal deposition and lift-off. Using optical lithography, a minimal feature size of 3 µm is thereby achieved. The IDT design and fabrication was carried out in close collaboration with two Bachelor students, Hajo Söde and Frederik Goerg. Details of the fabrication process can be found in their Bachelor theses [48,49]. Here, only a brief summary of the used materials and designs is given. While a large number of samples were actually fabricated and characterized with respect to phonon-magnon interaction, in this chapter we will restrain the discussion to the sample that was investigated in greatest detail.

We chose lithium niobate ($LiNbO_3$) as substrate material for all SAW samples discussed in this thesis. $LiNbO_3$ has a tetragonal unit cell with the long axis commonly denoted Z and the short axes denoted X and Y. The $LiNbO_3$ crystals employed in this work were obtained from a 0.5 mm thick Y-cut wafer, meaning that the Y axis points out of plane. The wafer was cut into $5 \times 6\,\mathrm{mm}^2$ rectangular substrates with their short side parallel to Z, which is the main axis for SAW propagation. $LiNbO_3$ is commonly used in SAW-based devices due to its high electromechanical coupling efficiency k^2 which is defined as

$$k^2 = \frac{e^2}{c\varepsilon_0\varepsilon_\mathrm{r}}\,, \tag{1.16}$$

with the piezoelectric coefficient e ($\mathrm{C/m^2}$), the elastic constant c ($\mathrm{N/m^2}$) and the vacuum and relative permittivities ε_0 and ε_r. $k^2 \approx 5\%$ [45] for $LiNbO_3$ is a measure for the efficiency of the conversion of electrical energy to mechanical energy or vice versa. As we want to exploit the elastic displacement of a SAW excited and detected by electric potentials, using a material with high k^2 is beneficial.

To launch and detect the SAW, an acoustic delay line consisting of two identical IDTs is fabricated and aligned along the $LiNbO_3$ Z axis. The final IDTs feature a periodicity $p = 20\,\mu\mathrm{m}$ and further dimensions as shown in Fig. 1.9. The IDT design shown here was optimized for high fundamental frequency transmission of a delay line consisting of two identical IDTs, while allowing it to be operated at higher harmonic frequencies as well. It was found that a larger number N of finger pairs increased the

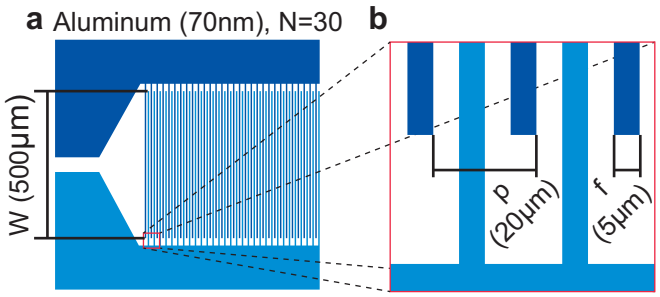

Figure 1.9: **a** Actual IDT design, featuring $N = 30$ finger pairs with a finger overlap of $W = 500\,\mu\text{m}$ made of 70 nm thick aluminum. **b** Closeup of IDT design, showing a finger width of $f = 5\,\mu\text{m}$ and a periodicity $p = 20\,\mu\text{m}$.

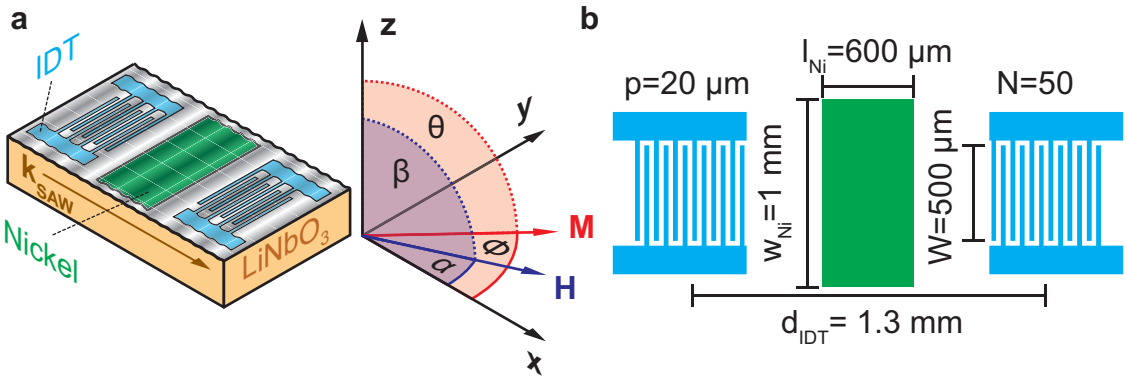

Figure 1.10: **a** Schematic illustration of finished hybrid device. **b** Design parameters chosen for the actual samples (not to scale).

transmission at the respective passband center frequencies [48]. $30 \leq N \leq 50$ thereby provides a good tradeoff between transmission characteristics, IDT size, and yield of the fabrication process.

For all results discussed in this thesis, IDTs with a periodicity of $p = 20\,\mu\text{m}$ are employed, resulting in a fundamental frequency of $\nu_0 = 172\,\text{MHz}$. For the IDT fabrication, optical lithography masks were designed and used in a contact lithography process [49]. To achieve the desired structure sizes, the photoresist AZ5214E was employed in an image reversal process. Subsequent to the lithography process, 70 nm of aluminum (Al) were deposited on the samples by electron beam evaporation. The IDT structure was finally revealed in a lift off process in warm acetone and with the aid of ultra sound.

To probe the interaction of the SAW with magnetoelastic media, a ferromagnetic thin film is deposited within the SAW propagation path after a second lithography

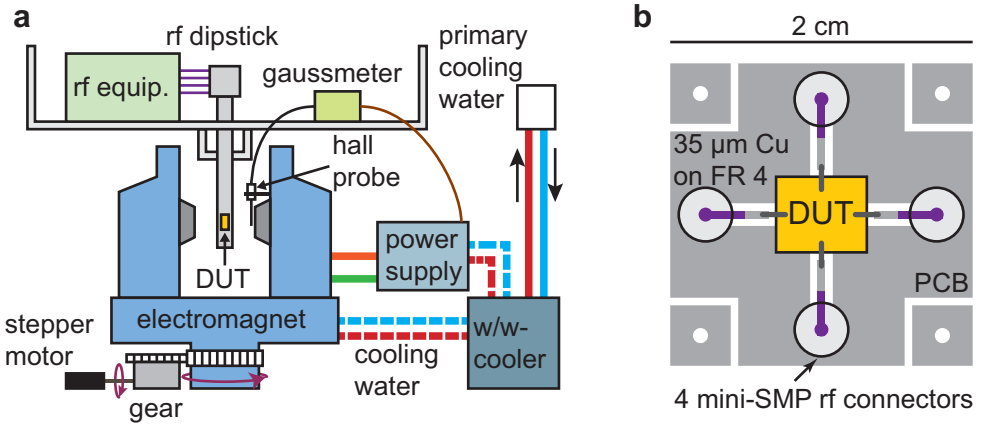

Figure 1.11: **a** Schematic view of the setup assembled and used for all experiments with surface acoustic waves. **b** Closeup of the DUT, showing the actual PCB design used. Up to 4 rf leads can be connected to the PCB and wire bonding is used to establish the electrical connection to the DUT.

step. In this chapter, we investigate a nickel (Ni) thin film of rectangular shape with lateral dimensions $0.6 \times 1\,\mathrm{mm}^2$ and a thickness of 50 nm. The ferromagnetic thin film was prepared in a process analogous to that described above for the Al IDTs. A schematic view of the finished hybrid device is shown in Fig. 1.10a. The illustration in Fig. 1.10b shows the actual dimensions of the structure investigated in this chapter. To control the phonon-magnon interaction, it is necessary to control the Ni magnetization $\boldsymbol{M}$. This is achieved via the application of an external, static magnetic field $\boldsymbol{H}$.

This external magnetic field is provided by a rotatable electromagnet capable of delivering magnetic fields up to 1.5 T at a pole shoe separation of about 7 cm. The setup depicted in Fig. 1.11a was conceived and built during this thesis around an already existing Oerlikon electromagnet. The magnet is energized via a Lakeshore 642 bipolar power supply delivering currents up to 70 A. The power supply output is controlled via a Lakeshore 475 DSP Gaussmeter in closed loop PI mode to match a magnetic field setpoint measured by a Hall probe between the pole shoes. Magnet and power supply are water cooled via a 10 kW water-water heat exchanger which decouples the setup from the primary in-house cooling water to minimize the risk of water damage to the setup and to compensate for cooling water temperature and flow instabilities. Water flow controllers were installed to ensure appropriate cooling of the setup and to automatically de-energize the magnet in the event of a cooling water

failure. A radio frequency (rf) dipstick with four rf leads was specifically designed and built for this setup and is employed to mount the device under test (DUT) between the pole shoes of the magnet. The orientation of the external magnetic field with respect to the DUT is set via rotation of the electromagnet. This approach was chosen (rather than rotating the dipstick) to avoid any movement of sample and rf wiring during measurement which would influence the rf transmission. The electromagnet is rotated by a stepper motor (Nanotec ST11018) through a 82:1 gear. Magnet rotation is possible within an arc of 220° and limit switches at both end positions are employed to automatically stop magnet rotation upon triggering. This ensures fail-safe operation of the magnet rotation that avoids damage to the gear, cooling water tubes and electric wiring. All equipment is connected to a control computer which is used to set magnetic field magnitude and orientation and to read out measurement devices. For the control of the measurement setup, a Labview program was developed which enables fully automated measurement data acquisition as a function of external magnetic field magnitude, orientation and various rf properties. The DUT is mounted in the dipstick on a printed circuit board (PCB) sample holder. The actual PCB design is shown in Fig. 1.11b and features four mini-SMP rf connectors that are soldered to the PCB. On-chip wire bonding establishes electrical connection from the PCB to the DUT. For the results discussed in this chapter, rf leads were plugged into the two mini-SMP connectors that are connected to the input and output IDT.

A vector network analyzer (VNA) is used to record the transmission S_{21} of the acoustic delay line as a function of frequency. While a more complete description of vector network analysis can be found in Ref. [50], for the understanding of the results presented in this chapter it is sufficient to know that S_{21} is the ratio of the rf voltage detected at port 2 of the VNA to the rf voltage output at port 1. As this detection is phase sensitive, S_{21} is a complex number. It is defined as [50]

$$S_{21} = \frac{Ae^{i\varphi_1}}{Be^{i\varphi_2}} =: \frac{a}{b} \,, \tag{1.17}$$

with the electromagnetic waves a and b corresponding to the detected and the emitted waves, respectively. It follows that for passive devices $|S_{21}| \leq 1$. Often $|S_{21}|$ is plotted on a logarithmic scale as

$$|S_{21}|\,(\mathrm{dB}) = 20 \log |S_{21}| \ . \tag{1.18}$$

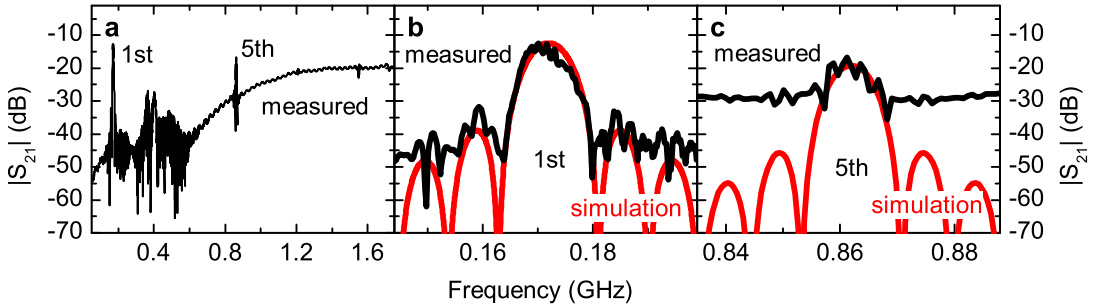

Figure 1.12: **a** Transmission $|S_{21}|$ as a function of frequency. The most pronounced transmission maxima are observed at approximately 170 MHz and 860 MHz and correspond to the launching of a SAW. **b** The experimentally determined transmission at the fundamental frequency (black) shows some deviations from the simulated curve (red). **c** At the 5^{th} harmonic, the deviations are more pronounced.

In this commonly used definition, $|S_{21}|$ (dB) corresponds to a power ratio rather than the voltage ratio measured by $|S_{21}|$. We will now investigate S_{21} of our "magnetoacoustic" delay line as a function of frequency and external magnetic field magnitude and orientation.

1.4 Experimental results

To investigate the phonon-magnon interaction in SAW-based hybrid devices, one needs to consider several key aspects. As a basic prerequisite to the experiments discussed here, evidence for the actual launching and detection of a SAW needs to be quantitatively established via a transmission measurement. Corresponding measurement data is then purged from any contributions not due to the SAW to exclude possible spurious effects due to the presence of, i.e., electromagnetic free space waves. Finally, a detailed study of the magnetic field dependence of the SAW-transmission provides experimental evidence for phonon-driven FMR, in particular featuring the 4-fold symmetry predicted in Fig. 1.4.

1.4.1 Delay line transmission

The two IDTs forming the magnetoacoustic delay line schematically shown in Fig. 1.10 are connected to the two ports of a Rohde & Schwarz ZVA 24 vector network analyzer.

The transmission S_{21} is measured in a frequency range from 10 MHz to 1.7 GHz at room temperature and in the absence of externally applied magnetic fields. $|S_{21}|$ (dB) is shown in Fig. 1.12a as a function of frequency. The transmission maxima at $\nu_0 = 172\,\text{MHz}$ and $\nu_5 = 861\,\text{MHz}$ are attributed to the launching and detection of a SAW at these frequencies. Comparison with IDT geometry ($p = \lambda = 20\,\mu\text{m}$) allows to conclude that the transmission maxima represent the fundamental IDT frequency and its 5^{th} harmonic with a SAW velocity of $c_\text{s} = \lambda\nu_0 = 3440\,\text{m/s}$ in very good accordance to literature values [45]. The several transmission peaks evident around 400 MHz are attributed to the generation of bulk acoustic waves [51] and conceal the third harmonic SAW excitation. We now investigate the two SAW passbands identified in Fig. 1.12a in more detail. The black lines in Figs. 1.12b and c show a closeup of the measured $|S_{21}|$ in the region around the 1^{st} and 5^{th} harmonic, respectively. For comparison, a sinc^2 function is shown in these panels to describe the expected SAW bandpass filter shape as discussed in Section 1.2 (red lines). While data in Fig. 1.12b shows quite good agreement to the simulation, large deviations are present in the data presented in Fig. 1.12c. Most strikingly, as already visible in Fig. 1.12a, the baseline of the transmission increases with increasing frequency. Furthermore, oscillations in $|S_{21}|$ are observed within and outside the main passband lobe. We attribute these non-idealities to the launching and detection of electromagnetic free-space waves that travel at the speed of light. These spurious contributions to $|S_{21}|$ can be investigated and separated from elastic waves traveling at the speed of sound in a time domain analysis, as discussed in the following.

1.4.2 Time domain analysis

Transition to the time domain is achieved via an inverse Fourier transformation of the frequency domain data presented in Fig. 1.12. Details of the Fourier transformation process can be found in the Diploma thesis of Christian Heeg [52] whom I advised. The calculated time domain response S_{21} for the fundamental and fifth harmonic SAW excitation is found in Fig. 1.13a and b, respectively. In each of these time domain traces, three distinguished oscillating impulses are observed as a function of time. As shown in Fig. 1.13c, each of these pulses can be attributed to a unique process in the delay line. Upon applying a rf voltage to the input IDT, an electromagnetic wave (EMW) is launched as the IDT fingers serve as an rf antenna. The EMW traverses the delay line at the speed of light and is detected by the antenna formed by the

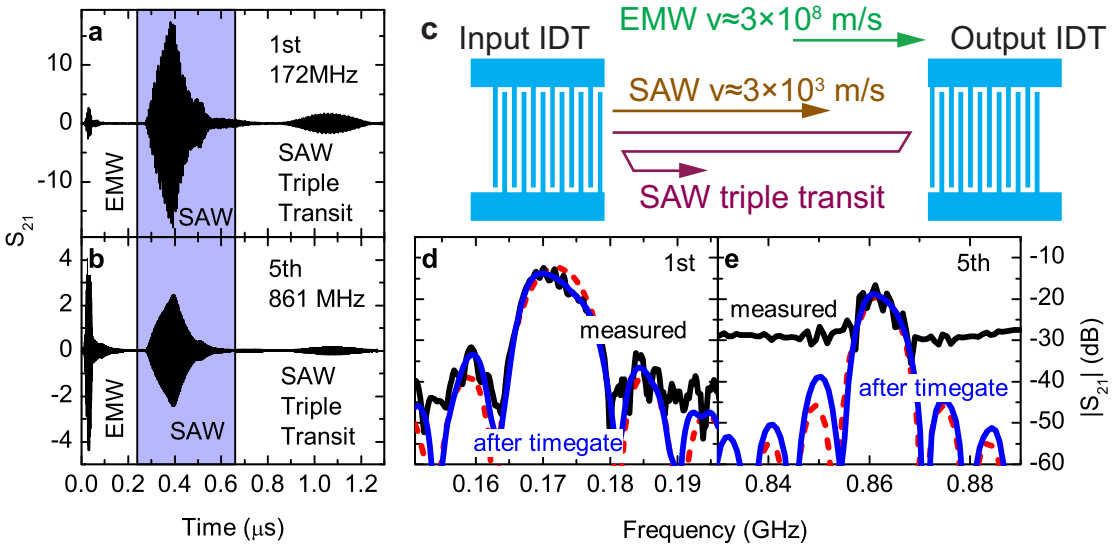

Figure 1.13: **a-b** Transmission data as a function of time, obtained via inverse fourier transformation of the data shown in Fig. 1.12b-c, respectively. **c** Contributions due to electromagnetic waves (EMW), SAW and triple transit SAWs can be separated in the time domain. **d-e** Fourier transformation of gated time domain data (see text) yields the contribution of only the SAW to $|S_{21}|$ (blue line) showing good agreement to the simulation (dashed red line).

output IDT. The EMW gives rise to the first pulse observed in the time domain traces. The fact that it does not appear instantaneously[1] but with a delay of about 20 ns is attributed to the finite length of the rf leads of several meters. With an IDT separation of $d_{\mathrm{IDT}} = 1.3\,\mathrm{mm}$ (cf. Fig. 1.10b), the SAW is expected to have a transit time of $t_{\mathrm{SAW}} = d_{\mathrm{IDT}}/c_{\mathrm{s}} \approx 0.37\,\mu\mathrm{s}$ which perfectly matches the middle impulse found in the time domain data. The last impulse found in Figs. 1.13a and b is finally attributed to the triple transit SAW, that is the wave that is reflected twice at the IDTs before being detected at the output IDT as shown in Fig. 1.13c. The triple transit SAW is expected to be found at $3t_{\mathrm{SAW}} \approx 1.1\,\mu\mathrm{s}$, which is just the time at which the third impulse is observed. In total, the time domain data thus shows that there are three main contributions to the frequency domain signal: The EMW, the SAW and the triple transit SAW.

From Figs. 1.13a it can be seen that at the fundamental frequency, the SAW is the dominant contribution to the total signal. However, as depicted in Fig. 1.13b, the EMW and SAW contributions are of comparable magnitude for the fifth harmonic

[1] for $d_{\mathrm{IDT}} = 1.3\,\mathrm{mm}$ and $c = 3 \times 10^8\,\mathrm{m/s}$, $t \approx 4\,\mathrm{ps}$

excitation. This can be understood as the efficiency of the SAW fifth harmonic generation is about 40% of the fundamental frequency efficiency for the IDT metallization ratio of 0.5 used for our IDTs [44]. The same holds true for the SAW detection, resulting in an expected 16% (or $-8\,\mathrm{dB}$) transmission of the 5^{th} harmonic with respect to the fundamental frequency. This is in very good accordance to the 15% transmission ($S_{21}^{1\mathrm{st}} = 16$ for the fundamental vs. $S_{21}^{5\mathrm{th}} = 2.4$ for the 5^{th}) found for the SAW pulse in the time domain traces in Figs. 1.13a and b.

As detailed in Refs. [50,52], we now multiply the data displayed in Figs. 1.13a and b by a timegate and subsequently perform a Fourier transform back to the frequency domain. For illustrative purposes, the timegate can be considered as a simple sequence of 1s for the times where the SAW pulse is found (blue shading in Figs. 1.13a and b) and 0s elsewhere. The timegate thus effectively nullifies the impulses due to the EMW and triple transit SAW, leaving only the SAW pulse in the time domain. In Figs. 1.13d and e, the fourier transforms of the gated time domain data are shown by the blue solid curves together with the original measurement data (black solid curves). Strikingly, the timegated data now almost perfectly mimic a sinc^2 function (dashed red curves) for both frequencies. Note that, in particular, the timegate nullifies the interference of SAW and EMW at the output IDT, resulting in elimination of the passband ripple. The timegated traces in Figs. 1.13d and e thus represent the transmission of an ideal SAW delay line without any spurious effects. This means that by timegating the measured data we now have separated the *photons* from the *phonons* by exploiting their vastly different propagation velocities. This is a fundamental step towards the investigation of purely *phonon*-driven magnetization dynamics that will be discussed in the following.

1.4.3 Phonon driven ferromagnetic resonance

Having dealt with the removal of electromagnetic crosstalk and triple transit interference, we revisit the transmission data of the delay line. Figure 1.14a shows $|S_{21}|\,(\nu)$ as measured (black) and after the application of the timegate (blue). In the gated data, the marked SAW transmission maxima are clearly visible. In particular, while the 9^{th} harmonic transmission was dominated by electromagnetic crosstalk in the raw data, the timegated data shows a clear sinc^2 passband as evident from the frequency evolution of $|S_{21}|$ shown in Fig. 1.14b. We will now investigate the dependence of the timegated $|S_{21}|$ data on an externally applied magnetic field $\boldsymbol{H}$. To this end,

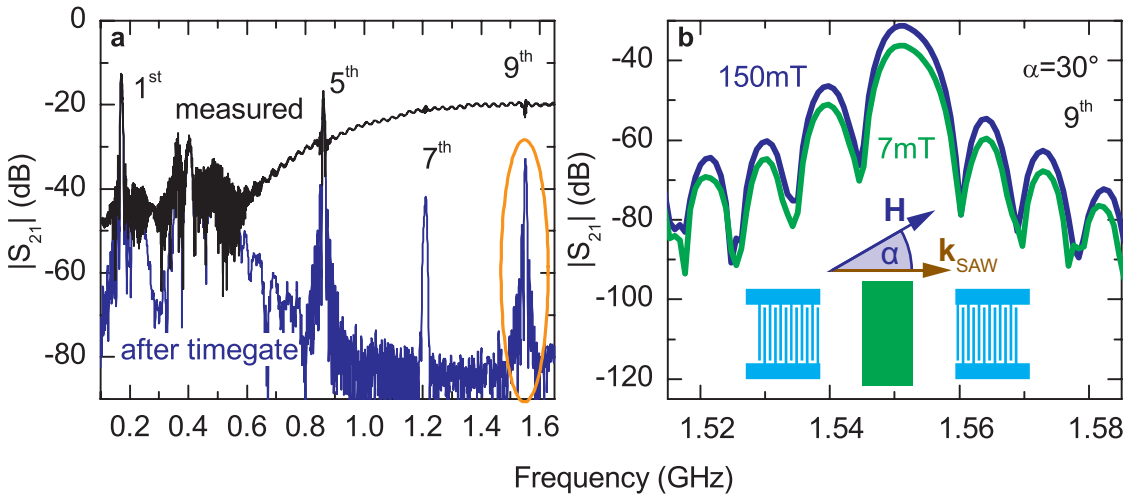

Figure 1.14: **a** $|S_{21}|$ as a function of frequency as measured (black) and after application of the timegate (blue). In the gated data, transmission maxima at odd harmonics of the fundamental frequency can be clearly identified. **b** Closeup of $|S_{21}|$ around the 9$^{\text{th}}$ harmonic for two different magnitudes of the external magnetic field $\boldsymbol{H}$ applied at $\alpha = 30°$ ($\beta = 90°$). At $\mu_0 H = 7\,\text{mT}$ (green), the SAW is attenuated.

$\boldsymbol{H}$ is applied within the film plane ($\beta = 90°$) at an angle $\alpha = 30°$ to the SAW propagation direction. Figure 1.14b depicts the evolution of $|S_{21}|$ as a function of frequency around the 9$^{\text{th}}$ harmonic for two different magnitudes of $\boldsymbol{H}$. We observe that at $\mu_0 H = 150\,\text{mT}$ (blue) the transmission $|S_{21}|$ is higher than at $\mu_0 H = 7\,\text{mT}$ (green). As we deal with timegated data here, the magnetic field dependence can not be caused by the electromagnetic free space wave and is thus attributed to a magnetic field-dependent change of the SAW amplitude. This will now be investigated in more detail. We consider the relative change in $|S_{21}|\,(\nu)$ determined at a magnetic field magnitude H with respect to a reference magnetic field magnitude H_{ref}. Both, reference and measurement field, are applied at identical orientation α. We define

$$\Delta\,|S_{21}|\,(\nu, H)(\text{dB}) = |S_{21}|\,(\nu, H)(\text{dB}) - |S_{21}|\,(\nu, H_{\text{ref}})(\text{dB})\;, \tag{1.19}$$

which depicts a relative change on a logarithmic scale as it is the difference of two logarithms (cf. Eq. (1.18)). For data shown here, we take $\mu_0 H_{\text{ref}} = 150\,\text{mT}$. We now consider the data obtained at $\mu_0 H = 7\,\text{mT}$.

Figure 1.15a shows a closeup of $|S_{21}|$ within the central part of the 9$^{\text{th}}$ harmonic

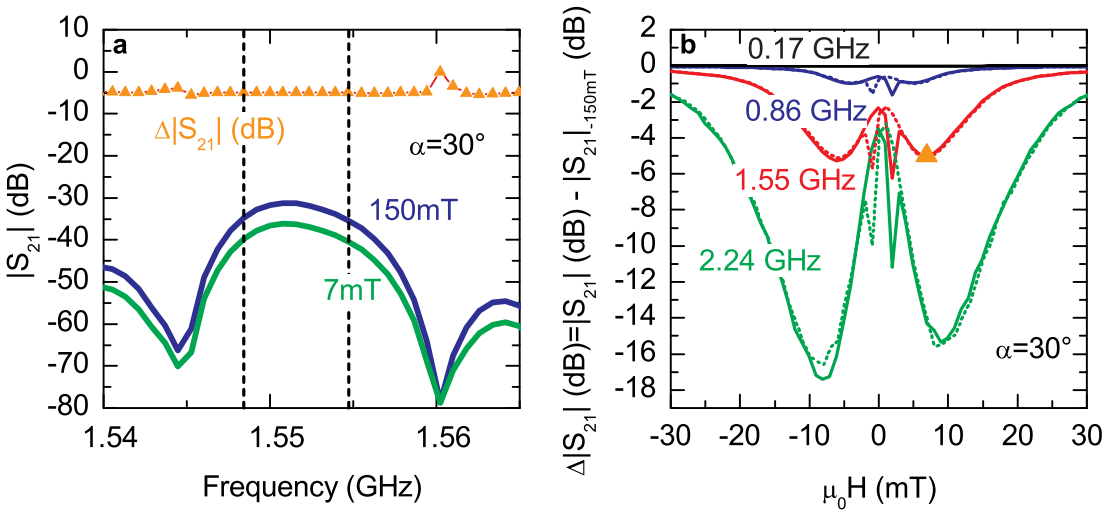

Figure 1.15: **a** The relative change of $|S_{21}|$ (orange) remains virtually constant within the FWHM (dashed lines) of the $^{\text{th}}$ harmonic SAW passband. **b** Relative change in $|S_{21}|$ as a function of H for all passbands investigated. The orange triangle corresponds to the averaged $|S_{21}|$ within the passband shown in panel **a**. The field-symmetric, non-hysteretic attenuation maxima are attributed to acoustically driven FMR.

passband lobe for $\mu_0 H_{\text{ref}} = 150\,\text{mT}$ (blue) and $\mu_0 H = 7\,\text{mT}$ (green). $\Delta\,|S_{21}|$ is thus given by the difference of these two $|S_{21}|$ traces. As shown by the orange data points in Fig. 1.15a, $\Delta\,|S_{21}|$ is constant within the full width at half maximum (FWHM) of the passband indicated by the vertical dashed lines. We will thus only consider the mean value of $\Delta\,|S_{21}|$ within the passband for the following discussion of the field dependent data and, for simplicity of notation, still refer to it as $\Delta\,|S_{21}|$. So far, we have only investigated transmission data obtained at the 9^{th} harmonic at a magnetic field of $\mu_0 H = 7\,\text{mT}$. Now we consider the data obtained during a full magnetic field sweep $-150\,\text{mT} \leq \mu_0 H \leq +150\,\text{mT}$ for the four most pronounced SAW transmission maxima.

Data shown in Fig. 1.15b were recorded at the fundamental frequency (172 MHz, black), the 5^{th} (860 MHz, blue), the 9^{th} (1.55 GHz, red) and the 13^{th} (2.24 GHz, green) harmonic. The solid lines show data obtained during the magnetic field upsweep, while the dashed lines correspond to the magnetic field downsweep. Exemplarily, we discuss the data obtained at the 9^{th} harmonic (1.55 GHz, red). The distinguished data point (orange triangle) corresponds to the $\Delta\,|S_{21}| \approx -5\,\text{dB}$ data shown in Fig. 1.15a (orange) averaged within the passband of the 9^{th} harmonic as indicated by the dashed

lines in Fig. 1.15a. Two main features can be observed in $\Delta|S_{21}|(H)$ shown in Fig. 1.15b. First, close to zero external magnetic field, two hysteretic, sharp dips are visible. These are attributed to the switching of the ferromagnet which in turn alters its elastic properties due to magnetostriction [38]. As the SAW is sensitive to a change in the stiffness of the material it propagates within, this yields the sharp features found in $\Delta|S_{21}|$. This non-resonant interaction of SAW and ferromagnet due to equilibrium magnetostriction has already been reported in literature [33]. Even more intriguing however, two non-hysteretic dips in $\Delta|S_{21}|$ are observed at $\mu_0 H = \pm 7\,\mathrm{mT}$ for $\nu = 1.55\,\mathrm{GHz}$. As the coercive field of the Ni film used is about $\mu_0 H_\mathrm{c} = 2\,\mathrm{mT}$, as clearly evident by the sharp features discussed before, these dips can not be attributed to the formation of magnetic domains. Data recorded within the remaining frequency passbands furthermore shows that these dips in $\Delta|S_{21}|$ are shifted to higher magnetic fields for increasing frequency. This is in accordance to the FMR condition defined in Eq. (1.4). We thus attribute these dips to a resonant interaction of the SAW and the ferromagnetic thin film.

As discussed in the introduction to phonon-driven FMR in Section 1.1, the magnetoelastic driving field is a function of both, the externally applied elastic excitation and the internal magnetization. Thus, phonon-driven FMR can be identified via its characteristic dependence on the magnetization orientation. Experimentally, this magnetization orientation is controlled via the magnitude and orientation of an externally applied magnetic field. It is hence mandatory to carry out a detailed investigation of $\Delta|S_{21}|$ as a function of external magnetic field orientation and magnitude.

To this end, we performed measurements in the same fashion as those discussed in the context of Fig. 1.15 for $-90° \leq \alpha \leq 90°$ with $\beta = \text{const.} = 90°$. The $\Delta|S_{21}|$ data obtained for this in-plane rotation of the external magnetic field are shown in Fig. 1.16a-c for the H upsweep as a function of α and H. Hereby, data recorded at $\alpha = 30°$ corresponds to data shown in Fig. 1.15b at the respective frequencies. While the maximum relative change in absorption increases with increasing frequency, the general evolution of $\Delta|S_{21}|$ is comparable among the three passbands investigated. In each case, the $\boldsymbol{M}$ switching process can be observed at all orientations α at $\mu_0 H_\mathrm{c} \approx 2\,\mathrm{mT}$. More intriguingly, all $\Delta|S_{21}|$ data share a similar angular dependency, in particular $\Delta|S_{21}| = 0$ at both, $\alpha = 90°$ and $\alpha = 0°$. This is in accordance to the simple model discussed in Section 1.1, where the internal magnetoelastic driving field vanishes for these orientations of $\boldsymbol{M}$. The fact that the maximum absorption is not

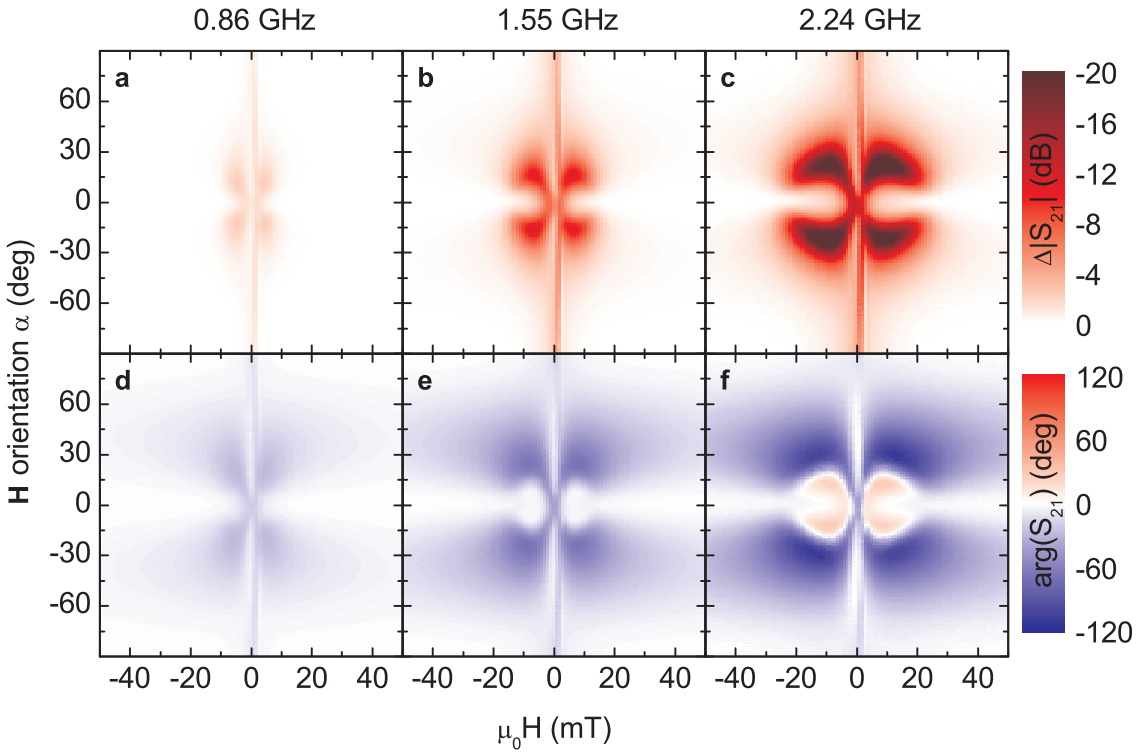

Figure 1.16: **a** to **c** $\Delta\,|S_{21}|$ as a function of in plane $\boldsymbol{H}$ orientation α ($\beta = 90°$) and H for 860 MHz, 1550 MHz and 2240 MHz, respectively. **d** to **f** The corresponding phase $\arg(S_{21})$.

found at $\alpha = 45°$ but rather at $\alpha \approx 20°$ is due to the in-plane magnetic anisotropy of the Ni thin film that results in a finite angle between the $\boldsymbol{M}$ and $\boldsymbol{H}$ orientations ϕ and α. This again demonstrates that acoustic FMR is actually driven by a phonon-magnon tickle field that depends on intrinsic magnetic properties of the ferromagnet.

We have furthermore evaluated the phase $\arg(S_{21})$ of the complex S_{21} parameter obtained via vector network analysis. Figure 1.16d-f shows contour plots of $\arg(S_{21})$ for the three investigated passbands. Here, we arbitrarily set $\arg(S_{21}) = 0$ out of resonance. Again, a four-fold symmetry is observed with the changes in $\arg(S_{21})$ becoming larger with increasing frequency.

1.5 Quantitative analysis and comparison to simulation

In this section, the obtained experimental results are compared to model calculations based on the modified LLG approach described in Section 1.1. Details of the model

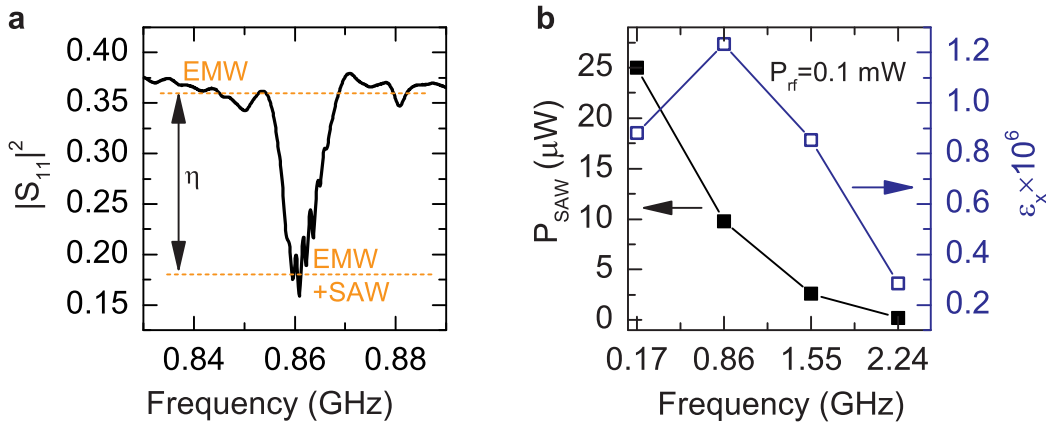

Figure 1.17: **a** Measured $|S_{11}|^2$ around the 5$^{\text{th}}$ harmonic. $\eta = |S_{11}|^2\,(\text{EMW}) - |S_{11}|^2\,(\text{EMW} + \text{SAW})$ is the power conversion efficiency of the IDT. **b** The total SAW power P_{SAW} and the strain ε for the investigated passbands at an rf power $P_{\text{rf}} = 0.1\,\text{mW}$ (the lines are a guide to the eye).

of acoustically driven FMR that was conceived to a large extent by Lukas Dreher can be found in Ref. [53].

1.5.1 Calculation of elastic strain

For a quantitative analysis of the acoustically driven FMR, one needs to determine the strain ε in the ferromagnet, which gives rise to the magnetoelastic driving field defined in Eq. (1.9). To quantify the strain, we performed vector network analysis on the input IDT. Thereby we measure the voltage reflection coefficient S_{11}. This coefficient is the ratio of the output voltage of the vector network analyzer at port 1 to the detected voltage at the same port. Figure 1.17a shows the power reflection ratio $|S_{11}|^2$ at the input IDT as a function of frequency exemplarily around the 5$^{\text{th}}$ harmonic of the IDT. The pronounced dip in $|S_{11}|^2$ at $\nu = 860\,\text{MHz}$ corresponds to the launching of SAWs. From Fig. 1.17a we determine $|S_{11}|^2\,(\text{EMW}) = 0.36$ and $|S_{11}|^2\,(\text{EMW}) = 0.17$ as the power reflection ratios without and with the launching of a SAW by the IDT. From these ratios we find that the electromagnetic wave generation efficiency is roughly 64%, while the efficiency for combined EMW and SAW generation is 83%. With $\eta = |S_{11}|^2\,(\text{EMW}) - |S_{11}|^2\,(\text{EMW} + \text{SAW}) = 0.19$ we can now calculate the total SAW power $P_{\text{SAW}} = \eta\frac{1}{2}P_{\text{rf}}$ for a rf power P_{rf} applied to the IDT. The factor $\frac{1}{2}$ is thereby introduced to account for the bidirectionality of the

IDT that results in the launching of two SAWs in opposite directions. The power P_{SAW} of the SAW that traverses the Ni film is shown in Fig. 1.17b (left scale, solid symbols) for the four investigated passbands at an rf power $P_{\mathrm{rf}} = 0.1\,\mathrm{mW}$ that was used for all magnetotransmission measurements discussed in this chapter. The total SAW power decreases for operation of the IDT at higher harmonic frequencies.

P_{SAW} gives rise to both, electric and mechanical displacements of the $LiNbO_3$ substrate [45]. The acoustic power P_{acoustic} of the SAW is $P_{\mathrm{acoustic}} = k^2 P_{\mathrm{SAW}}$, with the electromechanical coupling factor $k^2 = 5\%$ [45]. The normal component of the mechanical displacement at the surface of a SAW with acoustic power P_{acoustic} is given by [54]:

$$u_z^2 = \frac{P_{\mathrm{acoustic}}}{M 2\pi\nu W}\,, \tag{1.20}$$

with $M = 1.4 \times 10^{11}\,\mathrm{J/m^3}$ for $LiNbO_3$ [54] and the delay line width $W = 500\,\mu\mathrm{m}$. Furthermore, for a Raleigh SAW, the longitudinal component of the surface displacement is given by $u_x \approx \frac{2}{3} u_z$ [54]. From u_x we now calculate the pure strain $\varepsilon_x(x) = \frac{\partial u_x(x)}{\partial x}$ in a plane wave approximation $u_x(x) = u_x e^{-\mathrm{i}kx}$ with the wavevector $k = 2\pi/\lambda$. The magnitude $\varepsilon_x = k u_x$ of this strain is shown in Fig. 1.17b (right scale, open symbols) for the four investigated passbands. The maximum strain is thereby achieved at the 5^{th} harmonic. Now, according to Eq. (1.9), $\mu_0 H_{\mathrm{magel}}^{\mathrm{max}} = 2 B_1 \varepsilon_x$ for in-plane configuration ($\Theta_0 = 90°$), so that the maximum magnetoelastic driving field can be quantitatively derived with the magnetoelastic coupling constant $B_1 = 25.4\,\mathrm{T}$ [55] for Ni with a saturation magnetization $M_{\mathrm{s}} = 370\,\mathrm{kA/m}$ as determined by SQUID magnetometry by Matthias Althammer on similar Ni thin films. This yields a maximum virtual tickle field $\mu_0 H_{\mathrm{magel}}^{\mathrm{max}} \approx 30\,\mu\mathrm{T}$ for the 5^{th} harmonic at an rf level of $P_{\mathrm{rf}} = 0.1\,\mathrm{mW}$.

1.5.2 Comparison of experimental results and simulation

The coupling between the magnetization $\boldsymbol{M}$ and the SAW results in a resonant attenuation and phase shift of the SAW transmission when the condition for ferromagnetic resonance is met. To model this acoustically driven FMR, we evaluate the LLG (cf. Eq. (1.3)) numerically and take into account the magnetoelastic driving field $\boldsymbol{H}_{\mathrm{magel}}$.

The MATLAB package used for the numerical simulations and all calculations discussed below was conceived in collaboration with Lukas Dreher from the Walter Schottky Institut and my Diploma student Matthias Pernpeintner. A more detailed analysis of the model for acoustically driven FMR can be found in Ref. [53]. Here, only a brief

summary of the key ideas is given.

Our approach to model the acoustically driven FMR is formally identical to that used for conventional FMR. We thus write the absorbed rf power P as [27]

$$P = V_0 \frac{\mu_0 \omega}{2} \boldsymbol{H}^{\dagger}_{\mathrm{magel}} \overset{\leftrightarrow}{\chi} \boldsymbol{H}_{\mathrm{magel}} \,, \tag{1.21}$$

where the Polder susceptibility $\overset{\leftrightarrow}{\chi}$ is a function of the static anisotropy field F^{DC} defined in Eq. (1.1) and $\omega = 2\pi\nu$ is the SAW angular frequency. $V_0 = l_{\mathrm{Ni}} \cdot d_{\mathrm{Ni}} \cdot W = 1.5 \times 10^{-14}\,\mathrm{m}^3$ is the volume of the fraction of the Ni thin film perturbed by the SAW (cf. Fig. 1.10). We assume that the SAW is a uniform plane wave within V_0. This assumption is justified, as the Ni film thickness $d_{\mathrm{Ni}} = 50\,\mathrm{nm}$ is much smaller than the typical decaylength of the SAW into the bulk within $\lambda \geq 1.5\,\mu\mathrm{m}$. Equation (1.21) corresponds to the conventional FMR formula, but employs the purely virtual $\boldsymbol{H}_{\mathrm{magel}}(t)$ defined in Eq. (1.8) instead of an externally applied, real rf magnetic field. Thus, $\mathrm{Im}(P)$ is the power absorbed and $\mathrm{Re}(P)$ is the power dispersed in ferromagnetic resonance.

To obtain P as a function of the external magnetic field magnitude and orientation, we first calculate F^{DC} and F^{AC} (cf. Eqs. (1.1) and (1.7)). Numerical minimization of F^{DC} now yields the magnetization equilibrium orientation $\{\phi_0, \theta_0\}$. For this $\boldsymbol{M}$ orientation, the gradient of F^{AC} with respect to $\boldsymbol{m}$ yields $\boldsymbol{H}_{\mathrm{magel}}$ as shown in Eqs. (1.8) and (1.9).

For a quantitative simulation of acoustically driven FMR, the magnetic anisotropy and the damping constant of the ferromagnet needs to be considered. For the thin Ni film investigated in the experiment, we use a magnetic anisotropy with $B_{\mathrm{u}} = 2.5\,\mathrm{mT}$ with $\boldsymbol{u} = \boldsymbol{x}$ and $B_{\mathrm{d}} = 400\,\mathrm{mT}$. The in plane anisotropy B_{u} thereby is attributed to anisotropic thermal contraction of the lithium niobate substrate during the cooldown after the Ni deposition process. With these material parameters, we now exemplarily calculate $|\boldsymbol{H}_{\mathrm{magel}}|^2$ as shown in Fig. 1.18a. Note that, at large magnitudes of the external magnetic field $\boldsymbol{H}$ applied within the thin film plane, the magnetoelastic driving field is maximal for $\alpha = \pm 45°$. At these large $\boldsymbol{H}$ magnitudes, we find $\boldsymbol{M} \parallel \boldsymbol{H}$ and thus the anisotropy of the driving field mimics the four fold symmetry already introduced in Fig. 1.4. At small $\boldsymbol{H}$ magnitudes however, the magnetic anisotropy with a hard axis along $\boldsymbol{x}$ influences $\boldsymbol{M}$ orientation, so that the driving field shows a more complex anisotropy.

We now turn to the susceptibility $\overset{\leftrightarrow}{\chi}$. The susceptibility is a material parameter and

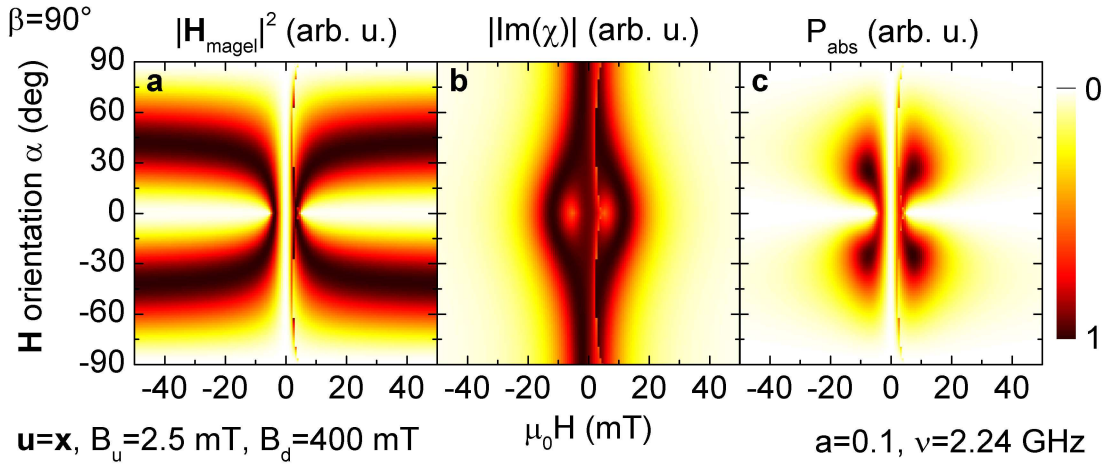

Figure 1.18: **a** Calculated magnetoelastic driving field $|\boldsymbol{H}_{\mathrm{magel}}|^2$ as a function of α and H. At high values of H ($\boldsymbol{M} \parallel \boldsymbol{H}$), H_{magel} shows the four-fold anisotropy found in Fig. 1.4. **b** Calculated $|\mathrm{Im}(\chi)|$, corresponding to conventional FMR with uniform tickle field. **c** Calculated $|\mathrm{Im}(P_{\mathrm{t}})| \propto |\boldsymbol{H}_{\mathrm{magel}}|^2 \cdot |\mathrm{Im}(\chi)|$.

thus independent of the driving field. We calculate the non-vanishing components of the Polder susceptibility in a linear driving field approximation as detailed in [53]. This yields

$$\overleftrightarrow{\chi} = \frac{\mu_0 M_{\mathrm{s}}}{D} \begin{pmatrix} F_{22}^{\mathrm{DC}} - F_3^{\mathrm{DC}} - \frac{\mathrm{i}\omega a}{\gamma} & -F_{12}^{\mathrm{DC}} - \frac{\mathrm{i}\omega}{\gamma} \\ -F_{12}^{\mathrm{DC}} + \frac{\mathrm{i}\omega}{\gamma} & F_{11}^{\mathrm{DC}} - F_3^{\mathrm{DC}} - \frac{\mathrm{i}\omega a}{\gamma} \end{pmatrix} , \tag{1.22}$$

with the determinant

$$D = \left(F_{22}^{\mathrm{DC}} - F_3^{\mathrm{DC}} - \frac{\mathrm{i}\omega a}{\gamma} \right) \left(F_{11}^{\mathrm{DC}} - F_3^{\mathrm{DC}} - \frac{\mathrm{i}\omega a}{\gamma} \right) - \left(F_{12}^{\mathrm{DC}} \right)^2 - \left(\frac{\omega}{\gamma} \right)^2 . \tag{1.23}$$

Here, we used the abbreviations $F_i^{\mathrm{DC}} = \partial_{m_i} F^{\mathrm{DC}}$ and $F_{ij}^{\mathrm{DC}} = \partial_{m_i} \partial_{m_j} F^{\mathrm{DC}}$. The partial derivatives of F^{DC} are evaluated at the equilibrium orientation of $\boldsymbol{M}$ ($m_3 = 1$, $m_1 = m_2 = 0$) and a is the dimensionless damping constant. Note that for the evaluation of $\overleftrightarrow{\chi}$, only the static anisotropy field F^{DC} needs to be considered. Exemplarily, we take the 13^{th} harmonic with $\omega = 2\pi\nu = 14.07\,\mathrm{GHz}$. For calculation of the gyromagnetic ratio $\gamma = g\mu_{\mathrm{B}}/\hbar$ we use $g = 2.185$ as the g-factor for Ni [56]. Finally we assume $a = 0.1$ as the damping parameter for calculation of $\overleftrightarrow{\chi}$. This value of a is comparatively large for two reasons. First it takes into account inhomogeneous broadening [57, 58] due

to the tickle field $\boldsymbol{H}_{\mathrm{magel}}$ being spatially inhomogeneous as the SAW wavelength is in the order of a few microns and the lateral dimensions of the Ni film are $l_{\mathrm{Ni}} = 600\,\mu\mathrm{m}$ (cf. Fig. 1.10). Second, an intrinsic FMR linewidth in the order of a few mT is experimentally found for bulk Ni [59] and our Ni thin films [60]. To account for this zero-frequency linewidth which is a major contribution at our comparatively low FMR frequencies ($\nu \leq 2.24\,\mathrm{GHz}$) we use an increased damping constant a.

While we use the full susceptibility tensor $\overleftrightarrow{\chi}$ in our simulations, for simplicity we consider only the scalar susceptibility $\chi := \overleftrightarrow{\chi}_{22}$ for a moment. In Fig. 1.18b, we plot $|\mathrm{Im}(\chi)|$ which corresponds to the FMR absorption. The influence of magnetic anisotropy leads to a shift of the FMR resonance field to higher values of $|H|$ at $\alpha = 0°$. Figure 1.18b shows the FMR absorption expected in conventional photon-driven FMR experiments with the electromagnetic tickle field $\boldsymbol{h}_1$ being applied perpendicular to $\boldsymbol{H}$. Now, in acoustically driven FMR, the absorbed power $P_{\mathrm{abs}} = \mathrm{Im}(P)$ is given by the multiplication of $|\boldsymbol{H}_{\mathrm{magel}}|^2$ with $|\mathrm{Im}(\chi)|$ (cf. Eq. (1.21)). This yields P_{abs} shown in Fig. 1.18c. Note that P_{abs} bears the characteristic angular dependency of $\boldsymbol{H}_{\mathrm{magel}}$. Furthermore, the maximum of P_{abs} is not necessarily identical to that of $|\mathrm{Im}(\chi)|$. Hence, the apparent resonance field in acoustically driven FMR is slightly different from the conventional FMR field.

We now turn to a quantitative comparison of our experimental results and the simulation introduced here. To this end, we calculate P as a function of $\boldsymbol{H}$ orientation and magnitude for the three SAW passband center frequencies 860 MHz, 1.55 GHz and 2.24 GHz using the strain, magnetoelasticity, magnetic anisotropy and damping already introduced. This yields a quantitative, completely parameter-free simulation of P_{abs} and P_{disp}.

To compare this simulation to our experimental data, we need to extract the measured absorbed and dispersed power. The absorbed power is derived from the change in $|S_{21}|$ as

$$P_{\mathrm{abs}}^{\mathrm{exp}}(\mu_0 H) = P_{\mathrm{SAW}} \left[1 - \left(\frac{|S_{21}|\,(\mu_0 H)}{|S_{21}|\,(\mu_0 H_{\mathrm{ref}})} \right)^2 \right] , \tag{1.24}$$

where P_{SAW} is taken from Fig. 1.17b. From Eq. (1.24) it follows that $P_{\mathrm{abs}}^{\mathrm{exp}}(\mu_0 H_{\mathrm{ref}}) = 0$ and $P_{\mathrm{abs}}^{\mathrm{exp}} \leq P_{\mathrm{SAW}}$. The maximum value of P_{abs} is observed at the resonance magnetic field $\mu_0 H_{\mathrm{res}}$, where $|S_{21}|$ is minimal (cf. Fig. 1.15b).

For the dispersion we use

$$P_{\mathrm{disp}}^{\mathrm{exp}}(\mu_0 H) = -\frac{1}{2} P_{\mathrm{abs}}^{\mathrm{exp}}(\mu_0 H_{\mathrm{res}}) \sin\left[\arg\left\{S_{21}\right\}(\mu_0 H)\right] \ , \tag{1.25}$$

where we set $\arg\left\{S_{21}\right\}(\mu_0 H_{\mathrm{ref}}) = 0$. The factor $\frac{1}{2}$ was thereby introduced to account for the ratio of the real and imaginary part of the complex susceptibility [61]

$$\max\left\{\mathrm{Im}(\chi)\right\} = \mathrm{Im}(\chi)(\mu_0 H_{\mathrm{res}}) = 2\mathrm{Re}(\chi)(\mu_0 H_{\mathrm{res}} + a\mu_0 H_{\mathrm{res}}) = 2\max\left\{\mathrm{Re}(\chi)\right\} \ .$$

We note that the expressions for P_{abs} and P_{disp} given in Eqs. (1.24) and (1.25) do not take the backaction of the magnetization dynamics on the SAW into account. However, we measure the amplitude and phase of the SAW and not that of the magnetization. In Ref. [53] this issue is discussed in more detail and a backaction model is introduced, so that the measured complex S-parameter can be simulated directly. It is found that Eq. (1.24) still holds in good approximation and Eq. (1.25) gives nearly the same qualitative evolution and quantitatively agrees to the backaction model within a factor of about two. We thus carry out our simulations based on Eq. (1.21).

We first compare the experimental results obtained for an in-plane rotation of $\boldsymbol{H}$ to corresponding simulations. Both, experimentally obtained and simulated P_{abs} and P_{disp} are shown in Fig. 1.19 for 860 MHz, 1.55 GHz and 2.24 GHz. We use $a = 0.1$, ε_x from Fig. 1.17, $B_{\mathrm{u}} = 2.5\,\mathrm{mT}$, $\boldsymbol{u} = (1, 0, 0)$ and $B_{\mathrm{d}} = 400\,\mathrm{mT}$ for the simulation. Overall, excellent agreement of simulation and measurement data is observed considering the simplicity of the model. The simulation reproduces the characteristic four-fold symmetry of the acoustically driven FMR. Furthermore, the evolution of P with frequency mimics the experimental observations.

To obtain a complete picture of the anisotropy of the elastically driven ferromagnetic resonance, we furthermore performed experiments with $\boldsymbol{H}$ being applied in the plane spanned by the SAW propagation direction $\boldsymbol{k}_{\mathrm{SAW}} \parallel \boldsymbol{x}$ and the film normal $\boldsymbol{z}$. Hence, $\alpha = \text{const.} = 0°$ and $-90° \leq \beta \leq 90°$, which yielded the measurement data and simulations shown in Fig. 1.20. Most remarkably, the acoustically driven FMR vanishes ($P_{\mathrm{abs}} = 0$) for $\beta = 0°$ while the most intense FMR is observed in the vicinity of this orientation. The fact that the most intense FMR is observed for $|\beta| \ll 45°$ is due to the comparatively large out-of-pane anisotropy field $B_{\mathrm{d}} = 400\,\mathrm{mT}$. This causes the equilibrium orientation θ_0 of $\boldsymbol{M}$ to be $\theta_0 = 45°$ for β close to 0°. Again, all salient

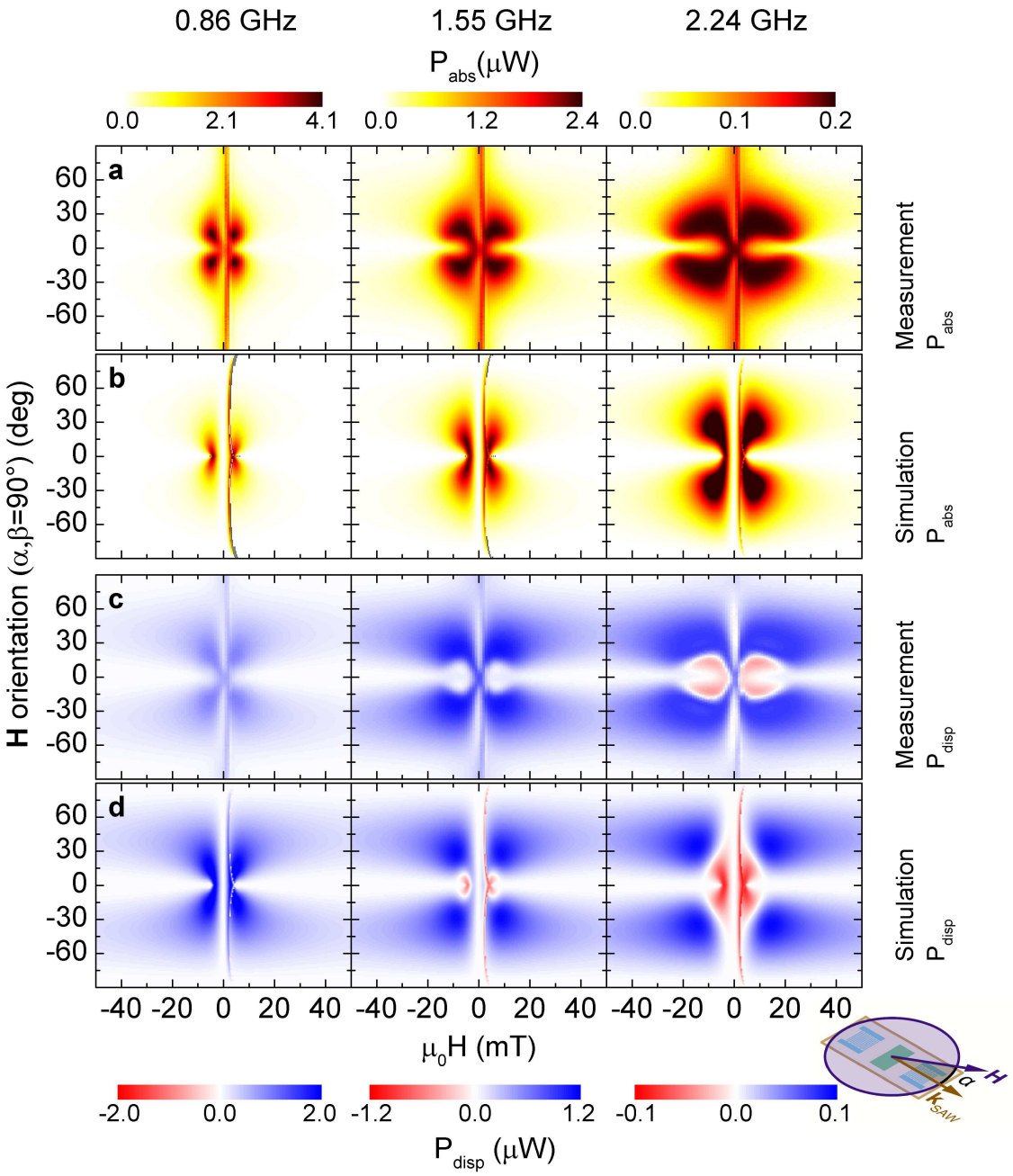

Figure 1.19: **a** Measured P_{abs} as a function of in-plane $\boldsymbol{H}$ orientation α ($\beta = 90°$) and H for 860 MHz, 1550 MHz and 2240 MHz, respectively. **b** Quantitative simulation of P_{abs}. **c** The measured P_{disp}. **d** Quantitative simulation of P_{disp}.

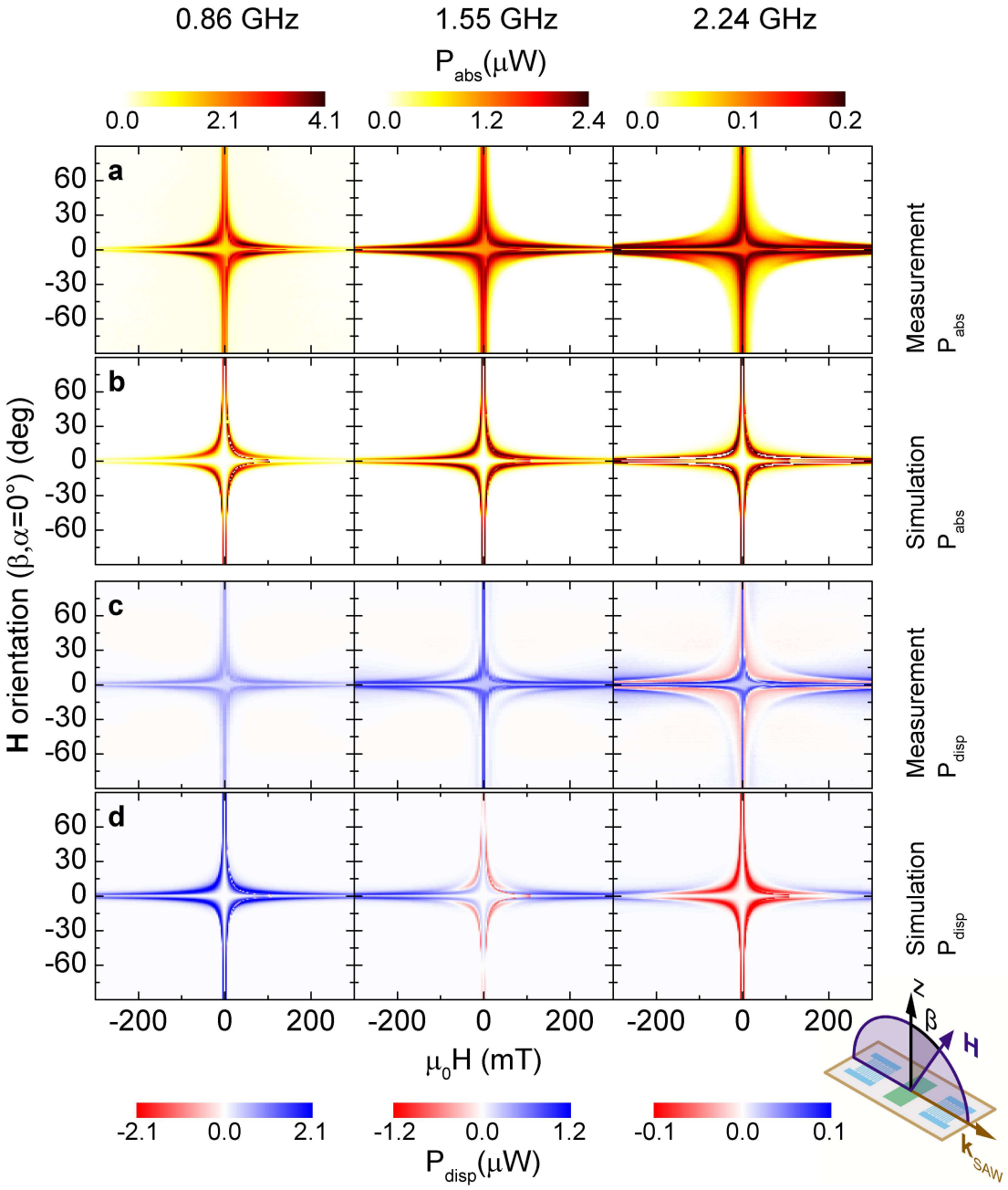

Figure 1.20: **a** Measured P_{abs} as a function of out-of-plane $\boldsymbol{H}$ orientation β ($\alpha = 0°$) and H for 860 MHz, 1550 MHz and 2240 MHz, respectively. **b** Quantitative simulation of P_{abs}. **c** The measured P_{disp}. **d** Quantitative simulation of P_{disp}.

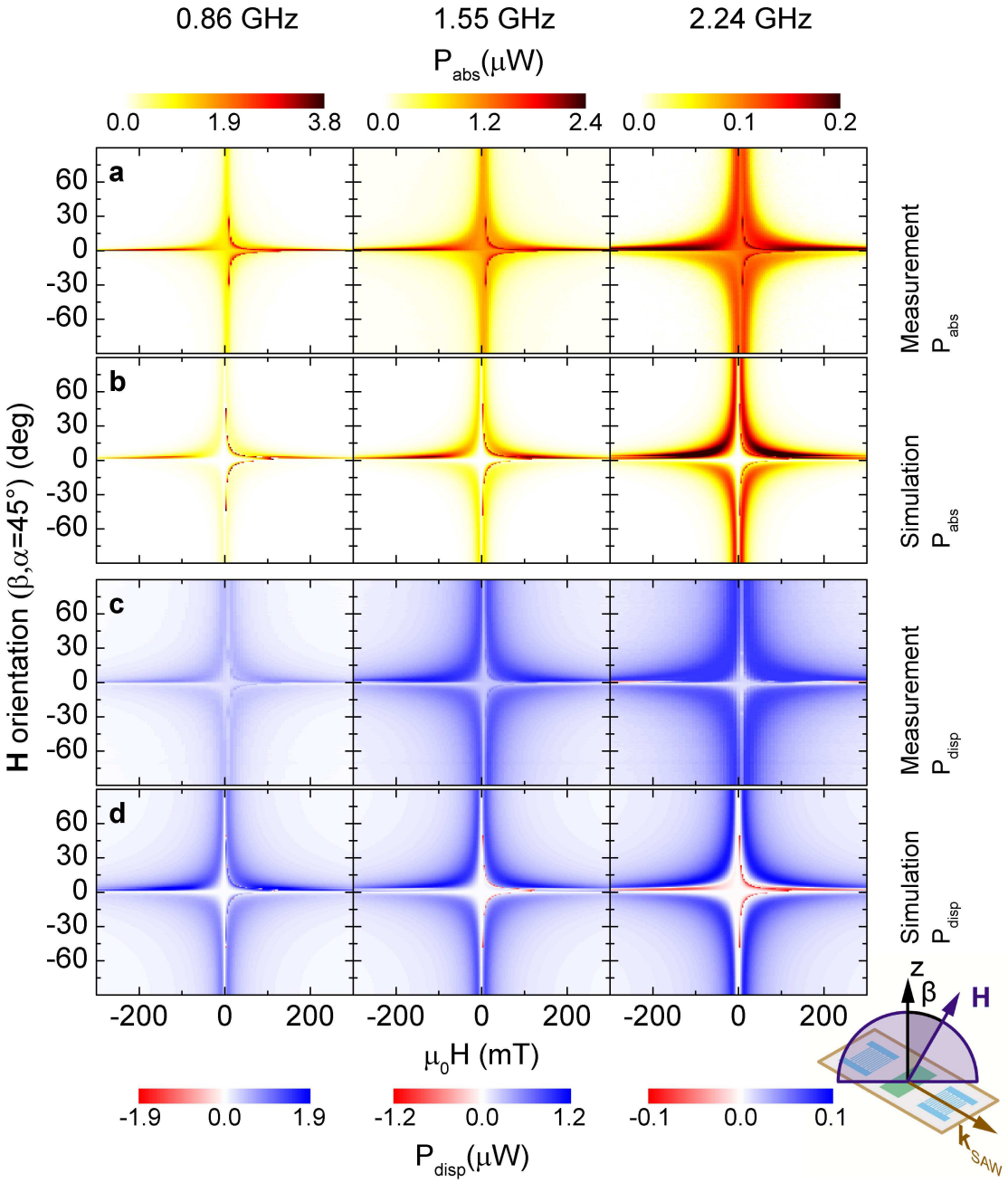

Figure 1.21: **a** Measured P_{abs} as a function of out-of-plane $\boldsymbol{H}$ orientation β ($\alpha = 45°$) and H for 860 MHz, 1550 MHz and 2240 MHz, respectively. **b** Quantitative simulation of P_{abs}. **c** The measured P_{disp}. **d** Quantitative simulation of P_{disp}.

features of the experimental data are quantitatively reproduced in the simulation. All parameters were identical to that used for the simulation of the in-plane data.

Finally, we performed measurments and corresponding model calculations for $\boldsymbol{H}$ being rotated from the $\boldsymbol{z}$-axis to an in-plane orientation where $\boldsymbol{H}$ encloses an angle of 45° with the SAW propagation direction ($\alpha = \text{const.} = 45°$ and $-90° \leq \beta \leq 90°$). We obtained the simulations and experimental results depicted in Fig. 1.21. Note that the small asymmetry in P_{abs} and P_{disp} for positive and negative β was caused by a tilting of 2° of the sample in the setup which is reproduced in the simulation. Once more, full quantitative agreement of simulation and measurement is found.

Taken together, the excellent agreement of our simulations and experiments strongly corroborates the interpretation of our measurement data on the basis of acoustically driven FMR. With just one set of plausible or independently measured parameters, it was possible to quantitatively model the acoustically driven FMR for all experimentally investigated $\boldsymbol{H}$ configurations. Small differences of simulation and experimental data are mainly observed in the linewidth, which is not surprising considering the simple phenomenological model that considers only the Gilbert-damping contribution to the FMR linewidth. We use a large Gilbert damping constant to account for line broadening due to inhomogeneities of either driving field $\boldsymbol{H}_{\text{magel}}$ or magnetic anisotropy [62–64] as well as for additional damping channels, i.e., two magnon processes [65, 66].

1.6 Conclusions and outlook

In conclusion, we have consistently found both in experiment and in simulation that the magnetoelastic interaction of a SAW with a ferromagnetic thin film allows to excite FMR in the latter. The FMR is driven acoustically in the sense that no external rf magnetic field is applied to the ferromagnet. Rather, a purely internal rf magnetic field arises due to magnetoelastic coupling between the SAW elastic strain field and the ferromagnet. Using a free energy approach as well as LLG calculations, we showed that the magnitude of the "acoustic" rf magnetic field characteristically depends on the equilibrium orientation of the magnetization. The angular dependence of the SAW transmission thus is a fingerprint of acoustic FMR, as observed in our experiments and corroborating quantitative simulations. Our experimental findings open a third alternative for the excitation of FMR, in addition to externally applied rf magnetic fields [16, 67] or the spin torque effect [68–72]. In future studies it appears appealing to investigate the acoustically driven FMR in the limit of a homogeneous

tickle field, i.e., in ferromagnetic thin films with lateral dimensions smaller than the acoustic wavelength. Furthermore, the interaction of magnetoelastic materials with shear surface acoustic waves is predicted to show a distinctly different symmetry of the acoustically driven FMR by our model [53]. This regarding, corresponding experiments need to be carried out to verify the predictive power of our simulations. The use of appropriate substrate materials may furthermore allow for the investigation of acoustic FMR in epitaxially grown ferromagnetic thin films. This might be particularly interesting for diluted ferromagnetic semiconductors such as (Ga,Mn)As. It is even possible to transfer the surface acoustic wave from one substrate material to another [73]. It hence should be possible to excite and detect the SAW all electrically on a piezoelectric substrate, while investigating acoustically driven FMR in a ferromagnetic thin film grown on an non-piezoelectric substrate, i.e., yttrium iron garnet thin films on gadolinium gallium garnet.

More fundamentally, acoustic FMR could be a pathway for the study of magnon-phonon interaction phenomena such as mechanical spin pumping [74,75] in solid state-based microstructures. This particular phenomenon is investigated in the following chapter. Furthermore, the coupling between elastic and magnetic degrees of freedom will open additional channels for spin dephasing, so that the magnetization damping is linked to the magnon-phonon coupling strength. Finally, a detailed study of the interaction between magnonic and phononic dispersions, of the strength of the coupling, of the anticrossing of these branches and of the generation of strongly coupled elastic/magnetic states are appealing challenges for the future. For an experimental investigation of said strong coupling phenomena, SAW resonators [44] are a viable option as detailed in Chapter 4. Hence, more advanced SAW device designs will be an important step towards the understanding of fundamental phonon-magnon interaction phenomena. Apart from SAW resonators, more advanced devices may allow for the generation of SAWs at almost arbitrary rf frequencies, allowing for a broadband detection of acoustically driven FMR. This will open the path for applications of this technique for the investigation of magnetic damping and anisotropy in micro- or nanopatterned magnetoelastic media in micron-scale integrated devices.

Chapter 2

Spin pumping with coherent elastic waves

Today's electronic devices use charge currents to store, retrieve and process information. As electrons bear a spin in addition to their charge, future information processing devices may use spin currents - that is a flux of spin rather than charge - for novel functionality. Such spintronic devices in the proper sense of the word offer conceptual advantages over their electronic counterparts since spin currents can be transmitted with very little dissipation even in electric insulators [76, 77], thus reducing waste heat and allowing further device miniaturization. Hence, spin currents are vigorously investigated for the injection and transportation of spin information [76,78–82]. In ferromagnet/metal hybrid devices, a spin current can be generated across the ferromagnetic/metallic interface by the relaxation of a resonantly precessing magnetization. This effect is referred to as spin pumping [76, 83–88]. In this approach, electromagnetic waves in the GHz regime, i.e., microwave *photons* are used to resonantly excite magnetization dynamics in a ferromagnet (FM) and thus drive a spin current into an adjacent normal metal (N).

Here we show that the resonant absorption of elastic waves, i.e., microwave *phonons* in a FM/N bilayer can be used to acoustically drive a spin current. This establishes the spin current generation by a resonant phonon-magnon coupling and thus an interaction of lattice and spin degrees of freedom. In this sense, acoustic spin pumping can be seen as a resonant analogue of the spin Seebeck effect [89] where a non-resonant lattice excitation due to a temperature gradient drives a spin current.

We would like to emphasize that very recently Uchida *et al.* observed *non-resonant* acoustic spin pumping in a ferromagnetic insulator [90,91]. Their findings are comple-

mentary to the results discussed in this chapter, as said authors studied the phonon-spin pumping at frequencies of a few MHz and thus far below ferromagnetic resonance (FMR). Most importantly, our experimental approach allows us to tune our system in and out of FMR via the application of a dc external magnetic field. As detailed below, we find that a spin current can be generated if the condition for acoustically driven FMR is met. However, within our experimental sensitivity limit, we found no evidence for the off-resonant acoustic spin pumping reported in Refs. [90,91]. Our findings are thus in accordance to the expectations from conventional photon-driven-FMR spin pumping experiments [76, 83–88]. The resonant phonon-spin current conversion discussed in this chapter opens intriguing perspectives for applications in, e.g., microelectromechanical resonators, since radio frequency elastic deformations can now be used for spin current generation. The main results presented in this chapter have been published in Ref. [36].

2.1 Introduction and physical concepts

Spin pumping with elastic waves incorporates a set of physical principles. A pure spin current needs to be generated all elastically and detected electrically. The generation and detection of a surface acoustic wave (SAW) in ferroelectric substrate/ferromagnetic thin film hybrids was already discussed in the previous chapter. Here, we again use such a SAW as a coherent source of phonons in the ferromagnetic thin film (FM). The SAW drives the magnetization dynamics in the FM [37] and, in the acoustic spin pumping configuration introduced in this chapter, the elastically driven ferromagnetic resonance (FMR) relaxes via the emission of a spin current into a thin normal metal film (N) deposited on top of the FM. We exploit the inverse spin Hall effect [92,93] in the normal metal for conversion of said spin current into a charge current which can be detected electrically. In the following, the concepts of acoustic spin pumping and the (inverse) spin Hall effect are briefly discussed.

2.1.1 Acoustic spin pumping

In analogy to Archimedes' screw which pumps a fluid by rotational motion, a precessing magnetization can "pump" angular momentum, or spin. While the mechanical pump transports fluid from one liquid reservoir to another, the "spin pump" transports angular momentum from a ferromagnet into a normal metal [94]. This spin

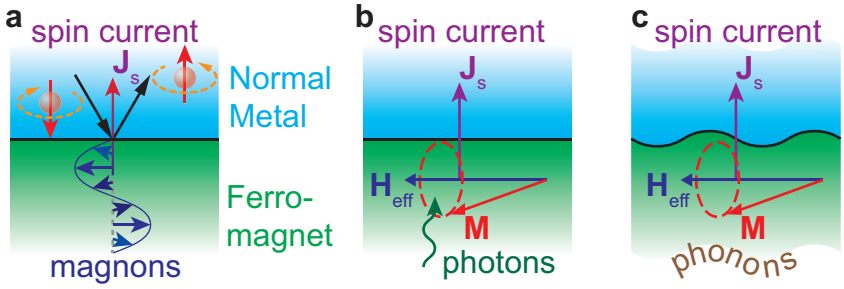

Figure 2.1: **a** Principle of spin pumping. A transfer of angular momentum of the magnon in the ferromagnet to the charge carriers in the normal metal results in a spin-current $\boldsymbol{J}_\mathrm{s}$ across the interface. **b** Photon-driven spin pumping effect. Microwave photons drive the resonant magnetization $\boldsymbol{M}$ precession which relaxes via the emission of $\boldsymbol{J}_\mathrm{s}$. **c** Phonon-driven spin pumping effect. An elastic wave drives the resonant $\boldsymbol{M}$ precession which relaxes via the emission of $\boldsymbol{J}_\mathrm{s}$.

transportation may either occur through two spin-polarized charge currents flowing in opposite directions in normal metals such that the net charge current cancels, or through a collective spin precession mode represented by a spin wave in ferromagnets. In total, spin pumping is a conversion of spin angular momentum of resonantly excited magnons into a directed spin current. Thus, spin pumping is the inverse of the spin transfer torque effect [95–97], where a spin polarized dc current drives magnetization dynamics. The spin pumping effect is depicted schematically in Fig. 2.1a, where a spin current $\boldsymbol{J}_\mathrm{s}$ is generated across a ferromaget/normal metal interface by transfer of the ferromagnetic spin-wave torque to the electron spins in the normal metal.

In the normal metal, two antiparallel charge currents with "spin up" and "spin down", respectively, exist. The total, net charge current thus vanishes, while in this picture, "spin up" is transported away from the interface. The direction of $\boldsymbol{J}_\mathrm{s}$ is assumed to be the direction of "spin up" transportation. Now, in this process, the magnons transfer their angular momentum to the conduction electrons in the metal such that the magnetization precession is damped [84]. Hence, in the absence of an external magnetization driving force, $\boldsymbol{J}_\mathrm{s} = 0$ in equilibrium. One may now use externally applied microwave photons to excite resonant magnetization precession. Thus, in ferromagnetic resonance (FMR) a static dc spin current $\boldsymbol{J}_\mathrm{s}$ is generated as depicted in Fig. 2.1b. This *photon*-driven spin pumping has been observed in conductive, insulating or semiconducting ferromagnets [76, 83–88]. However, as shown below, spin currents can also be generated in the absence of external microwave photons by exploiting *phonon*-driven ferromagnetic resonance (cf. Chapter 1). Here, a

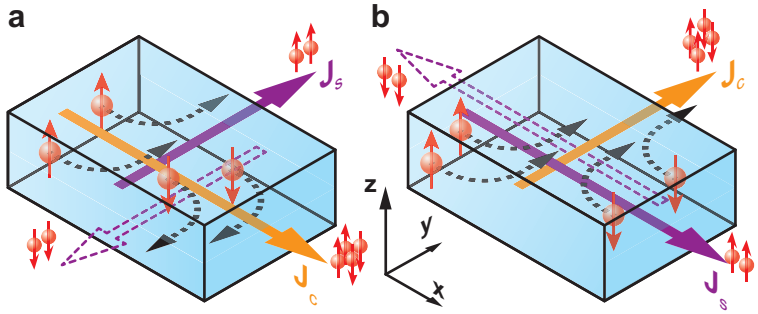

Figure 2.2: **a** Spin Hall effect. A charge current $\boldsymbol{J}_c$ is a flow of charge carriers the net spin moment of which vanishes. Due to the spin orbit interaction, spin "up" and "down" are deflected in opposite directions, resulting in a pure spin current $\boldsymbol{J}_s$ orthogonal to $\boldsymbol{J}_c$. Here, $\boldsymbol{J}_s$ is the net flow of spin up moments. **b** Inverse spin Hall effect. As a direct consequence of the spin Hall effect, a spin current $\boldsymbol{J}_s$ gives rise to an orthogonal charge current $\boldsymbol{J}_c$.

surface acoustic wave (SAW) is used as a phonon-source and provides the magnetoelastic magnetization driving field. Hence, as depicted in Fig. 2.1c, it is possible to elastically excite a ferromagnet and thus generate a spin-current. An experimental investigation of this acoustic spin pumping effect is the focus of this chapter.

Note however, that the observation of the elastically driven spin current requires its conversion to a charge current to enable electrical detection. This spin-charge conversion is achieved by exploiting the inverse spin Hall effect discussed in the following.

2.1.2 The spin Hall effect

Electrons bear a spin degree of freedom in addition to their charge. Hence, electric currents can be spin polarized, i.e., a flux of electrons the majority of which carry identical spin. These spin polarized currents are observed in materials where an imbalance of charge carrier spins exist at the Fermi level. Even more intriguing, it was predicted already in 1971 [98] and later rediscovered [92] that the spin-orbit interaction [99–102] may give rise to a pure spin current - that is a flux of spin without flux of charge - which is driven by a non-polarized charge current. In other words, in materials with spin-orbit interaction, any charge current is accompanied by a spin current and vice versa. Experimentally, this so called spin Hall effect was first observed in 2004 [81]. Here, only a brief phenomenological description of the spin Hall effect will be given.

Consider a slab of a normal metal in a cartesian coordinate system where electrons with spin orientation "up" and "down" (here assumed along $\pm\boldsymbol{z}$ as depicted in Fig. 2.2a), are the charge carriers. A pure (non-polarized) charge current $\boldsymbol{J}_\mathrm{c} \parallel \boldsymbol{x}$ thus comprises an equal number of spin up and down electrons that all move in positive $\boldsymbol{x}$ direction. Now, spin-orbit interaction mechanisms, such as skew scattering [103], side-jump scattering [104] and intrinsic interactions [105, 106], all result in a force on the electrons, the direction of which is perpendicular to both, the electron propagation direction $\boldsymbol{x}$ and spin orientation $\boldsymbol{\sigma} \in \{-\boldsymbol{z}, +\boldsymbol{z}\}$. Hence, spin up and spin down electrons are deflected in opposite directions. In Fig. 2.2a, spin up electrons are deflected along $+\boldsymbol{y}$ and spin down electrons along $-\boldsymbol{y}$. This results in a pure spin current $\boldsymbol{J}_\mathrm{s} \parallel +\boldsymbol{y}$. Note that spin down electron movement $\boldsymbol{J}_\mathrm{s}^\downarrow$ is always antiparallel to the spin up electron movement $\boldsymbol{J}_\mathrm{s}^\uparrow$, making it sufficient to describe movement of both, spin up and down electrons, by a single spin current $\boldsymbol{J}_\mathrm{s} = \boldsymbol{J}_\mathrm{s}^\uparrow - \boldsymbol{J}_\mathrm{s}^\downarrow$. As an equal number of electrons, all of which bear identical charge $-e$ move along $\boldsymbol{y}$ and $\boldsymbol{-y}$, no net charge current is generated in the direction of $\boldsymbol{J}_\mathrm{s}$. Hence, the charge current $\boldsymbol{J}_\mathrm{c}$ gives rise to a spin current $\boldsymbol{J}_\mathrm{s}$ of electrons perpendicular to both, $\boldsymbol{J}_\mathrm{c}$ and $\boldsymbol{\sigma}$.

Now,consider a pure spin current $\boldsymbol{J}_\mathrm{s} \parallel \boldsymbol{x}$ with spin up electrons flowing along $+\boldsymbol{x}$ while spin down electrons flowing along $-\boldsymbol{x}$. Hence both, spin direction and direction of movement are opposite for spin down and spin up electrons. They are thus both deflected along the same direction, yielding a charge current $\boldsymbol{J}_\mathrm{c} \parallel \boldsymbol{y}$ as depicted in Fig. 2.2b. We conclude that in conductive materials with spin-orbit coupling, any spin current is accompanied by a perpendicular charge current and vice versa. In total, this interconversion of charge and spin currents is phenomenologically governed by the following equations [107]:

$$\boldsymbol{J}_\mathrm{s} = \alpha_\mathrm{SH} \left(-\frac{\hbar}{2e}\right) \boldsymbol{J}_\mathrm{c} \times \boldsymbol{\sigma} \tag{2.1}$$

$$\boldsymbol{J}_\mathrm{c} = \alpha_\mathrm{SH} \left(-\frac{2e}{\hbar}\right) \boldsymbol{J}_\mathrm{s} \times \boldsymbol{\sigma} \ , \tag{2.2}$$

where the spin Hall angle α_SH is a material parameter, $e > 0$ is the elementary charge and $\hbar$ is the Planck constant h divided by 2π. One usually refers to the conversion of a charge to a spin current in Eq. (2.1) as the spin Hall effect, while its counterpart in Eq. (2.2) is called the inverse spin Hall effect. As can be seen from Eq. (2.2), the inverse spin Hall effect allows for an all electrical detection of a spin current in a normal metal [93].

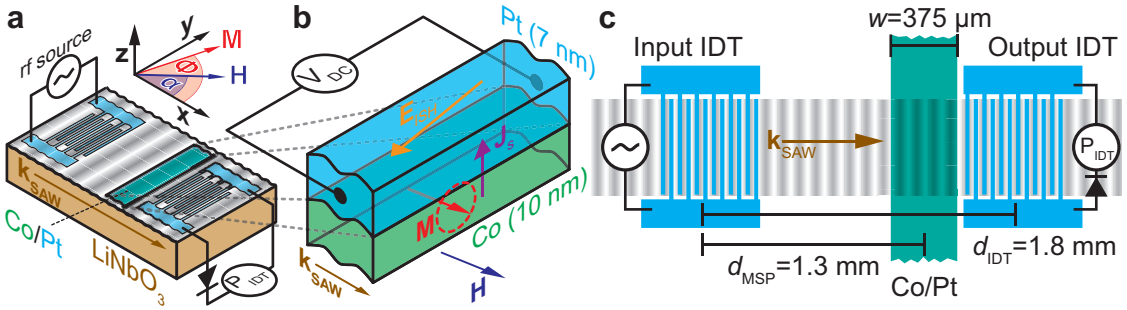

Figure 2.3: **a** Schematic view of $LiNbO_3$/Co/Pt hybrid. An external static magnetic field $\boldsymbol{H}$ can be applied within the film plane at an angle α to the SAW propagation direction. **b** The SAW drives resonant magnetization $\boldsymbol{M}$ precession that emits a spin current $\boldsymbol{J}_s$ into the Pt. $\boldsymbol{J}_s$ is detected via the inverse spin Hall effect in the Pt thin film, i.e., as the voltage V_{DC}. **c** Sample geometry (not to scale).

2.2 Sample fabrication and experimental setup

For the experimental observation of an acoustically pumped spin current, we employ the sample schematically depicted in Fig. 2.3a. It consists of a Co (10 nm)/Pt (7 nm) bilayer deposited by electron beam evaporation on a 500 µm thick y-cut $LiNbO_3$ crystal between two Al (70 nm) interdigital transducers (IDTs) with a periodicity of 20 µm. The IDTs with a fundamental frequency of $\nu_0 = 172$ MHz were fabricated as detailed in Chapter 1 with an aperture of 500 µm. Two opposing IDTs form an acoustic delay line which is operated at its 9^{th} harmonic frequency $\nu = 1.548$ GHz at room temperature. Thus, the excited SAW features a wavelength $\lambda = 2.2$ µm. The sample is mounted on the chip-carrier shown in Fig. 1.11b, and three semi-rigid rf coaxial cables are used to contact input IDT, output IDT and bilayer. By wire bonding to the ground plane on the chip carrier, a common signal ground was established for one end of the bilayer and one of each IDT's electrode arrays. In contrast to the vector-network-analysis experiments discussed in the previous chapter, we here use a Rohde & Schwarz SMB100A microwave source to drive the input IDT and an Anritsu 70KC50 microwave diode to probe the rf power P_{IDT} at the output IDT. More precisely, the voltage output of the microwave diode is amplified by a minicircuits ZFL-1000 18 dB rf amplifier and a diode calibration was performed to compute P_{IDT}, which we will discuss in the following. Hence, P_{IDT} is a measure for the SAW transmission and can be used to probe acoustically driven FMR in the Co/Pt bilayer. Now, the resonant magnetoelastic magnetization $\boldsymbol{M}$ precession in

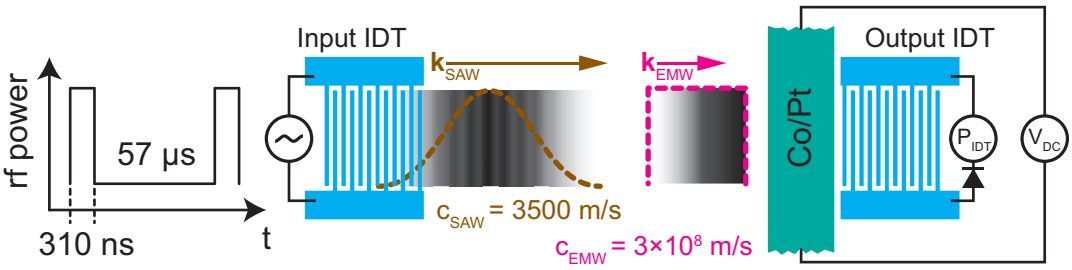

Figure 2.4: Rf pulses are applied to the input IDT which emits SAW and EMW pulses. Due to their vastly different propagation velocities, $c_{\mathrm{SAW}} \ll c_{\mathrm{EMW}}$, their contributions to V_{DC} and P_{IDT} can be separated in a time-resolved study.

the Co layer can relax via the emission of a spin current $\boldsymbol{J}_{\mathrm{s}}$ into the normal metal (Pt) [84] as depicted in Fig. 2.3b. We detect $\boldsymbol{J}_{\mathrm{s}}$ along $\boldsymbol{z}$ via the inverse spin Hall effect as discussed above, which results in an electric field $\boldsymbol{E}_{\mathrm{ISH}} \propto \boldsymbol{M} \times \boldsymbol{J}_{\mathrm{s}}$. We measure $V_{\mathrm{DC}} \propto \boldsymbol{E}_{\mathrm{ISH}} \cdot \boldsymbol{y}$ after amplification with a FEMTO DHPVA variable gain voltage amplifier set to a gain of 40 dB and a bandwidth of 20 MHz.

In the sample geometry depicted in Fig. 2.3c, a direct measurement of V_{DC} and P_{IDT} is obstructed by spurious effects caused by the electromagnetic wave (EMW) which is launched at the input IDT simultaneously to the SAW. These spurious effects include the interference of SAW and EMW at the output IDT already discussed in Chapter 1. Furthermore, the voltage V_{DC} bears contributions due to microwave rectification effects in the Co/Pt bilayer [75, 108, 109] in the presence of an EMW. To separate *photon*-driven from *phonon*-driven effects, we here perform a time-resolved experiment. To this end, we apply rf pulses to the input IDT as depicted in Fig. 2.4 and study the time dependent evolution of V_{DC} and P_{IDT} using a two channel oscilloscope (Gage Razor CompuScope 1622). For improved signal-to-noise ratio, we use the oscilloscope's internal FPGA[1] to average data obtained in 1024 pulse cycles. This data is again averaged 32 times in the measurement software and several external magnetic field sweeps are performed and averaged. For the generation of the SAW pulses we apply +30 dBm rf pulses with $\nu = 1.548$ GHz, a pulse width $t_{\mathrm{w}} = 310$ ns and a pulse period $t_{\mathrm{r}} = 57.3$ µs to the input IDT. The input IDT launches a SAW and an EMW with the application of each rf pulse. Now, the SAW propagates with the speed of sound, $c_{\mathrm{SAW}} \approx 3.5 \times 10^3$ m/s, while the EMW propagates with the speed of light, $c_{\mathrm{EMW}} \approx 3 \times 10^8$ m/s. Both pulses can be clearly separated in the

[1] A Field-Programmable Gate Array (FPGA) is an electronic circuit the functionality of which can be programmed after manufacturing.

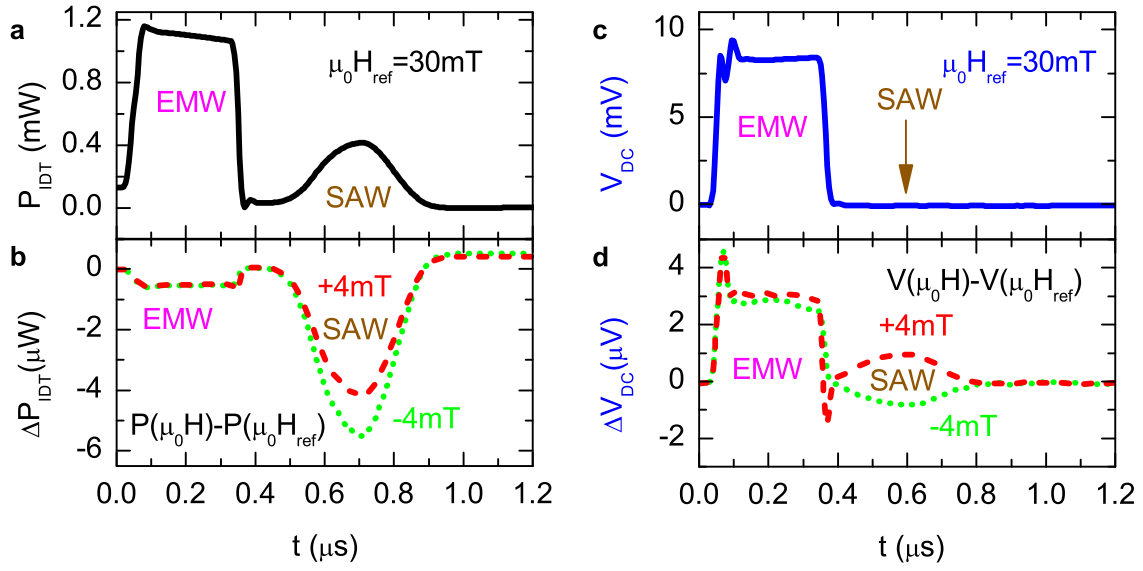

Figure 2.5: Time resolved spectroscopy with $\boldsymbol{H}$ applied at $\alpha = 10°$. **a** P_{IDT} as a function of time with $\mu_0 H_{\mathrm{ref}} = 30\,\mathrm{mT}$, showing the detection of the electromagnetic wave (EMW, 0.2 µs) and the surface acoustic wave (SAW, 0.7 µs) pulses at the output IDT. **b** $\Delta P_{\mathrm{IDT}}(t) = P_{\mathrm{IDT}}(t, \mu_0 H) - P_{\mathrm{IDT}}(t, \mu_0 H_{\mathrm{ref}})$. $\Delta P_{\mathrm{IDT}}(0.7\,\mu\mathrm{s}) < 0$ shows that the SAW is damped for $\mu_0 H_{\mathrm{res}} = \pm 4\,\mathrm{mT}$, indicating acoustically driven FMR. **c** V_{DC} as a function of time at $\mu_0 H_{\mathrm{ref}} = 30\,\mathrm{mT}$. The EMW is rectified at the bilayer. **d** $\Delta V_{\mathrm{DC}}(t) = V_{\mathrm{DC}}(t, \mu_0 H) - V_{\mathrm{DC}}(t, \mu_0 H_{\mathrm{ref}})$. The change of sign of $\Delta V_{\mathrm{DC}}(0.6\,\mu\mathrm{s})$ with reversal of **H** direction is a signature of acoustic spin pumping.

time domain as they are expected to show a temporal separation of approximately 400 ns at the bilayer ($d_{\mathrm{MSP}} = 1.3\,\mathrm{mm}$) and of approximately 500 ns at the output IDT ($d_{\mathrm{IDT}} = 1.8\,\mathrm{mm}$). We use the identical electromagnet and rf dipstick as introduced in the previous chapter to provide magnetic field and rf wiring. Thus, in particular, changing magnetic field orientation does not involve a movement of the sample which would result in bending of the rf-wiring and thus impede reproducible measurement results. By studying $P_{\mathrm{IDT}}(t)$ and $V_{\mathrm{DC}}(t)$ for various external magnetic field $\boldsymbol{H}$ orientations and magnitudes we can unambiguously identify phonon driven spin-pumping as shown in the following.

2.3 Experimental results and discussion

We first address how the contributions to P_{IDT} and V_{DC} related to SAW and EMW can be separated. As we detect two measurands (P_{IDT} and V_{DC}) and both SAW and EMW contribute to each of these, we will identify a total of four contributions. In the magnetic field dependent measurement data $\Delta P_{\mathrm{IDT}} = P_{\mathrm{IDT}}(\mu_0 H) - P_{\mathrm{IDT}}(\mu_0 H_{\mathrm{ref}})$ these will be referred to as ΔP_{SAW} and ΔP_{EMW} for SAW and EMW, respectively. Correspondingly, for $\Delta V_{\mathrm{DC}} = V_{\mathrm{DC}}(\mu_0 H) - V_{\mathrm{DC}}(\mu_0 H_{\mathrm{ref}})$ we will identify ΔV_{MSP} and ΔV_{MR} as the contributions to V_{DC} from mechanical (SAW) spin pumping and EMW microwave rectification, respectively.

In Fig. 2.5a we show the rf power P_{IDT} transmitted across the delay line as a function of time t for application of $\boldsymbol{H}$ at $\alpha = 10°$. In the displayed data, the rf pulse commences at $t = 0$. As the SAW has a velocity of $c_{\mathrm{SAW}} = 3440\,\mathrm{m/s}$ and the sample features a center to center IDT spacing of $d_{\mathrm{IDT}} = 1.8\,\mathrm{mm}$ (cf. Fig. 2.3a), the SAW transit time from input IDT to output IDT is $t_{\mathrm{t}} = 0.52\,\mu\mathrm{s}$. In contrast, the EMW propagates with the speed of light and is thus expected to appear almost instantaneously with the start of the microwave pulse at $t \approx 0$. Indeed, in the $P_{\mathrm{IDT}}(t)$ trace shown in Fig. 2.5a, two signals are observed, the first of which begins at $t \approx 0$ and is attributed to the reception of the EMW at the output IDT. This electromagnetic crosstalk was already encountered and discussed in the previous chapter. The rectangular shape and duration mimics the applied microwave pulse. Around $t = t_{\mathrm{SAW}} = 0.7\,\mu\mathrm{s}$ a Gaussian pulse of smaller magnitude is recorded. This pulse is due to the SAW reaching the output transducer. The pulse-shape is Gaussian rather than rectangular due to the finite length of the transducers and the low SAW propagation velocity. This can be understood as, during a pulse length of $t_{\mathrm{w}} = 310\,\mathrm{ns}$, the SAW travels for approximately 1 mm. Hence, at any time, a certain fraction of the output IDT is excited by the SAW as it passes underneath it, resulting in the observed pulse shape. Note that the SAW pulse is clearly separated from the EMW pulse in the time domain. This allows us to distinguish between photon and phonon driven contributions to $P_{\mathrm{IDT}}(t)$.

To show this in more detail, we investigate the magnetic field dependence of P_{IDT} shown in Fig. 2.5b. Here we plot $\Delta P_{\mathrm{IDT}} = P_{\mathrm{IDT}}(\mu_0 H) - P_{\mathrm{IDT}}(\mu_0 H_{\mathrm{ref}})$. We use $\mu_0 H_{\mathrm{ref}} = 30\,\mathrm{mT}$ as the reference magnetic field and investigate data obtained at the FMR magnetic field $\mu_0 H_{\mathrm{res}} = \pm 4\,\mathrm{mT}$ at $\nu_{\mathrm{SAW}} = 1.55\,\mathrm{GHz}$ (dashed and dotted line, respectively). For both values of H, one observes a pronounced dip in ΔP_{IDT} at t_{SAW}.

This SAW attenuation is attributed to acoustically driven FMR, which results in a damping of the SAW as detailed in Chapter 1. The slight asymmetry in ΔP_{IDT} with respect to the external magnetic field orientation can be explained by the shear wave component of the SAW. In contrast, during the EMW pulse, a much smaller magnetic field-dependence is observed.

We now turn to the simultaneously recorded dc voltage $V_{\mathrm{DC}}(t)$ in the Co/Pt bilayer (cf. Fig. 2.4). Since the bilayer is positioned at a distance $d_{\mathrm{MSP}} = 1.3\,\mathrm{mm}$ from the input IDT, the SAW pulse is expected to reach the bilayer 0.1 µs before it is detected at the output IDT. This yields a maximum SAW amplitude at the bilayer at $t_{\mathrm{MSP}} = 0.6\,\mu\mathrm{s}$, while the EMW is again expected at $t \approx 0$. We hence expect EMW-driven effects to appear simultaneously with the microwave pulse, while SAW-driven effects should be prominent at t_{MSP}. In the experimental data, we observe $V_{\mathrm{DC}}(t)$ shown in Fig. 2.5c for $\mu_0 H_{\mathrm{ref}} = 30\,\mathrm{mT}$. For this value of the external magnetic field, V_{DC} is finite only during the EMW pulse. In particular, no signal is observed at t_{MSP}. This is not surprising, since no acoustic FMR is excited for these parameters. Hence, no resonant spin current generation takes place for this external magnetic field configuration. We note that the vanishing V_{DC} signal at t_{MSP} indicates that the presence of an elastic excitation alone is *not* sufficient to generate a spin-current in our bilayer within the resolution of our experiment. This is in contrast to the recent observation of a non-resonant elastically driven spin current in yttrium iron garnet crystals by Uchida *et al.* [90]. In order to observe a resonant elastically driven spin current, the FMR condition needs to be fulfilled. This is the case at $\mu_0 H_{\mathrm{res}} = \pm 4\,\mathrm{mT}$. In Fig. 2.5d we plot $\Delta V_{\mathrm{DC}} = V_{\mathrm{DC}}(\mu_0 H) - V_{\mathrm{DC}}(\mu_0 H_{\mathrm{ref}})$ for $\mu_0 H = \pm 4\,\mathrm{mT}$ (dashed and dotted line, respectively). Here, a clear feature is observed at t_{MSP}. The sign reversal of $\Delta V_{\mathrm{DC}}(t_{\mathrm{MSP}})$ with respect to $\boldsymbol{H}$ direction inversion thereby is a necessary condition and one of the typical signatures for the detection of a spin current via the inverse spin Hall effect [87], since $\boldsymbol{E}_{\mathrm{ISH}} \propto \boldsymbol{M} \times \boldsymbol{J}_{\mathrm{s}}$.

In contrast, the EMW causes a field-symmetric contribution to ΔV_{DC} of larger magnitude. The absence of a sign reversal in this case allows to rule out spin-current generation due to conventional EMW-driven spin pumping. We rather attribute ΔV_{DC} under EMW-excitation to microwave rectification processes. Note that the EMW causes a contribution to ΔV_{DC} already at $\mu_0 H_{\mathrm{ref}} = 30\,\mathrm{mT}$ as shown in Fig. 2.5c. Hence, the microwave rectification observed here takes place even in non-resonant conditions in accordance to the findings in Ref. [110]. However, in our case, the

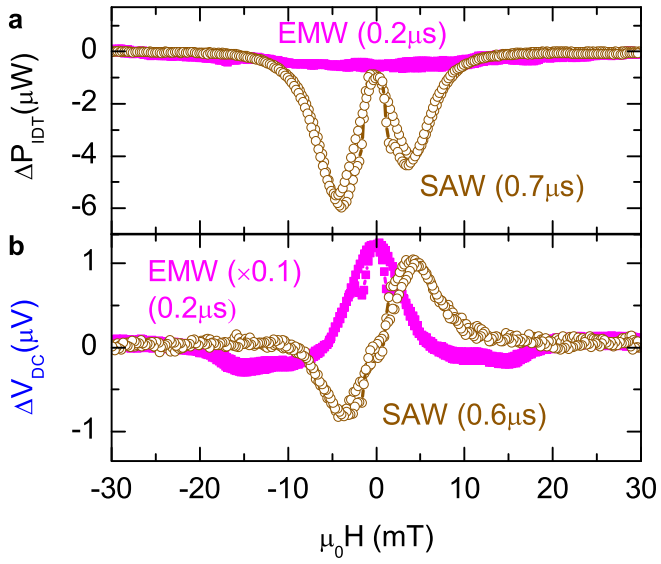

Figure 2.6: **a** ΔP_{IDT} for the detection of the SAW (open symbols) and the EMW (solid symbols) pulse at the output IDT as a function of the external magnetic field magnitude, for $\boldsymbol{H}$ applied at $\alpha = 10°$. **b** ΔV_{DC} for the detection of the SAW (open symbols) and the EMW (solid symbols) pulse at the bilayer. The characteristic fingerprint for acoustic spin pumping is the antisymmetric behavior of ΔV_{DC} with respect to $\boldsymbol{H}$ orientation.

off-resonant EMW contribution to V_{DC} is dominant, as we observe $V_{\mathrm{DC}} \approx 8\,\mathrm{mV}$ at H_{ref} (cf. Fig. 2.5c) while the magnetic field dependent contribution of the EMW to ΔV_{DC} is in the order of $3\,\mu\mathrm{V}$ (cf. Fig. 2.5d). The comparatively large background in V_{DC} observed in the bilayer even far from FMR may be due to piezoelectric EMW rectification [111]. However, since our focus here is on spin pumping, we will not discuss EMW rectification in more detail.

To establish a more complete picture of the contributions to ΔP_{IDT} and ΔV_{DC} due to the SAW and EMW, we now investigate their evolution as a function of H. We hereby take advantage of the separation of the SAW and EMW in the time domain and attribute $\Delta P_{\mathrm{IDT}}(0.2\,\mu\mathrm{s})$ and $\Delta V_{\mathrm{DC}}(0.2\,\mu\mathrm{s})$ to the interaction of the bilayer with the EMW and $\Delta P_{\mathrm{IDT}}(0.7\,\mu\mathrm{s})$ and $\Delta V_{\mathrm{DC}}(0.6\,\mu\mathrm{s})$ to the interaction of SAW and bilayer. We first turn to the EMW and SAW transmission measured at the output IDT. Figure 2.6a shows $\Delta P_{\mathrm{IDT}}(\mu_0 H)$ for both elastic and electromagnetic interaction. We find a very weak magnetic field dependence of the transmission of the EMW (solid symbols) which shows no indication for FMR driven by the EMW. We however observe a distinct

resonant absorption of the SAW (open symbols) which we attribute to acoustically driven FMR as explained in the previous chapter. Note that the slight asymmetry of ΔP_{IDT} with respect to the sign of H can be attributed to the shear component of the SAW. Turning to ΔV_{DC} shown in Fig. 2.6b, we in contrast observe a sizeable magnetic field dependence of the EMW transmission at $t = 0.2\,\mu\mathrm{s}$ (solid symbols) attributed to microwave rectification effects [109]. The fact that $\Delta V_{\mathrm{DC}}(t = 0.2\,\mu\mathrm{s})$ clearly shows the magnetic switching of the Co/Pt layer (dips in up and downsweep at $\mu_0 H = \pm 2\,\mathrm{mT}$) unambiguously shows that this magnetic field dependent contribution is caused by rectification in the Co/Pt bilayer. The signal shape however is distinctly different from that expected for the spin pumping effect, in particular no reversal of the sign of ΔV_{DC} with reversal of $\boldsymbol{H}$ direction is observed. Here, a detailed investigation of the rather complex evolution of $\Delta V_{\mathrm{DC}}(t = 0.2\,\mu\mathrm{s})$ as a function of H is not performed, as our studies are focussed on the phonon-driven effects. For a detailed investigation of microwave rectification processes we refer to, e.g., Refs. [112, 113].

We now turn to the phonon-driven contribution to ΔV_{DC}. At $t_{\mathrm{MSP}} = 0.6\,\mu\mathrm{s}$ (open symbols) only the SAW pulse is present at the bilayer location while the EMW pulse has passed it already. Here, ΔV_{DC} shows a magnetic field dependence characteristic for spin pumping, in particular featuring a sign reversal with reversal of $\boldsymbol{H}$ direction and extrema at the FMR H field as can be seen in comparison to the resonance field shown in Fig. 2.6a. Note that the maximum magnitude of ΔV_{DC} is approximately one order of magnitude larger for the EMW rectification than for the SAW spin pumping. Hence a separation of rectification and spin pumping voltages is crucial for a correct interpretation of our experimental results.

While separation of EMW and SAW driven effects can be performed in our time-resolved experiments, we still need to consider that the SAW bears an electric field itself due to the piezoelectricity of $LiNbO_3$. We now briefly discuss whether this SAW-induced electric field $\boldsymbol{E}_{\mathrm{SAW}}$ may contribute to $\Delta V_{\mathrm{DC}}(\mathrm{SAW})$ due to rectification. It is well known that the in-plane component of $\boldsymbol{E}_{\mathrm{SAW}}$ is oriented parallel to the SAW propagation direction $\boldsymbol{k}_{\mathrm{SAW}} \parallel \boldsymbol{x}$ [44]. We can extract the peak electric power of the SAW pulse from Fig. 2.5(a) to $P_{\mathrm{E}} = 0.4\,\mathrm{mW}$. With the bilayer resistivity $\rho = 550\,\mathrm{n\Omega m}$ determined from a two-point resistance measurement, we calculate the rf current density $i_{\mathrm{rf}} = 6 \times 10^9\,\mathrm{A/m^2}$ along $\boldsymbol{x}$ in the bilayer. For an estimate of the upper limit for V_{DC} by spin rectification of i_{rf}, we use this current density and assume an extremely high rectification efficiency of $C_{\mathrm{rect}} = 1.9 \times 10^{-26}\,\mathrm{Vm^4/A^2}$ as reported

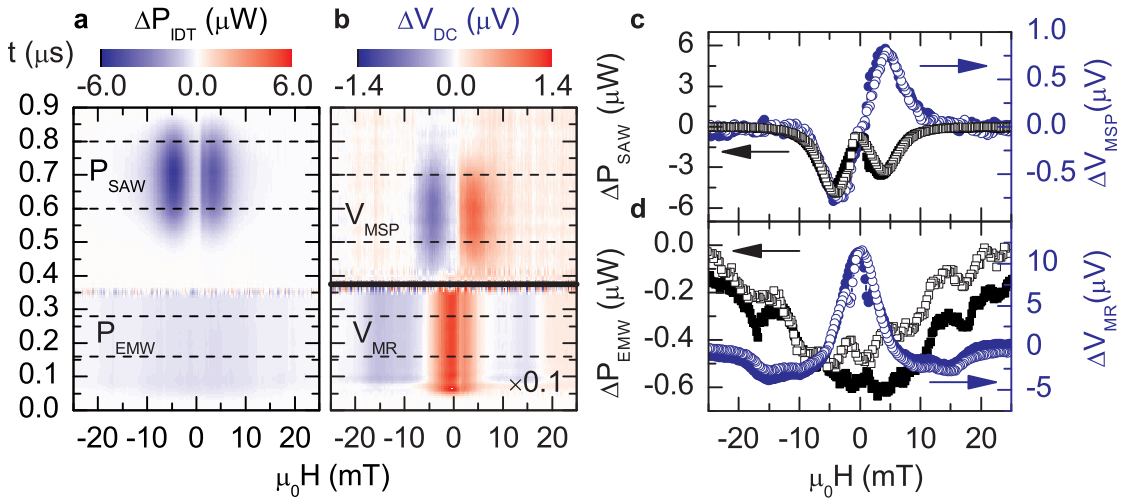

Figure 2.7: **a** ΔP_{IDT} as a function of t and $\mu_0 H$ for $\boldsymbol{H}$ applied at $\alpha = 10°$. **b** $\Delta V_{\mathrm{DC}}(t, \mu_0 H)$ shows EMW rectification (lower part, scaled by 0.1) while the SAW acoustically pumps a spin current which is detected via the inverse spin Hall effect (upper part). **c** We average ΔP_{IDT} and ΔV_{DC} data for the timespan indicated by the dashed lines in **a** and **b**, respectively. These data correspond to all elastic excitation of FMR (ΔP_{SAW}, left scale) and a spin current (ΔV_{MSP}, right scale). **d** Same as **c**, but for electromagnetic crosstalk ΔP_{EMW} and microwave rectification ΔV_{MR}.

by Yamaguchi *et al.* [112] for $Ni_{81}Fe_{19}$ (Py). It follows $V_{\mathrm{DC}} = C_{\mathrm{rect}} \cdot i_{\mathrm{rf}}^2 < 700\,\mathrm{nV}$ along $\boldsymbol{x}$. Now, since we measure V_{DC} along $\boldsymbol{y}$, only a fraction of the order of the anisotropic magnetoresistance will appear in this direction due to the planar Hall effect. We assume an anisotropic magnetoresistance of Co in the order of 1% [114] and thus find that $V_{\mathrm{DC}} < 7\,\mathrm{nV}$. Furthermore, in FM/N bilayers, the rectification efficiency is greatly reduced [113] such that $V_{\mathrm{DC}} \ll 7\,\mathrm{nV}$. Taken together, we can exclude SAW E-field rectification as the origin of V_{DC} observed in the presence of the SAW. Consequently, we attribute $\Delta V_{\mathrm{DC}}(\mathrm{SAW})$ solely to phonon-driven spin pumping. This is furthermore supported by the fact that - within our experimental sensitivity - $\Delta V_{\mathrm{DC}}(\mathrm{SAW})$ vanishes out of resonance, in accordance to the expectations from photon-FMR-driven spin pumping.

To show the separation of EMW and SAW driven effects in more detail, we plot ΔP_{IDT} and ΔV_{DC} as a function of t and $\mu_0 H$ in Fig. 2.7a and b, respectively (only magnetic field upsweep shown). In the ΔP_{IDT} data depicted in Fig. 2.7a, the EMW contribution P_{EMW} ($t < 0.375\,\mu\mathrm{s}$) exhibits only a very weak dependence on H. The

visible artifacts in ΔP_{IDT} at $t \approx 0.35\,\mu\mathrm{s}$ are caused by trigger jitter of the oscilloscope. At $0.5\,\mu\mathrm{s} < t < 0.85\,\mu\mathrm{s}$, two field symmetric Gaussian pulses are observed at $\mu_0 H_{\mathrm{res}} = \pm 4\,\mathrm{mT}$. As explained above, these pulses are attributed to the detection of acoustically driven FMR.

The DC voltage V_{DC} measured along the $\boldsymbol{y}$ axis of the Co/Pt bilayer is shown in Fig. 2.7b. Here, EMW rectification is observed for $t < 0.375\,\mu\mathrm{s}$ yielding a field-symmetric contribution to ΔV_{DC}. In the presence of the SAW pulse at $0.4\,\mu\mathrm{s} < t < 0.75\,\mu\mathrm{s}$, ΔV_{DC} is finite only for a narrow range around the FMR magnetic field $\mu_0 H_{\mathrm{res}} = \pm 4\,\mathrm{mT}$. As mentioned above, the observed change of sign of ΔV_{DC} with $\boldsymbol{H}$ orientation reversal is mandatory for spin-pumping in combination with the inverse spin Hall effect. One can furthermore observe that the phonon-driven features in ΔP_{IDT} are retarded by about $0.1\,\mu\mathrm{s}$ with respect to ΔV_{DC} (indicated by the dashed lines), in accordance to the propagation of the SAW along the delay line. For the investigation of phonon-driven spin pumping with good signal to noise ratio, we average ΔP_{IDT} and ΔV_{DC} for the time range indicated by the dashed lines. This yields the phonon-driven ΔP_{SAW} and ΔV_{MSP}, respectively. ΔP_{SAW} and ΔV_{MSP} are plotted in Fig. 2.7c as a function of H (solid symbols: H upsweep, open symbols: H downsweep). While a field symmetric absorption of rf power is observed for ΔP_{SAW} as expected for acoustically driven FMR [37], ΔV_{MSP} shows the antisymmetric behavior with respect to $\boldsymbol{H}$ orientation reversal characteristic of spin pumping. Furthermore, the resonance field and linewidth of ΔP_{SAW} and ΔV_{MSP} coincide. Outside of acoustically driven FMR (i.e. $\mu_0|H| > 10\,\mathrm{mT}$), the SAW and thus phonons are still present in the ferromagnetic thin film. However, within the resolution of our experiment, $\Delta V_{\mathrm{MSP}} = 0$ in this off-resonant condition. Thus, a non-resonant phonon-driven spin current is not observed in our experiments.

For the photon-driven effects displayed in Fig. 2.7d, ΔP_{EMW} corresponds to the field-dependence of the detected EMW power at the output IDT during the rf pulse. Only a very weak field dependence is observed, with no indication for the detection of EMW-driven FMR in the Co/Pt bilayer. The microwave rectification voltage ΔV_{MR} shown in Fig. 2.7d however shows a distinct dependence on the external magnetic field. While a detailed investigation of V_{MR} is beyond the scope of this work, we note again that V_{MR} is field-symmetric and thus bears a distinctly different symmetry than the spin-pumping voltage V_{MSP}.

We now compare the observed spin-pumping voltage V_{MSP} to phenomenological

expectations. Using the scaling law derived in Ref. [87], we can calculate the resonant $\boldsymbol{M}$ precession cone angle Θ_{res} as:

$$\sin^2\Theta_{\mathrm{res}} = \frac{\Delta V_{\mathrm{MSP}}}{e\nu PRwCg_{\uparrow\downarrow}} \tag{2.3}$$

with the elementary charge e, the ellipticity $P = 0.11$ calculated according to Ref. [75], the resistance $R = 37\,\Omega$ [2] and width $w = 375\,\mu\mathrm{m}$ of the Co/Pt bilayer, the constant $C = 4.37 \times 10^{-11}\,\mathrm{m}$ [87] and the spin mixing conductance of Co/Pt $g_{\uparrow\downarrow} = 6 \times 10^{19}\,/\mathrm{m}^2$ [87]. With $\nu = 1.548\,\mathrm{GHz}$ and $\Delta V_{\mathrm{MSP}} = 0.8\,\mu\mathrm{V}$ from Fig. 2.7c, Eq. (2.3) yields $\Theta_{\mathrm{res}} = 1.6°$, which is similar to Θ_{res} observed in photon-driven FMR experiments with comparable[3] rf powers [87]. Out of resonance $\Delta V_{\mathrm{MSP}} < 0.1\,\mu\mathrm{V}$ and hence the $\boldsymbol{M}$ precession cone angle is $\theta < 0.6°$ assuming identical P. We can now apply magnetoelastic theory to calculate the strain needed to magnetoelastically drive $\boldsymbol{M}$ precession with such a precession cone angle. Using $\Theta_{\mathrm{res}} = 1.6°$, the strain caused by the SAW corresponds to a rf virtual driving field of $\mu_0 H_{\mathrm{magel}} = \frac{1}{2}\mu_0 \Delta H \Theta_{\mathrm{res}} = 73\,\mu\mathrm{T}$ with $\mu_0\Delta H = 5.25\,\mathrm{mT}$ extracted from Fig. 2.7c as the FWHM of ΔV_{MSP} at resonance.

For acoustically driven FMR, $\mu_0 H_{\mathrm{magel}} = 2B_1\varepsilon\cos\phi_0\sin\phi_0$ (cf. Eq. (1.9)), where $B_1 = 15.4\,\mathrm{T}$ [115] is the magnetoelastic coupling constant divided by the saturation magnetization $M_{\mathrm{s}} = 1.17 \times 10^6\,\mathrm{A/m}$ [116] and $\phi_0 = 30°$ is the equilibrium orientation of $\boldsymbol{M}$ for $\boldsymbol{H}$ applied at $\alpha = 10°$ calculated by a free energy minimization as explained in Chapter 1.

Equation (1.9) yields a strain $\varepsilon \approx 5.7 \times 10^{-6}$ in the ferromagnet due to the SAW pulse. At a SAW wavelength of $\lambda = 2.2\,\mu\mathrm{m}$ this yields a SAW amplitude of $u_x = 0.01\,\mathrm{nm}$. For comparison, we now derive the SAW amplitude directly from the measured SAW power by vector network analysis as detailed in Section 1.5.1. We find the total power of the SAW $P_{\mathrm{SAW}} = 17.5\,\mathrm{mW}$ and the acoustic power $P_{\mathrm{acoustic}} = k^2 P_{\mathrm{SAW}} = 0.9\,\mathrm{mW}$ with $k^2 = 5\%$ [44] being the electromechanical coupling coefficient of $LiNbO_3$. According to Eq. (1.20) the amplitude of the pure strain component is given by $u_x = \frac{2}{3}\left[P_{\mathrm{acoustic}}/\left(2\pi\nu_{\mathrm{SAW}} W M\right)\right]^{0.5} = 0.02\,\mathrm{nm}$ with $M = 1.4 \times 10^{11}\,\mathrm{J/m^3}$ [54] and the IDT width $W = 500\,\mu\mathrm{m}$ assuming that $u_x = \frac{2}{3}u_z$. Hence, the SAW amplitude calculated from the measured power at the IDT is large

[2] R was determined by a 2 point measurement and takes into account that only a fraction of the Co/Pt is perturbed by the SAW

[3] We use 1 W rf pulses to drive the IDTs, while in the photon-driven spin pumping experiments with Co/Pt 200 mW of rf power was applied to a microwave cavity.

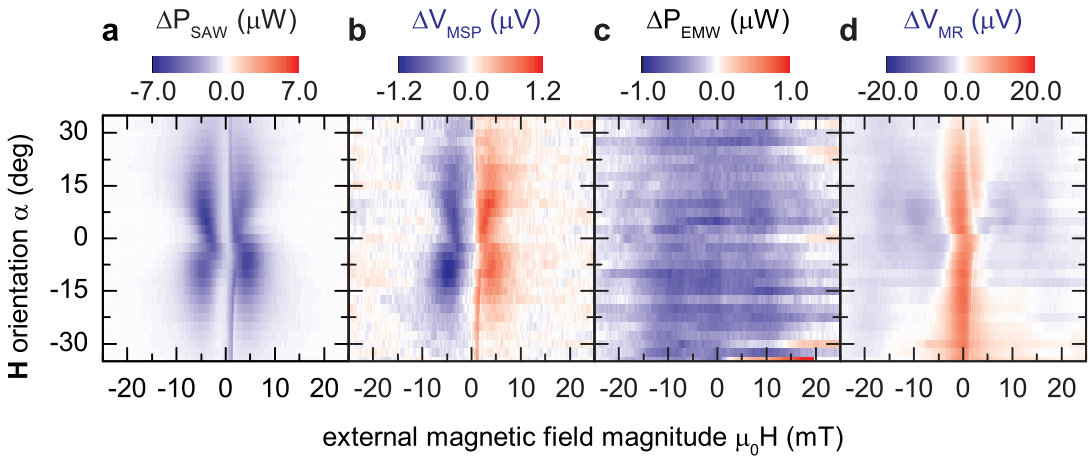

Figure 2.8: **a** ΔP_{SAW} and **b** ΔV_{MSP} as a function of $\boldsymbol{H}$ orientation and magnitude for magnetic field upsweep. The observed angular dependency is characteristic for acoustically driven FMR. The features around 2 mT are due to $\boldsymbol{M}$ reversal. **c** ΔP_{EMW} shows no sign of FMR due to the EMW. **d** Microwave rectification ΔV_{MR} in the bilayer.

enough to account for V_{MSP} alone, even after considering potential decay of SAW amplitude along the delay line and the fact that V_{MSP} is an averaged value during the Gaussian SAW pulse. This corroborates the notion that we indeed observe acoustically driven spin pumping.

As a final test for the phononic nature of the spin-pumping effect described here, we performed a series of experiments as a function of the external magnetic field in-plane orientation α. As detailed in the previous chapter, the characteristic fingerprint of acoustically driven FMR is exactly this dependence on the orientation α. Hence, we expect to find an identical symmetry in our acoustically driven spin-pumping experiments, while different symmetries are expected for EMW-driven effects. We thus studied ΔP_{IDT} and ΔV_{DC} as a function of α. Time domain analysis and subsequent averaging as shown in Fig. 2.7 now yield the phonon-driven contributions ΔP_{SAW} and ΔV_{MSP} and the photon-driven contributions ΔP_{EMW} and ΔV_{MR}. These are shown as a function of α and H in Fig. 2.8. Clearly, the fourfold symmetry that was observed for phonon-driven FMR in Chapter 1 is present also in Fig. 2.8a. Note that in Chapter 1, we studied Ni while here we address Co, such that differences in resonance magnetic fields and lineshape are attributed to different material parameters. In the

Co/Pt bilayer, acoustic spin pumping shows identical symmetry as the acoustically driven FMR as shown in Fig. 2.8b. Note the sign change in ΔV_{MSP} with reversal of $\boldsymbol{H}$ orientation and the lack of off-resonantly excited spin currents ($\Delta V_{\mathrm{MSP}} = 0$ whenever $\Delta P_{\mathrm{SAW}} = 0$). We now turn to the photon-driven contributions ΔP_{EMW} and ΔV_{MR} to ΔP_{IDT} and ΔV_{DC}, respectively. Here, no systematic evolution of ΔP_{EMW} with $\boldsymbol{H}$ is found in Fig. 2.8c. Furthermore, ΔV_{MR} in Fig. 2.8d shows a field-symmetric H dependence for any α, clearly discerning it from ΔV_{MSP}. Note that, in particular, the resonance magnetic fields are not clearly pronounced in ΔV_{MR}. This can be seen by considering the magnetic anisotropy of the Co which shows a hard axis along $\alpha = 0°$ as clearly evident from the SAW driven FMR which shows maximum intensity for $|\alpha| < 45°$ (cf. Chapter 1). Now, for photon-driven FMR the resonance magnetic field is expected to shift to higher values of $|H|$ at the hard axis and thus at $\alpha = 0°$. However, from the data presented in Fig. 2.8d, such a behavior can not be clearly derived. Considering that a sizable V_{MR} is already observed at $\mu_0 H = 30\,\mathrm{mT}$ (cf. Fig. 2.5c) we assume that off-FMR processes [110] are the dominant contribution to V_{MR}. Taken together, the photon- and phonon-driven contributions to V_{DC} show distinctly different symmetries after separation in the time domain and evidence for spin-pumping can be clearly observed in the exclusive presence of a coherent elastic wave.

2.4 Conclusions and outlook

In conclusion, we have shown that a spin current can be generated by microwave phonons via rf magnetoelastic interaction in a Co/Pt thin film bilayer. By recording both, the generated inverse spin Hall voltage proportional to the spin current, and the SAW transmission as a function of time for various configurations of the externally applied magnetic field, we are able to discern between effects caused by photonic and phononic excitations. We find that a spin current is generated in the exclusive presence of a resonant acoustic excitation of the Co thin film. Our findings thus establish a resonant analogue to the spin Seebeck effect by exploiting phonon-driven spin current generation. We did not observe any indication for off-resonant elastic spin pumping [90, 91]. This is in full accordance to the expectations from photon-FMR-driven spin pumping experiments [75, 87].

As the concept introduced here does not rely on thermal gradients but rather on an elastic deformation for spin current generation, it provides a viable path for the

implementation in micromechanical devices. This should enable the augmentation of, e.g., microelectromechanical systems (MEMS) with the possibility to elastically generate spin currents for future spintronic data processing applications.

From a fundamental physics point of view, our results are an important step towards the study of the interconversion of phononic and spin degrees of freedom. In future experiments, it will be necessary to clearly separate the physical principles that are involved in the off-resonant acoustic spin current generation reported by Uchida *et al.* [90, 91], and the resonant acoustic spin current generation discussed here. So far, the interaction mechanism for the off-resonant acoustic spin pumping lacks detailed exploration in particular on theoretical grounds. In this regard, using SAWs to provide the phonons is a very appealing approach due to the wide frequency range (some MHz to several GHz) in which SAWs can be excited. This, in principle, allows experiments with a broad range of excitation frequencies using harmonic excitation and/or several IDTs. In combination with the application of an external magnetic field, both, off-resonant and resonant acoustic excitation can be investigated in one and the same sample. The resonance condition is hereby determined via the external magnetic field configuration.

Furthermore, our experimental approach allows for a time-resolved investigation of the generated voltages. As evident from the results discussed in this chapter, this is mandatory for a clear separation of acoustically driven inverse spin Hall effect voltages from spurious rectification voltages. Future time-resolved SAW driven studies in further materials, e.g. the ferromagnetic insulator YIG, will be important to reveal details of the spin-current-generating interaction of phonons and magnons. Thereby special attention should be paid to the role of magnetoelasticity. While we identified magnetoelastic interaction to be the driving force behind the resonant acoustic spin current generation discussed here, magnetoelasticity is roughly two orders of magnitude lower in YIG than in Co ($B_1^{\mathrm{Co}} = 18\,\mathrm{MJ/m^3}$ [115] and $B_1^{\mathrm{YIG}} = 0.35\,\mathrm{MJ/m^3}$ [117]). Nevertheless, it surprisingly appears to be possible to generate a spin-current via a magnon-phonon interaction in YIG [90, 91]. This finding needs to be reviewed and compared to acoustic excitation of FMR in a time-resolved study. Establishing a scaling law similar to that derived by Czeschka *et al.* [87] for both, resonant and non-resonant acoustic excitation could be a very appealing way to identify and separate acoustic spin pumping mechanisms. This could be done, e.g., by studying the generated spin current as a function of the precession cone angle, the magnetoelastic

coupling, or spin Seebeck coefficient.

Finally, the present theoretical understanding of the spin pumping effect suggests that the emitted spin current contributes to a damping of the magnetization similar to the Gilbert magnetization damping [84]. Thus the effect of spin pumping on the magnetization dynamics can be phenomenologically described by an additional term in the Landau-Lifshitz-Gilbert equation (cf.Eq. (1.3)) which has the same symmetry as the damping term. It thus follows that the emitted spin current is proportional to $\boldsymbol{m} \times \partial_t \boldsymbol{m}$. With the ansatz $\boldsymbol{m} = \{m_1 \cos \omega t, m_2 \sin \omega t, m_0\}$, one finds $\boldsymbol{m} \times \partial_t \boldsymbol{m} = \{m_0 m_2 \cos \omega t, -m_0 m_1 \sin \omega t, m_1 m_2\}$. This suggests that in addition to the dc spin current proportional to $m_1 m_2$ which was investigated here, radio frequency spin currents are generated in ferromagnetic resonance orthogonal to the dc component. A detailed theoretical and experimental investigation of these rf spin currents is a fundamental step towards separating the physical principles behind the spin Seebeck effect and spin pumping.

Chapter 3

Spin and charge currents in magnetothermal landscapes

In conductive materials, Ohm's law relates the electric field to electrical charge motion. In a similar fashion, a temperature gradient ∇T can drive charge redistribution which results in the Seebeck [118] and Nernst [119] effects. In other words, ∇T results in a heat current which, in metals, is carried mainly by charge carriers resulting in said thermoelectric effects. Since charge carriers also transport spin, thermo-spin-effects can appear in spin polarized systems or in the presence of strong spin-orbit coupling. In magnetic media, the orientation of the magnetization with respect to ∇T plays an essential role for the sign and magnitude of the magneto-thermoelectric field. Even more intriguing, it was recently discovered that not only spin polarized charge currents, but even pure spin currents can be driven by thermal gradients in magnetic media. The corresponding phenomenon is called spin Seebeck effect [77, 89]. In the literature, both charge and spin based magnetothermal effects have been investigated using spatially homogeneous temperature gradients, such that only the integral properties were probed. However, the properties of magnetic materials often are spatially inhomogeneous, e.g., due to magnetic domain formation. Thus, a spatially resolved study of magnetothermal effects appears as an important next step to establish a microscopic picture of the magnon-phonon interactions driving charge and spin currents.

In this chapter, we present a quantitative, spatially resolved experimental study of the spin Seebeck and anomalous Nernst effect arising in magnetic media exposed to magnetothermal landscapes. A scannable laser beam is used to generate local thermal gradients in metallic (Co_2FeAl) or insulating ($Y_3Fe_5O_{12}$) ferromagnetic thin films. We

study the resulting local charge and spin currents that arise due to the anomalous Nernst effect (ANE) and the spin Seebeck effect (SSE), respectively. In the local ANE experiments, we detect the voltage in the Co_2FeAl thin film plane as a function of the laser spot position and external magnetic field magnitude and orientation. The local spin current generated by the SSE effect is detected in a similar fashion by exploiting the inverse spin Hall effect [92, 93] in a Pt layer deposited on top of the $Y_3Fe_5O_{12}$. Our findings demonstrate that spatially confined thermal gradients allow for the generation of local, bipolar and magnetically controllable electric fields or spin currents that can be used to, e.g., electrically image the magnetic microstructure in ferromagnetic metals and insulators. The main results presented in this chapter have been published in Ref. [120] and discussed in Ref. [121].

3.1 Caloric transport effects

Caloric transport effects arise due to the transport of heat in solid media in close analogy to electric transport. As discussed, e.g., in the book by Harman and Honig [122] as well as in Ref. [123] one finds the following relations for combined electric and caloric transport in the presence of a magnetic induction $\boldsymbol{B} = \mu_0 (\boldsymbol{H} + \boldsymbol{M})$:

$$\boldsymbol{E} = \underbrace{\rho \boldsymbol{J}_\mathrm{q}}_{\text{Electrical conductivity}} + \underbrace{R_\mathrm{H} (\boldsymbol{B} \times \boldsymbol{J}_\mathrm{q})}_{\text{Hall effect}} + \underbrace{S \nabla T}_{\text{Thermopower}} + \underbrace{N (\boldsymbol{B} \times \nabla T)}_{\text{Nernst effect}} \tag{3.1}$$

$$\boldsymbol{J}_\mathrm{h} = \underbrace{\Pi \boldsymbol{J}_\mathrm{q}}_{\text{Peltier effect}} + \underbrace{P (\boldsymbol{B} \times \boldsymbol{J}_\mathrm{q})}_{\text{Ettingshausen effect}} - \underbrace{\kappa \nabla T}_{\text{Thermal conductivity}} + \underbrace{L (\boldsymbol{B} \times \nabla T)}_{\text{Righi–Leduc effect}} . \tag{3.2}$$

Here, $\boldsymbol{E}$ is the electric field, ∇T is the temperature gradient, $\boldsymbol{J}_\mathrm{q}$ is the charge current and $\boldsymbol{J}_\mathrm{h}$ is the heat current. The resistivity ρ, as well as all other constants in Eqs. (3.1) and (3.2) are assumed to be scalar for simplicity, although they are tensorial quantities in general. We now briefly discuss the eight magneto-thermoelectric effects governed by Eqs. (3.1) and (3.2).

Electrical conductivity

The first term in Eq. (3.1) is Ohm's law with the resistivity tensor ρ. Note that ρ depends on $\boldsymbol{B}$, leading to, e.g., anisotropic magnetoresistance in ferromagnetic media.

Hall effect

The second term in Eq. (3.1) refers to the Hall effect which arises due to the Lorentz force. The Hall effect describes the occurrence of an electric field perpendicular to both, charge current and magnetic induction. In the single band model, the Hall constant $R_{\mathrm{H}} = -1/ne$ is a function of the charge carrier density n.

Thermopower

The third term in Eq. (3.1) describes the thermopower. The thermopower coefficient S is usually determined using the Seebeck effect, in which two metals - one with unknown thermopower S_1 and one with known thermopower S_2 - are arranged in a thermocouple such that they are electrically connected at one end as schematically depicted in Fig. 3.1a. With the ends of the two metals being exposed to the identical temperature difference ΔT, a voltage $V = (S_1 - S_2)\,\Delta T$ appears between the open ends of the metals. Thermocouples consisting of two materials with known thermopowers are used as thermometers.

Nernst effect

The last term in Eq. (3.1) bears a Hall-like symmetry but is observed in the presence of a thermal gradient instead of a charge current. It describes the Nernst effect. Due to its symmetry with respect to ∇T it results in a finite electric field within the plane of a conductive thin film with in plane magnetization which is exposed to a thermal gradient along the film normal. The Nernst effect is central to the results discussed in the following sections.

Peltier effect

The first term in Eq. (3.2) is the Peltier effect where a charge current induces a heat current. Due to the Onsager reciprocity relations [124, 125], the peltier coefficient Π is linked to the thermopower by $\Pi = S \cdot T$.

Ettingshausen effect

The second term in Eq. (3.2) describes the generation of a heat current perpendicular to both, $\boldsymbol{J}_{\mathrm{q}}$ and $\boldsymbol{B}$. The Ettingshausen coefficient P/κ is linked to the Nernst coefficient by $P = N \cdot T$ due to the Onsager relations [124, 125].

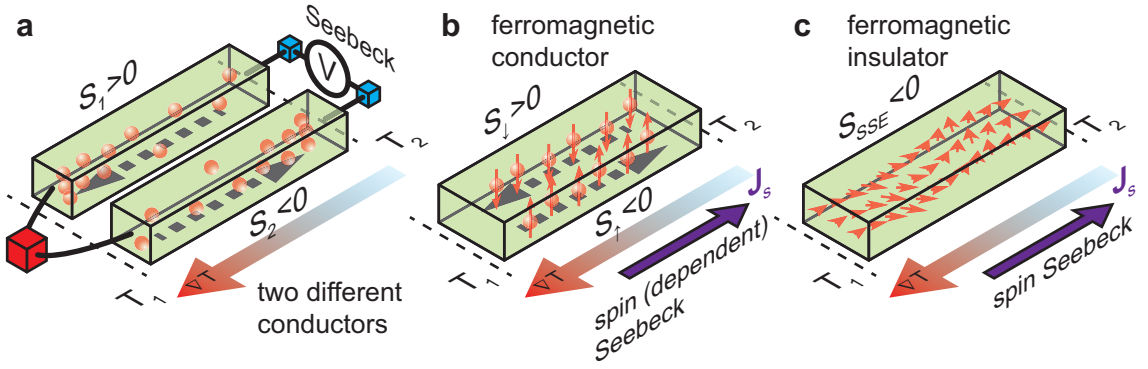

Figure 3.1: **a** The conventional Seebeck effect is proportional to the difference of the thermpowers of two conductors. **b** A conductive ferromagnet is a single-material spin-thermocouple due to the spin (dependent) Seebeck effect where spin up and spin down charge carriers have different Seebeck coefficients. **c** The spin Seebeck effect in a ferromagnetic insulator is due to the transport of heat and angular momentum by magnons and takes place in the absence of mobile charge carriers.

Thermal conductivity

The third term in Eq. (3.2) describes the heat current due to a temperature gradient. The negative sign accounts for the fact that heat (or entropy) is always transported from hot to cold, so that the thermal conductivity κ is positive for all materials. In metals, electrons carry both, charge and heat. One thus finds $\kappa = LT/\rho$ with the universal Lorenz number $L = 2.45 \times 10^{-8}\,\mathrm{W\Omega/K^2}$ (Wiedemann-Franz-law).

Righi-Leduc effect

Finally, the last term in Eq. (3.2) is the Righi-Leduc-Effect with the Righi-Leduc coefficient L/κ. It is the thermal analogue to the Hall effect and arises due to the Lorentz force on electrons that carry heat due to the thermal gradient ∇T.

3.1.1 Spin Seebeck effect

The magneto-thermoelectric effects introduced above can be observed in metals. In these materials, electrons dominate both, charge and heat transport. However, electrons carry an additional degree of freedom - their spin. This leads to further intriguing effects such as the spin Hall effect (cf. Section 2.1.2). Recently, a novel thermomagnetic effect that describes spin transport by a thermal gradient was discovered [89]. In

analogy to the conventional Seebeck effect (cf. Fig. 3.1a) that describes charge transport by a thermal gradient, it thus was called spin Seebeck effect [89]. As depicted in Fig. 3.1b, the spin Seebeck effect discovered by Uchida *et. al* [89] in a metallic ferromagnet can be understood in the context of a single-material spin-thermocouple where the spin up and spin down electrons have different Seebeck coefficients. This results in a net flow of angular momentum along the temperature gradient and thus the accumulation of spin up and spin down electrons at opposite ends of the sample in open circuit conditions. In materials where the flow of angular momentum occurs in the absence of a net charge current, i.e. assuming an equal number of spin up and spin down charge carriers as depicted in Fig. 3.1b, this spin *dependent* Seebeck effect becomes a pure spin Seebeck effect.

However, the transport of angular momentum does not necessarily require mobile charge carriers. For instance, a spin wave (or magnon) can transport angular momentum in ferromagnets. As magnons can transport heat as well, a spin Seebeck effect can be observed even in ferromagnetic insulators - as first experimentally demonstrated by Uchida *et. al* [77] and sketched in Fig. 3.1c. At the time being, the microscopic picture of the spin Seebeck effect is entirely different in metallic and in insulating ferromagnets. We note that the magnitude of the spin Seebeck effect reported in the metallic ferromagnet permalloy [89] and in the insulating ferromagnet yttrium iron garnet [77] are however very similar with a spin Seebeck coefficient of $S_{\mathrm{SSE,Py}} = 0.25\,\mu\mathrm{V/K}$ in permalloy/Pt and $S_{\mathrm{SSE,YIG}} = 0.1\,\mu\mathrm{V/K}$ in YIG/Pt[1]. Clearly, more experiments and a better theoretical understanding are needed to clarify the role of the magnon-driven spin Seebeck effect in metals.

In the experiments discussed in this Chapter we investigate the spin Seebeck effect in thin films of the ferromagnetic insulator yttrium iron garnet. As shown below, our measurement geometry furthermore allows for the investigation of the anomalous Nernst effect in ferromagnetic conductors. We now discuss the basic idea, the experimental setup and results that constitute spatially resolved magnetothermal charge and spin current generation.

[1]The spin Seebeck coefficients taken from Refs. [77, 89] are determined using the inverse spin Hall effect in Pt and thus depend on its spin Hall angle. The same holds true for S_{SSE} in Eq. (3.4).

3.1.2 Spatially resolved anomalous Nernst and spin Seebeck effects

In conductive media exposed to a thermal gradient ∇T, the presence of a magnetic induction $\boldsymbol{B}$ results in an electric field $\boldsymbol{E} = N\boldsymbol{B} \times \nabla T$ due to the Nernst effect as discussed above. In ferromagnetic conductors, the magnetization $\boldsymbol{M}$ results in a finite magnetic induction $\boldsymbol{B} = \mu_0(\boldsymbol{H} + \boldsymbol{M})$ even at vanishing external magnetic field $\boldsymbol{H}$. In this limit ($M \gg H$), the anomalous Nernst effect (ANE) is the dominant cause of magnetothermal transversal electric fields in ferromagnetic materials. The ANE [119] describes the occurrence of an electric field $\boldsymbol{E}_{\mathrm{ANE}} \propto \boldsymbol{M} \times \nabla T$, perpendicular to both, the temperature gradient ∇T and the magnetization $\boldsymbol{M}$. It has been studied extensively in bulk ferromagnets [126–129] as well as in a variety of ferromagnetic thin film metals [129, 130], oxides [129, 131], spinels [129, 132, 133] and diluted magnetic semiconductors [134].

In analogy to charge-based caloritronic effects [122], the recently discovered spin Seebeck effect (SSE) [89] describes the generation of a spin current $\boldsymbol{J}_{\mathrm{s}}$ parallel to an applied temperature gradient ∇T in ferromagnetic materials. $\boldsymbol{J}_{\mathrm{s}}$ can be detected all electrically by exploiting the inverse spin Hall effect [92, 93] (cf. Section 2.1.2) in a normal metal (N) deposited on top of the ferromagnet (FM). In the longitudinal spin Seebeck configuration [135], ∇T is applied along the FM/N hybrid normal, resulting in an electric field $\boldsymbol{E}_{\mathrm{ISHE}} \propto \boldsymbol{J}_{\mathrm{s}} \times \boldsymbol{\sigma}$. Here, $\boldsymbol{\sigma} \parallel \boldsymbol{M}$ is the spin polarization, such that the symmetry of the SSE is identical to the ANE with respect to $\boldsymbol{M}$ and ∇T. Spin Seebeck measurements have been carried out in ferromagnetic metals [89,136], diluted magnetic semiconductors [137] and magnetic insulators [77].

The interplay of spins and temperature leads to further intriguing effects such as the spin Peltier effect [138, 139], thermal spin torque [140, 141], or thermally driven spin injection [142, 143]. However, in all spin caloritronic experiments mentioned above, homogeneous temperature gradients were applied. In order to establish the interplay between temperature gradients and spin degrees of freedom also on the length scale of the magnetic microstructure, temperature gradients changing on such length scales are mandatory. Here, we therefore use a focussed, scanning laser beam to generate a local temperature gradient perpendicular to a thin film sample plane, and perform a spatially resolved study of the resulting spin caloritronic effects.

In such spatially resolved experiments in conductive ferromagnetic thin films the local anomalous Nernst effect arising due to a temperature gradient along the film

normal $\boldsymbol{z}$ results in an electric field

$$\boldsymbol{E}_{\mathrm{ANE}}(x,y) = -N\mu_0 \boldsymbol{M}(x,y) \times \nabla T(x,y) \ , \tag{3.3}$$

at position (x, y) with the Nernst coefficient N. This local electric field can be detected in an integral voltage measurement[2].

In ferromagnetic insulators, the Nernst effect is suppressed since there are no mobile charge carriers. It was however shown [77] that the spin Seebeck effect persists, as spin currents can flow even in the absence of charge carrier mobility due to angular momentum transport by magnons. In a ferromagnetic insulator/normal metal bilayer, the inverse spin Hall effect in the metallic constituent can be used to detect the spin currents flowing across the interface. Hence, in such samples exposed to a local temperature gradient, the spin Seebeck and inverse spin Hall effect yield a local electric field

$$\boldsymbol{E}_{\mathrm{ISHE}}(x,y) = -S_{\mathrm{SSE}} \boldsymbol{\sigma}(x,y) \times \nabla T(x,y) \ , \tag{3.4}$$

defined analogous to the integral expression given in Ref. [137] with the phenomenological spin Seebeck coefficient S_{SSE} and the spin polarization vector $\boldsymbol{\sigma} = \boldsymbol{M}/M_{\mathrm{s}}$, with the saturation magnetization M_{s}.

Comparing Eq. (3.3) and Eq. (3.4), it is evident that $\boldsymbol{E}_{\mathrm{ANE}}$ and $\boldsymbol{E}_{\mathrm{ISHE}}$ bear identical symmetry. Hence both, $\boldsymbol{E}_{\mathrm{ANE}}(x,y)$ and $\boldsymbol{E}_{\mathrm{ISHE}}(x,y)$ can be detected in an identical fashion, enabling a spatially resolved study of charge and spin currents in a magnetothermal experiment. It is important to note that $\boldsymbol{E}_{\mathrm{ANE}}(x,y)$ and $\boldsymbol{E}_{\mathrm{ISHE}}(x,y)$ are local electric fields, determined by the magnetic properties and temperature gradient at position (x, y). In conductive ferromagnets with $N \neq 0$, a spatially confined $\nabla T(x,y)$ will thus evoke a local $\boldsymbol{E}_{\mathrm{ANE}}(x,y)$. Its magnitude and polarity are controllable in situ by manipulating $\boldsymbol{M}(x,y)$. Vice versa, $\boldsymbol{E}_{\mathrm{ANE}}(x,y)$ can be used to electrically read out the magnetization $\boldsymbol{M}(x,y)$ with full 360° confidence, i.e., to electrically image the magnetic microstructure by scanning $\nabla T(x,y)$ across the sample. Identical considerations apply in magnetic insulator / normal metal bilayers where $\boldsymbol{E}_{\mathrm{ISHE}}(x,y)$ is generated in the presence of a temperature gradient. $\boldsymbol{E}_{\mathrm{ISHE}}(x,y)$ is, however, caused by a local spin current $\boldsymbol{J}_{\mathrm{s}}(x,y)$. Hence the detection of $\boldsymbol{E}_{\mathrm{ISHE}}(x,y)$ not only allows to electrically detect magnetic texture in a ferromagnetic insulator,

[2]The minus signs in Eqs. (3.3) and (3.4) were introduced so that the obtained N and S_{SSE} are in accordance to literature. In particular, the sign of S_{SSE} is still unclear as it seems to depend on measurement geometry [135].

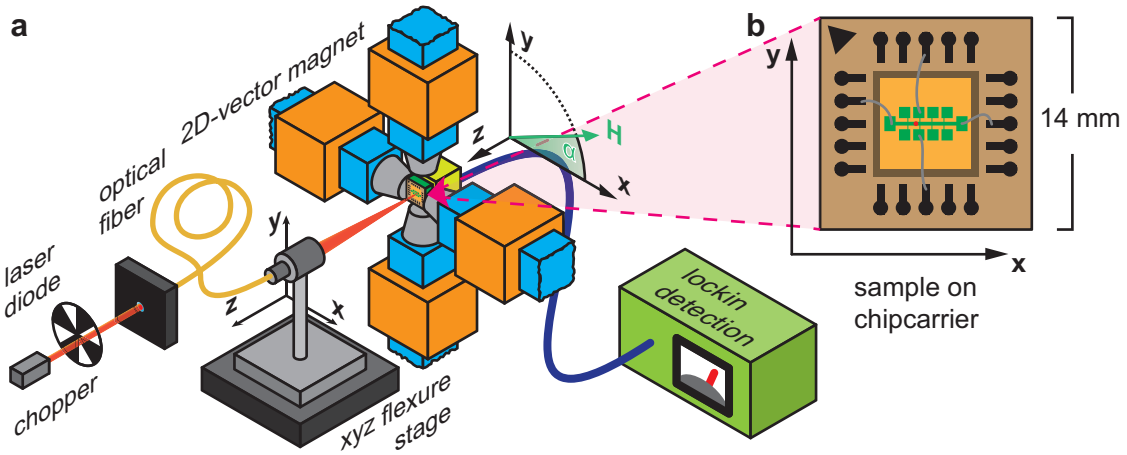

Figure 3.2: **a** Schematic illustration of the experimental setup. A scannable laser beam is focussed on the sample surface to provide the thermal landscape. An external magnetic field can be applied within the sample plane via a 2D-vector magnet. **b** Closeup of sample with Hall bar (Hall bar not to scale) mounted on chip carrier.

but even enables the spatial mapping of spin currents.

3.2 Experimental setup and samples

To record spatial maps of spin and charge currents in magnetothermal landscapes we use the setup schematically depicted in Fig. 3.2a. It was conceived and assembled during this thesis. A laser diode with wavelength $\lambda = 658\,\mathrm{nm}$ and power $P_0 = 40\,\mathrm{mW}$ is coupled into a single mode optical fiber which terminates in a collimator with a $f = 11\,\mathrm{mm}$ lens. The collimator is mounted on a xyz flexure stage (Thorlabs NanoMax) with a traveling range of 4 mm in all three directions. The computer-controlled stage movement is performed by three stepper motors with a repetition accuracy of 500 nm. The external magnetic field $|\mu_0 H| \leq 100\,\mathrm{mT}$ can be applied at any orientation α within the sample plane via a homebuilt 2D vector magnet. The vector magnet features 4 identical coils that can be exposed to a maximum current of 4 A. The coils form two pairs, each of which is connected by an iron core, so that the sample is positioned in a gap of approximately $2 \times 2\,\mathrm{cm}^2$. The magnetic field is measured by two Hall probes that determine the $\boldsymbol{x}$ and $\boldsymbol{y}$ components H_x and H_y of the external magnetic field $\boldsymbol{H}$. H_x and H_y are closed-loop PI controlled

by two Lakeshore DSP 475 Gaussmeters that set the output currents of two Kepco BOP bipolar four quadrant power supplies. A measurement program which enables fully automated vector-magnetic field and stage position control was developed using National Instruments Labview specifically for this setup.

In a typical measurement procedure, the laser beam is focussed and scanned over the surface of the investigated sample, which is patterned into a Hall bar geometry. The sample is mounted on a chipcarrier system (cf. Fig. 3.2b) which features 20 electrical contacts and allows for easy and tool-free sample exchange. The electrical contacts of the chip carrier terminate in the center pins of BNC connectors of a break-out box. Twisted pairs of coaxial cables are used to connect two Hall bar contacts to the differential input of a Stanford Research SR830 lock-in detector. This allows to determine the magnetothermally excited voltage drop across any desired part of the Hall bar. An optical chopper operated at $\nu = 817 - 853\,\mathrm{Hz}$ is used to provide the reference signal for lock-in detection and multiple identical lock-ins are used for a corresponding number of simultaneous magnetothermal voltage measurements. The lock-in phase was identical for all lock-ins used and chosen such that all signal was recorded in the x channel of the instrument. We verified that neither sign nor magnitude of the measured magnetothermally excited voltage is influenced by the lock-in detection scheme in comparison to direct DC voltage measurements using a Keithley 2182 Nanovoltmeter.

Using this experimental setup, we studied several conductive ferromagnetic thin film and insulating ferromagnetic thin film / Pt hybrid samples. Here, we exemplarily discuss the results obtained in thin films of the Heusler compound Co_2FeAl and Ni as well as $Y_3Fe_5O_{12}$/Pt thin film bilayers. The Co_2FeAl thin films were prepared in a collaboration with the University of Bielefeld as described in [144]. The $Y_3Fe_5O_{12}$ (111) thin films were prepared at the Walther-Meißner-Institut by Matthias Althammer using pulsed laser deposition on $Gd_3Ga_5O_{12}$ substrates. The Pt was deposited in situ using electron beam evaporation and the Hall bar was defined in a photolithography / etching process for these samples. The polycrystalline Ni film was prepared by photolithography and electron beam evaporation on a 1 mm thick MgO substrate followed by a lift-off process to define the Hall bar geometry. All investigated samples were patterned into identical 80 µm wide and 900 µm long Hall bars.

3.3 Experimental results and discussion

In this section, we discuss the experimentally obtained local magnetothermal voltages with respect to the contributions of the local anomalous Nernst and spin Seebeck effects. On the basis of Eqs. (3.3) and (3.4) we show that the application of locally confined thermal gradients indeed results in local charge and spin currents that are sensitive to the local magnetization. For a quantitative evaluation of the measurement data, the sample geometry is taken into account and the thermal gradient arising due to the laser beam is calculated. The thus obtained anomalous Nernst and spin Seebeck coefficients N and S_{SSE} are in accordance to literature for Ni and $Y_3Fe_5O_{12}$ (YIG) and the previously unknown Nernst coefficient for Co_2FeAl is derived. Finally, we carried out magnetotransport measurements in YIG/Pt hybrids that indicate magnetic polarization in the Pt close to the ferromagnetic insulator/metal interface. We discuss the possible contribution of Nernst-like effects in magnetically polarized Pt to our measurement signal. Our findings strongly corroborate the interpretation of the magnetothermal voltage in YIG/Pt hybrids on the basis of the local spin Seebeck effect.

3.3.1 Mapping local spin and charge currents

Using the setup introduced above, we first demonstrate magnetothermal domain imaging in a conductive ferromagnetic thin film via the anomalous Nernst effect. The key idea behind the experiments is that since the sample at least partially absorbs the laser light, its intensity and thus the energy deposited decrease as a function of depth. Hence, the energy absorption profile of the laser beam into the film thickness gives rise to a thermal gradient $\nabla T(x, y)$ perpendicular to the sample plane, laterally confined to a region around the position (x, y) of the laser spot [145]. This thermal gradient gives rise to a local electric field $\boldsymbol{E}_{\mathrm{ANE}}(x, y) \propto \boldsymbol{M} \times \nabla T$ (cf. Eq. (3.3)). Temperature gradients within the sample plane are radially symmetric and their contributions to magnetothermal effects thus cancel out.

For the investigation of the local ANE we use a 50 nm thick ferromagnetic Co_2FeAl film deposited on a MgO substrate as schematically depicted in Fig. 3.3a. The film is patterned into the Hall bar geometry shown in Fig. 3.3. This Hall bar geometry and contact numbering scheme is used for all samples discussed in this chapter. We already investigated the magnetic microstructure of this particular Co_2FeAl sample

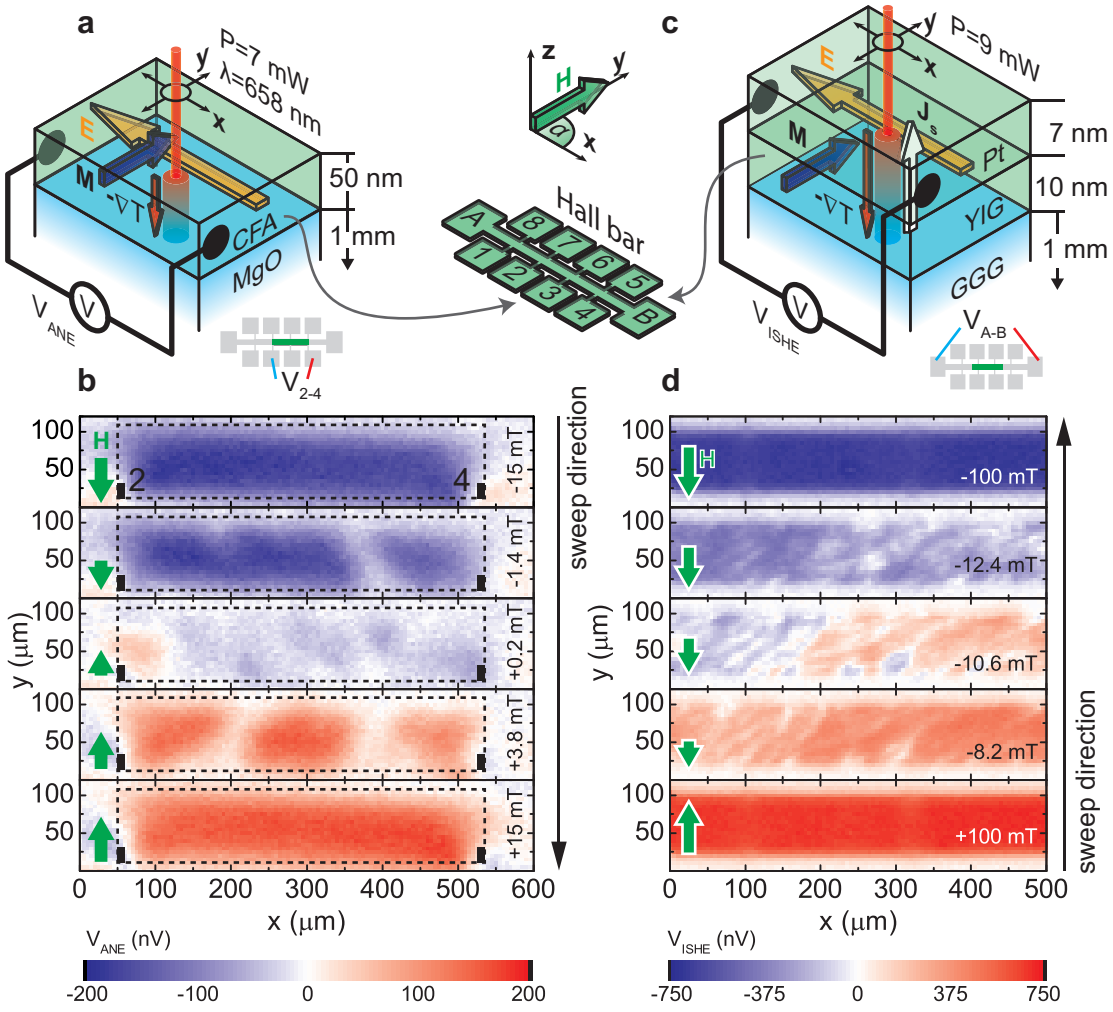

Figure 3.3: **a** The scannable laser beam generates a local temperature gradient ∇T normal to the ferromagnetic thin film plane. The dc voltage V_{ANE} which arises due to the anomalous Nernst effect depends on the local magnetization $\boldsymbol{M}$ at the position (x, y) of the laser beam. **b** V_{ANE} determined between contacts 2 and 4 of a 50 nm thick Co_2FeAl (CFA) Hall bar as a function of the laser-spot position (x, y) and the external magnetic field magnitude $\mu_0 H$ ($\alpha = 90°$). **c** Schematic illustration of the GGG/YIG/Pt sample. The spin Seebeck effect yields a pure, local spin current $\boldsymbol{J}_{\mathrm{s}}$ along ∇T in YIG. $\boldsymbol{J}_{\mathrm{s}}$ depends on the local magnetization $\boldsymbol{M}(x, y)$ and is detected using the inverse spin Hall effect in Pt, which gives rise to a dc voltage V_{ISHE}. **d** V_{ISHE} determined between contacts A and B as a function of the laser-spot position (x, y) and the external magnetic field magnitude $\mu_0 H$ applied along $\boldsymbol{y}$ in a 10 nm YIG / 7 nm Pt hybrid sample.

by spatially resolved magneto-optical Kerr effect measurements [144], such that its typical magnetic domain patterns are known.

Figure 3.3b shows the dc voltage V_{ANE} recorded between the Hall bar contacts 2 and 4 which are separated by approximately 460 µm. For each value of the in-plane magnetic field $\mu_0 H$ applied at an angle $\alpha = 90°$ to the $\boldsymbol{x}$ axis, we scanned the laser beam over the central Hall bar area and recorded $V_{\mathrm{ANE}}(x, y)$ as a function of the laser spot position (x, y). The small full rectangles indicate the location of the used electric contacts and the dashed rectangle depicts the region on the main Hall bar enclosed by said contacts. At $\mu_0 H = -15\,\mathrm{mT}$ ($\boldsymbol{H} \parallel -\boldsymbol{y}$ as indicated by the solid arrow to the left), we observe a voltage $V_{\mathrm{ANE}} \approx -150\,\mathrm{nV}$ in the Hall bar region independent of the laser spot position (x, y). We attribute $V_{\mathrm{ANE}} \propto \boldsymbol{E} \cdot \boldsymbol{x}$ to the anomalous Nernst effect defined in Eq. (3.3). At $\mu_0 H = -15\,\mathrm{mT}$, the film is in magnetic saturation with $\boldsymbol{M} \parallel \boldsymbol{H}$ as shown later. Hence, no magnetic microstructure is present and $V_{\mathrm{ANE}}(x, y)$ does not change as a function of x and y. As the magnetic field magnitude is decreased to $\mu_0 H = -1.4\,\mathrm{mT}$, magnetic domain formation is evident from the V_{ANE} map and at $\mu_0 H = +0.2\,\mathrm{mT}$, V_{ANE} vanishes in the major part of the Hall bar, indicating that $\boldsymbol{M}$ is oriented (anti-)parallel to $\boldsymbol{x}$ and $\boldsymbol{E} \cdot \boldsymbol{x} \propto (\boldsymbol{M} \times \nabla T) \cdot \boldsymbol{x} = 0$. Note that Co_2FeAl has cubic magnetic anisotropy. As a consequence, the magnetic reversal proceeds via two 90° switches [144] such that $\boldsymbol{M} \parallel \boldsymbol{x}$ is a natural intermediate magnetic state. Upon increasing the external magnetic field to $\mu_0 H = +3.8\,\mathrm{mT}$, domains exhibiting $V_{\mathrm{ANE}} > 0$ become visible. In magnetic saturation at $\mu_0 H = +15\,\mathrm{mT}$, $V_{\mathrm{ANE}} \approx +150\,\mathrm{nV}$ in the entire Hall bar region. The sign reversal of V_{ANE} with the reversal of the direction of $\boldsymbol{H}$ (and thus $\boldsymbol{M}$) is a clear indication that the observed V_{ANE} indeed is caused by a term $\nabla T \times \boldsymbol{M}$, which allows to rule out all field-symmetric thermopower effects as the cause of the observed voltage. This is completely analogous to the Nernst signal in the mixed state of superconductors [146–151] which changes sign upon switching the direction of the flux lines [152]. Furthermore, V_{ANE} is a local voltage as can be seen by the fact that $V_{\mathrm{ANE}}(x < 50\,\mu\mathrm{m}, y) = 0$ and $V_{\mathrm{ANE}}(x > 550\,\mu\mathrm{m}, y) = 0$. For these x, the laser still impinges on the main Hall bar, it is however outside the region enclosed by the contacts, rendering them at identical electrical potential. The locality of the observed voltage is discussed in more detail in Section 3.3.3.

We now turn to the generation and detection of local spin currents via the longitudinal spin Seebeck effect in a ferromagnetic insulator exposed to magnetothermal landscapes. We employ a $Gd_3Ga_5O_{12}$ (0.5 mm) / $Y_3Fe_5O_{12}$ (10 nm) / Pt (7 nm) hybrid

sample. The thin film $Y_3Fe_5O_{12}$/Pt (YIG/Pt) bilayer was patterned into the same Hall bar geometry as the Co_2FeAl sample. A schematic view of the sample is shown in Fig. 3.3c. Upon application of a temperature gradient along the hybrid normal, the longitudinal SSE [135] yields a pure spin current $\boldsymbol{J}_\mathrm{s}$ in the YIG film parallel to ∇T which can be detected by exploiting the inverse spin Hall effect in the Pt layer. Note that YIG is an electrical insulator, such that it does not show an anomalous Nernst effect. The Pt layer serves not only as a spin current detector but furthermore as an optical absorber of the laser light.

In Fig. 3.3d, we present a spatially resolved measurement of $V_\mathrm{ISHE} = V_\mathrm{A-B}$ as a function of H. Figure 3.3d thus represents a map of magnetic domains in the ferromagnetic insulator YIG, detected by local electric fields in the Pt layer deposited on top. Note that the images were recorded during a magnetic field downsweep, so the bottommost panel was actually recorded first. At $\mu_0 H = \pm 100\,\mathrm{mT}$ (bottom and top panel), the YIG thin film is in a single domain state with $\boldsymbol{M} \parallel \boldsymbol{H}$. As $\boldsymbol{H}$ is applied along $\boldsymbol{y}$, we can observe $\boldsymbol{E}_\mathrm{ISHE} \propto \boldsymbol{M} \times \nabla T$ along $\boldsymbol{x}$ by probing V_ISHE (cf. Eq. (3.4)). As we used contacts A and B for recording V_ISHE, the laser spot position is located between the used contacts for all values of x in Fig. 3.3d. For all values of y where the laser impinges on the 80 µm wide Hall bar, $V_\mathrm{ISHE} = +640\,\mathrm{nV}$ in magnetic saturation with $\mu_0 H = +100\,\mathrm{mT}$ (bottom panel). Magnetic texture can be observed during the magnetic field sweep in the images recorded with $\mu_0 H = +8.2\,\mathrm{mT}$ to $\mu_0 H = -12.4\,\mathrm{mT}$ (middle panels). As our YIG (111) films show only very small magnetic anisotropy in the film plane, the magnetic domain pattern is more complex than that observed in Co_2FeAl. We note that - while our YIG thin films are electrically insulating - magnetotransport measurements on our YIG/Pt samples showed an anisotropic magnetoresistance $\Delta R/R \approx 7 \times 10^{-4}$ attributed to induced magnetic moments in the Pt thin film close to the interface [153]. However, as detailed in Section 3.3.5, an interpretation of V_ISHE on the basis of Nernst effects in Pt would require implausible Nernst coefficients. We thus attribute the magnetothermal voltage observed to the longitudinal SSE in combination with the inverse spin Hall effect (cf. Eq. (3.4)).

3.3.2 Integral measurements

To quantitatively compare our spatially resolved magnetothermal voltages with the known integral properties, we average V_ANE and V_ISHE within the illuminated regions.

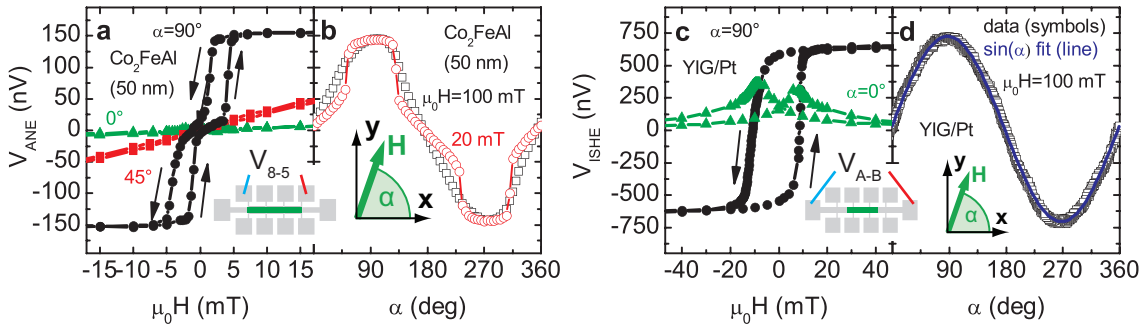

Figure 3.4: **a** Averaged V_{ANE} in Co_2FeAl using the region of interest and contacts shown in the inset as a function of $\mu_0 H$ for $\alpha \in \{0°, 45°, 90°\}$ (triangles, squares, circles). **b** Sine like angular dependency of V_{ANE} on α at $\mu_0 H = 100\,\mathrm{mT}$ (squares). At $\mu_0 H = 20\,\mathrm{mT}$ (circles), the abrupt $\boldsymbol{M}$ switching across the magnetically hard axes (45° and 135°) becomes visible as steps in V_{ANE}. **c** Averaged V_{ISHE} in YIG/Pt within the main Hall bar region as a function of $\mu_0 H$ for $\alpha \in \{0°, 90°\}$ (triangles, circles). **d** V_{ISHE} as a function of α (symbols). The solid curve is a fit to $\sin(\alpha)$ showing excellent agreement with the data.

Such integral measurements are presented in Fig. 3.4, where the insets depict the regions of interest (ROI) used for averaging. In Fig. 3.4a, V_{ANE} in Co_2FeAl is shown as a function of the external magnetic field magnitude $\mu_0 H$ for three different orientations α of the external magnetic field in the plane of the film. For $\alpha = 90°$ (circles), we observe a double step switching behavior indicating cubic magnetic anisotropy. For large H applied at $\alpha = 90°$, $\boldsymbol{M}$ is oriented perpendicular to the main Hall bar. Hence, the generated electric field $\boldsymbol{E}$ is parallel to the main Hall bar and can be probed by the potential difference between the used contacts along $\boldsymbol{x}$. For $\alpha = 45°$, V_{ANE} is smaller, as only the projection of $\boldsymbol{E}$ on the $\boldsymbol{x}$ direction is probed. Furthermore, at this value of α, $\boldsymbol{H}$ is oriented along a magnetically hard axis of the Co_2FeAl film, so hysteresis is minimal. Finally, for $\alpha = 0°$, V_{ANE} vanishes because $\boldsymbol{E}$ is generated along the $\boldsymbol{y}$-direction and thus cannot be detected by voltage contacts aligned along the $\boldsymbol{x}$ direction. The evolution of V_{ANE} as a function of $\boldsymbol{H}$ orientation is shown in more detail in Fig. 3.4b, where V_{ANE} data recorded during a rotation of $\mu_0 H = 100\,\mathrm{mT}$ within the film plane are depicted (squares). A dependence $V_{\mathrm{ANE}} \propto \sin(\alpha)$ is observed in agreement with the cross product found in Eq. (3.3). In an analogous experiment with $\mu_0 H = 20\,\mathrm{mT}$, a similar behavior is found (circles). However, at the four magnetically hard axes along 45°, 135°, 225° and 315°, the magnetization switches abruptly, as evident from the steps in V_{ANE} at these orientations. This shows that the anomalous

Nernst effect measurements can be used to probe magnetic anisotropy in the same fashion as in angular dependent magneto resistance (ADMR) measurements [154], but with spatial resolution.

Figure 3.4c shows $V_{\mathrm{A-B}} = V_{\mathrm{ISHE}} \propto \boldsymbol{E}_{\mathrm{ISHE}} \cdot \boldsymbol{x}$ obtained in the YIG/Pt bilayer as a function of the external magnetic field H for $\alpha = 90°$ (circles) and $\alpha = 0°$ (triangles). As expected from Eq. (3.4), and following the same line of arguments as for V_{ANE}, we observe an antisymmetric V_{ISHE} vs. H behavior for $\alpha = 90°$ while for $\alpha = 0°$, V_{ISHE} vanishes for large values of H. The comparatively large positive V_{ISHE} at the coercive fields for $\alpha = 0°$ is attributed to a small unidirectional in-plane magnetic anisotropy of YIG, which results in domains with $\boldsymbol{M} \parallel \boldsymbol{y}$ during the magnetization switching. This is in accordance to the data obtained with $\alpha = 0°$, where the $\boldsymbol{M}$ hysteresis is not perfectly antisymmetric with respect to the sign of H. Rather, domains with $\boldsymbol{M} \parallel \boldsymbol{y}$ appear to be energetically more favorable than domains with $\boldsymbol{M} \parallel -\boldsymbol{y}$ in our sample, as visible from the more abrupt $\boldsymbol{M}$ switching at positive H. In Fig. 3.4d, we present V_{ISHE} data as a function of α (symbols) recorded with $\mu_0 H = 100\,\mathrm{mT}$ together with a fit to $\sin(\alpha)$ (line). The excellent agreement between fit and data corroborates the cross product in Eq. (3.4). Thus, by exploiting the SSE, it is possible to perform spatially resolved magnetic anisotropy measurements by a magneto-transport based technique even in magnetic insulators.

Taken together, the integral measurements corroborate the interpretation of V_{ANE} and V_{ISHE} on the basis of the anomalous Nernst and spin Seebeck effect in Co_2FeAl and YIG/Pt, respectively. Furthermore, the integral measurements allow for a quantitative comparison of the Nernst and spin Seebeck coefficients determined in our measurements to existing observations in literature. To extract these coefficients from our measurement data, we need to consider the sample geometry and the magnitude of the temperature gradients. These points will be addressed in the following two sections.

3.3.3 Locality of the magnetothermal electric fields

The fact that magnetic microstructure influences the recorded magnetothermal voltages V_{ANE} and V_{ISHE} (cf. Fig. 3.3) strongly suggests that these voltages are due to local electric fields. The assumption of a local electric field implies that the magnitude of the observed magnetothermal voltage should be independent on Hall bar length or contact separation. This is demonstrated using the Co_2FeAl sample already

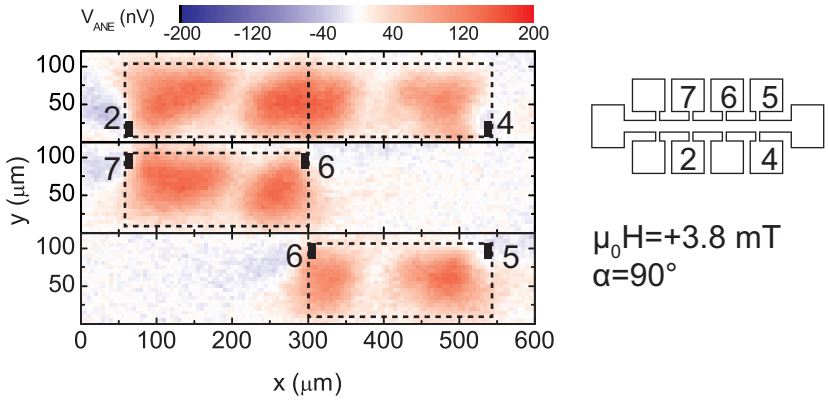

Figure 3.5: V_{ANE} at +3.8 mT in a 50 nm thick Co_2FeAl film for three different sets of contacts. V_{ANE} vanishes for illumination on either side of both contacts. Magnetic microstructure and V_{ANE} magnitude is independent of the contact pair used.

investigated in Section 3.3.1. Figure 3.5 shows data obtained via three simultaneous V_{ANE} measurements using three different sets of contacts at constant magnetic field $\mu_0 H = +3.8\,\mathrm{mT}$. The top panel (contacts 2 and 4) shows V_{ANE} recorded with contacts that are aligned along the main Hall bar and separated by 460 µm. In Fig. 3.5 the contact locations are marked by the dark solid rectangles. The second (contacts 7 and 6 - middle panel) and third (contacts 6 and 5 - bottom panel) set of contacts are both located on the side of the main Hall bar opposite to the first contact pair and are each separated by 230 µm. Clearly, V_{ANE} is finite only if the laser beam and thus the vertical temperature gradient is positioned within the area enclosed by the used contacts. In any case, the observed magnetic microstructure and the magnitude of V_{ANE} are independent of the selected contact pair. These observations provide clear evidence that the electric field is generated only locally at the laser spot position, since V_{ANE} does not depend on the contact separation.

This *local* electric field is experimentally probed by an *integral* voltage measurement. While the Hall bar length thus does not influence the measurement, the Hall bar width should do so due to parallel resistance channels. As illustrated in Fig. 3.6a, in the Hall bar geometry used, we can investigate the magnetothermal voltage generated along the main Hall bar (dark blue) and along a Hall bar tap (light blue). These two sections of the Hall bar not only feature different widths, but furthermore enclose an angle of 90° with respect to their long sides. To determine the dependence of the magnetothermal voltage on Hall bar width and orientation in the experiment,

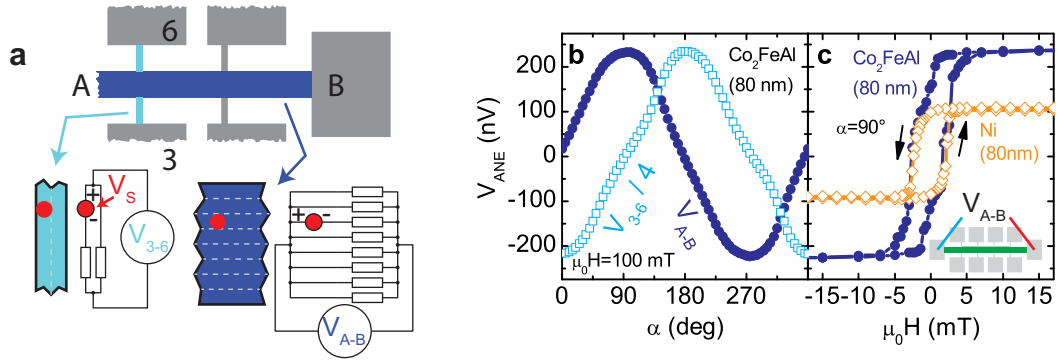

Figure 3.6: **a** Schematic view and equivalent circuits of the main Hall bar (dark shading) and contact line (light shading) with parallel resistors and ideal voltage source V_s at the laser spot position (solid circle). **b** V_ANE as a function of α for illumination on the 80 µm wide central Hall bar (solid symbols) and for illumination on the 20 µm wide contact line (open symbols). **c** $V_\mathrm{ANE} = V_\mathrm{A-B}$ averaged within the region indicated in the inset as a function of $\mu_0 H$ in a Co_2FeAl and a Ni sample.

we measured V_ANE simultaneously at two contact pairs on a 80 nm thick Co_2FeAl film sample as a function of α. We used the orthogonal contact pairs A and B as well as 3 and 6 to obtain $V_\mathrm{A-B}$ and V_{3-6}, respectively. Hereby, $V_\mathrm{A-B}$ is the averaged voltage for illumination within the main Hall bar (dark blue in Fig. 3.6a) and V_{3-6} is averaged while scanning the laser within the light blue Hall bar tap regions in Fig. 3.6a. The results of the magnetothermal voltage measurements are presented in Fig. 3.6b and correspond to the projection of $\boldsymbol{E}$ to the $\boldsymbol{x}$ and $\boldsymbol{y}$ axis, respectively. While $V_\mathrm{A-B} \propto \sin(\alpha)$ (closed symbols), $V_{3-6} \propto -\cos(\alpha)$ (open symbols). This angular dependency of V_ANE again corroborates $\boldsymbol{E}_\mathrm{ANE} \propto \boldsymbol{M} \times \nabla T$, i.e., Eq. (3.3). Turning to the V_ANE magnitude in Fig. 3.6b, we find that the magnitude of $V_{3-6}(\alpha = 180°)$ is exactly four times the magnitude of $V_\mathrm{A-B}(\alpha = 90°)$ (note the scaling of V_{3-6} in the figure). The Hall bar width w in the region probed by $V_\mathrm{A-B}$ (dark shading) was 80 µm, while that in the region probed by V_{3-6} (light shading) was 20 µm. The voltage V observed in magnetocaloritronic experiments thus scales with w^{-1}. This is in accordance to the geometry introduced in Fig. 3.6a, considering the magnetothermal generation of a local electromagnetic force at the laser spot position shunted by the unperturbed (non-illuminated) Hall bar cross-section. We assume the locally generated voltage $V_\mathrm{s} = E \cdot d$ to be an ideal, homogeneous voltage source within the laser spot width $d = 10$ µm for simplicity. The Hall bar resistance is then modeled by a series of parallel resistances, at the position of one of which V_s is generated. The

detected voltage V thus is:

$$V = \frac{d}{w} V_\mathrm{s} \,. \tag{3.5}$$

This expression is, in particular, independent of the resistivity of the thin film (the resistance R of the resistors sketched in Fig. 3.6a) and of Hall bar length. The magnitude of V for a given thermal landscape is inversely proportional to the structure width w. As V increases with decreasing structure size, the technique described in this work is thus particularly applicable to micro- or nanoscale devices.

To demonstrate the general nature of spin caloritronics, we carried out magnetocaloritronic measurements in a set of further samples. We observed V_ANE in thin films of all three elemental ferromagnets, iron, cobalt and nickel and recorded V_ISHE in a further GGG/YIG/Pt sample. Exemplarily, in Fig. 3.6c, we compare data obtained at an incident laser power $P = 9\,\mathrm{mW}$ and a $\boldsymbol{H}$ orientation $\alpha = 90°$ in a 80 nm thick Ni film with data obtained in the already introduced 80 nm thick Co_2FeAl sample, both patterned into identical Hall bar geometry. The data correspond to V_ANE averaged for illumination within a region of interest (ROI) on the main Hall bar as indicated by the inset. Note that the maximum magnitude of $V_\mathrm{A-B}$ in Co_2FeAl observed in Fig. 3.6b is identical to that in Fig. 3.6c, regardless of the different magnetic field strengths ($\mu_0 H = 20\,\mathrm{mT}$ vs. $\mu_0 H = 100\,\mathrm{mT}$). This shows that the contributions due to the conventional Nernst effect (which scales with H instead of M) are negligible in our experiments. While the shapes of the V_ANE hysteresis loops reflect the thin films' respective magnetic anisotropy, the magnitude of V_ANE is approximately twice as large in the Co_2FeAl thin film. Considering $V_\mathrm{ANE} \propto M_\mathrm{s}$ (cf. Eq. (3.3)), we attribute this mainly to the larger saturation magnetization $M_\mathrm{s} = 1050\,\mathrm{kA/m}$ of Co_2FeAl as opposed to $M_\mathrm{s} = 370\,\mathrm{kA/m}$ in Ni.

Using Eq. (3.5), we can now calculate the electric fields generated in our measurements. For the ANE measurements in Ni we obtain $E_\mathrm{ANE} = V_\mathrm{s}/d = \frac{w}{d^2} \cdot V_\mathrm{ANE} = 87\,\mathrm{mV/m}$ with $V_\mathrm{ANE} \approx 109\,\mathrm{nV}$ taken from Fig. 3.6c. Accordingly, for Co_2FeAl we obtain $E_\mathrm{ANE} = 176\,\mathrm{mV/m}$ (cf. Fig. 3.6c). For the V_ISHE measurements in YIG/Pt, identical considerations apply and we obtain $E_\mathrm{ISHE} = \frac{w}{d^2} \cdot V_\mathrm{ISHE} = 512\,\mathrm{mV/m}$ (cf. Fig. 3.4c). In order to quantitatively determine either the Nernst coefficient N or the longitudinal spin Seebeck coefficient S_SSE of the respective materials from these electric fields, a quantitative knowledge of the temperature gradients driving the magnetothermal voltages V_ANE and V_ISHE is required.

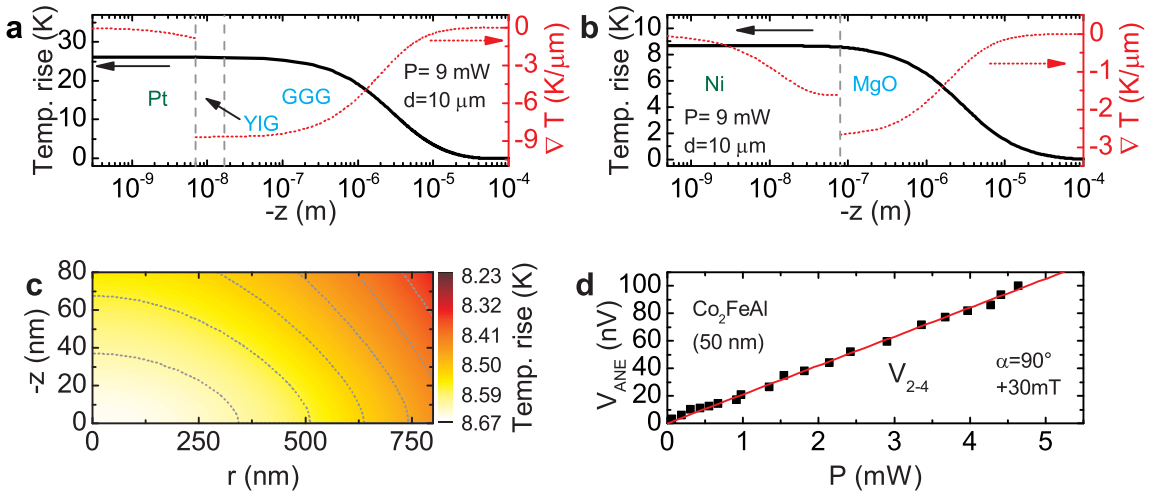

Figure 3.7: **a** Calculated temperature profile (solid line, left scale) and gradient (dotted line, right scale) in a Pt (7 nm) on YIG (10 nm) / GGG (1 mm) sample in the direction of the film normal $\boldsymbol{z}$ for an incident laser power $P = 9\,\mathrm{mW}$ and a Gaussian laser beam profile with a diameter of 10 µm. **b** Corresponding calculation for a Ni (80 nm) on MgO (1 mm) sample. **c** The radially symmetric temperature profile in the Ni film as a function of depth z and radial coordinate r. **d** V_{ANE} scales linearly with laser power (symbols are measured data, line is a linear fit)

3.3.4 Thermal landscape generation

A direct quantitative measurement of the temperature gradient induced by the laser beam in our experimental setup is difficult. A spatially resolved technique would be required to determine the local temperature gradient at the position of the laser spot. Moreover, one would need to determine the temperature at various positions *within* the bulk of the sample which can not be done straightforward by, e.g., infrared thermography [155]. However, the temperature gradient induced by a laser beam with Gaussian profile impinging on a multilayered sample can be calculated analytically as shown by Reichling and Grönbeck [145]. The calculated temperature profile then allows for a quantitative evaluation of the anomalous Nernst and spin Seebeck coefficients of our samples. Since not all required material parameters are known for Co_2FeAl, we carried out the calculation for MgO/Ni and GGG/YIG/Pt.

We start by calculating the local temperature rise in GGG/YIG/Pt due to the laser heating. To this end, the quite lengthy formulae derived for the temperature rise $T_0(r, z)$ to $T_3(r, z)$ as a function of radial coordinate r and depth z in a

four-layered system [145] were used and embedded into a Wolfram Mathematica 8 workbook. The result of the calculation for a laser chopping frequency of 853 Hz and an incident laser power $P = 9\,\mathrm{mW}$ is shown in Fig. 3.7a. We plot T as a function of the position z along the film normal at the center of the laser beam (left scale), with $z < 0$ corresponding to positions within the sample. The right scale shows the temperature gradient $\nabla T(z)$. We assumed the four layers air, Pt, YIG/GGG, air with identical thermal and optical properties of YIG and GGG and used the following material parameters: $a_{\mathrm{Pt}} = 82 \times 10^6\,/\mathrm{m}$ and $a_{\mathrm{YIG}} = 0$ for the absorption coefficients, $R_{\mathrm{Pt}} = 0.68$ and $R_{\mathrm{YIG}} = 0.08587$ for the reflectivities, with values taken from Ref. [156]. For the thermal properties we used $\kappa_{\mathrm{Air}} = 0.02\,\mathrm{W/Km}$, $\kappa_{\mathrm{Pt}} = 71.6\,\mathrm{W/Km}$ [157] and $\kappa_{\mathrm{YIG}} = 7\,\mathrm{W/Km}$ [158] for the thermal conductivities and $c_{\mathrm{Air}} = 1000\,\mathrm{J/kgK}$ [159], $c_{\mathrm{Pt}} = 130\,\mathrm{J/kgK}$ and $c_{\mathrm{YIG}} = 570\,\mathrm{J/kgK}$ for the heat capacities. Finally, $\rho_{\mathrm{Air}} = 1.2\,\mathrm{kg/m^3}$, $\rho_{\mathrm{Pt}} = 21450\,\mathrm{kg/m^3}$ [157] and $\rho_{\mathrm{YIG}} = 5245\,\mathrm{kg/m^3}$ were taken as the respective densities. We obtain a mean temperature gradient of approximately $\nabla T = -8.7\,\mathrm{K/\mu m}$ in the YIG close to the Pt interface. In the Pt layer, the mean temperature gradient amounts to $\nabla T = -0.6\,\mathrm{K/\mu m}$.

For the determination of N, we calculated the temperature profile considering a 80 nm thick Ni film on a 1 mm thick MgO substrate. We used the following material parameters: $a_{\mathrm{Ni}} = 73 \times 10^6\,/\mathrm{m}$ and $a_{\mathrm{MgO}} = 0$ for the absorption coefficients, $R_{\mathrm{Ni}} = 0.66071$ and $R_{\mathrm{MgO}} = 0.071970$ for the reflectivities, with values taken from Ref. [156] at $\lambda = 658\,\mathrm{nm}$. For the thermal properties we used $\kappa_{\mathrm{Air}} = 0.02\,\mathrm{W/Km}$ [160], $\kappa_{\mathrm{Ni}} = 90\,\mathrm{W/Km}$ [161] and $\kappa_{\mathrm{MgO}} = 53\,\mathrm{W/Km}$ [162] for the thermal conductivities and $c_{\mathrm{Air}} = 1000\,\mathrm{J/kgK}$ [159], $c_{\mathrm{Ni}} = 439\,\mathrm{J/kgK}$ [163] and $c_{\mathrm{MgO}} = 960\,\mathrm{J/kgK}$ [164] for the heat capacities. Finally, $\rho_{\mathrm{Air}} = 1.2\,\mathrm{kg/m^3}$, $\rho_{\mathrm{Ni}} = 8900\,\mathrm{kg/m^3}$ [157] and $\rho_{\mathrm{MgO}} = 3580\,\mathrm{kg/m^3}$ were taken as the respective densities. The calculated temperature T, considering the same laser beam profile as above with $d = 10\,\mu\mathrm{m}$ diameter, a laser power of $P = 9\,\mathrm{mW}$ and a chopping frequency of 817 Hz are shown in Fig. 3.7b. The temperature gradient ∇T along $\boldsymbol{z}$ (right scale) is in average $-1.4\,\mathrm{K/\mu m}$ in the Ni thin film.

Figure 3.7c shows the temperature in the Ni film as a function of z and the radial coordinate r, with $r = 0$ corresponding to the center of the laser beam. The temperature gradient along z is roughly one order of magnitude larger than that along r. Furthermore, as the lateral temperature gradient is radially symmetric, its contributions to the conventional Seebeck effect cancel out and thus need not to be considered in the interpretation of data presented here.

Both, the ANE and the SSE scale linearly with the temperature gradient (cf. Eqs. (3.3) and (3.4)). We experimentally checked the dependence of the effects on the incident laser power which again is proportional to ∇T [145]. Exemplarily, Fig. 3.7d shows V_{ANE} measured in a sample featuring a 50 nm thick Co_2FeAl film deposited on MgO substrate as a function of laser power P, with illumination on the central part of the main Hall bar in between the used contacts 2 and 4, and the magnetic field applied perpendicular to the main Hall bar. We observe the expected linear dependence of V_{ANE} on P. Note that the maximum power in this experiment was lower than 9 mW due to the insertion of a rotatable filter wheel into the optical path. This was necessary to adjust the laser power impinging on the sample, but resulted in imperfect coupling of the laser beam into the optical fiber and thus lowered the laser power emitted at the scannable collimator.

These calculations show that a scannable, focussed laser beam impinging on either ferromagnet or ferromagnet/normal metal thin film samples can be used for a controllable thermal landscape generation with substantial, laterally confined, temperature gradients along the sample normal.

Having calculated the temperature gradient ∇T evoked by the laser heating as well as the local magnetothermal electric fields, we can quantify the anomalous Nernst coefficient N and the spin Seebeck coefficient S_{SSE} of the investigated samples as evident from Eqs. (3.3) and (3.4). We first turn to the evaluation of the anomalous Nernst coefficient of Ni, using the calculated temperature gradient and electric field. As discussed above, the temperature gradient is $\nabla T = -1.4\,\mathrm{K/\mu m}$. Using a saturation magnetization $M_{\mathrm{s}} = 370\,\mathrm{kA/m}$ obtained by SQUID magnetometry [13] and the experimentally measured $E = 87\,\mathrm{mV/m}$, we obtain the Nernst coefficient $N_{\mathrm{Ni}} = 1.3 \times 10^{-7}\,\mathrm{V/KT}$ which is lower than values $N_{\mathrm{Ni}} \approx 5 \times 10^{-7}\,\mathrm{V/KT}$ found for bulk Ni [165] at room temperature. A comparable reduction of a caloritronic property with respect to bulk material was recently reported for the Seebeck coefficient in Ni thin films [166]. Assuming comparable optical and thermal properties for Co_2FeAl and thus $\nabla T = -1.4\,\mathrm{K/\mu m}$ in a 80 nm thick Co_2FeAl sample with $M_{\mathrm{s}} = 1050\,\mathrm{kA/m}$ obtained by SQUID magnetometry, we estimate $N_{\mathrm{CFA}} \approx 9.5 \times 10^{-8}\,\mathrm{V/KT}$.

We now turn to the longitudinal spin Seebeck coefficient of the YIG/Pt bilayer. Using a calculated mean temperature gradient of $\nabla T = -8.7\,\mathrm{K/\mu m}$ in the YIG thin film, we obtain a spin Seebeck coefficient $S_{\mathrm{SSE}} = 5.9 \times 10^{-8}\,\mathrm{V/K}$, compared to $S_{\mathrm{SSE}} = 1 \times 10^{-7}\,\mathrm{V/K}$ found in [135]. We assume that the small difference in S_{SSE} is

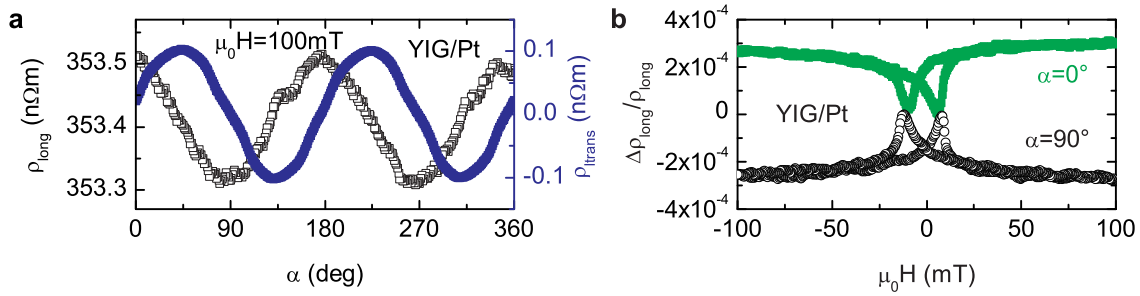

Figure 3.8: **a** ADMR measurements of ρ_{long} (left scale, open squares) and ρ_{trans} (right scale, solid circles) in YIG/Pt with $\mu_0 H = 100\,\mathrm{mT}$ reveals an AMR of $\Delta\rho/\rho \approx 7 \times 10^{-4}$. **b** ρ_{long} as a function of H for $\alpha = 90°$ (open circles) and $\alpha = 0°$ (solid squares) shows coercive fields identical to that of YIG.

due to different interfaces of Pt and YIG as well as different Pt thicknesses. Taken together, the calculated Nernst and spin Seebeck coefficients are in accordance to values found in the literature, quantitatively corroborating the interpretation of our measurement results based on Eq. (3.3) and (3.4).

3.3.5 Magnetotransport in YIG/Pt

The interpretation of the magnetothermal voltage in the YIG thin film sample given above is based on the spin Seebeck effect. As YIG is a ferromagnetic insulator, it should not show any Nernst-like effects since the latter requires charge motion. However, Pt may become magnetically polarized in the vicinity of a ferromagnet [153,167]. This so-called proximity effect has not yet been reported for YIG/Pt thin film samples, indications for this effect can however be revealed in, e.g., magnetotransport measurements. As such a proximity effect yields magnetically polarized Pt that may show Nernst effects, it is mandatory to exclude them as the origin of V_{ISHE}. This is particularly cumbersome since the anomalous Nernst effect and the inverse spin Hall effect used to detect the spin Seebeck effect show identical symmetry as evident from Eqs. (3.3) and (3.4). Hence, a quantitative analysis of the proximity effect in ferromagnet/Pt bilayers is an important aspect for the understanding of the spin Seebeck effect. To this end, element-specific magnetometry is required. Such an investigation with x-ray magnetic circular dichroism (XMCD) as performed in Refs. [153, 167] was beyond the scope of this thesis. However, we measured the electrical resistivity of the Pt thin film in GGG/YIG/Pt samples as a function of the external magnetic field

strength and orientation and found indications for a magnetic polarization of the Pt thin film as discussed in the following.

Our pure YIG films (GGG/YIG(10 nm)) are electrically insulating with a resistivity in excess of 20 Ωm. This resistivity corresponds to the maximum resistance that can be determined by the Keithley 2410 sourcemeter that was used for the measurement. However, the finite electrical resistivity of the Pt layer in the YIG/Pt sample discussed here is dependent on the external magnetic field. We determined V_{1-4} (longitudinal voltage) and V_{3-6} (transversal voltage) in a 4 point magnetotransport measurement with currents $I_{\mathrm{A-B}}$ ranging from 0.1 mA to 2 mA. The calculated resistivities ρ_{long} and ρ_{trans} obtained in a measurement with $I = 1\,\mathrm{mA}$ along contacts A-B are shown as a function of magnetic field orientation (angular dependent magnetoresistance measurement [154]) in Fig. 3.8a. Clearly, $\rho_{\mathrm{long}} \propto \cos^2(\alpha)$ (open symbols, left scale) and $\rho_{\mathrm{trans}} \propto \sin(2\alpha)$ (solid symbols, right scale) show the characteristic signature of anisotropic magnetoresistance (AMR) [168]. Furthermore, as shown in Fig. 3.8b, ρ_{long} shows switching fields coinciding with the coercive field $\mu_0 H_{\mathrm{c}} \approx 10\,\mathrm{mT}$ of our YIG thin film. In accordance to the expectations for AMR, the switching changes direction under a rotation of $\boldsymbol{H}$ of 90°. This can be observed in Fig. 3.8b, where the curve recorded for $\alpha = 0°$ appears reflected along the horizontal axis with respect to the curve obtained at $\alpha = 90°$. The total AMR amounts to $\left(\rho_{\mathrm{long}}(\mu_0 H) - \rho_{\mathrm{long}}(\mu_0 H_{\mathrm{c}})\right) / \langle \rho_{\mathrm{long}} \rangle =: \Delta\rho_{\mathrm{long}}/\rho_{\mathrm{long}} \approx 7 \times 10^{-4}$, with the mean longitudinal resistivity $\langle \rho_{\mathrm{long}} \rangle$ and the coercive magnetic field $\mu_0 H_{\mathrm{c}}$. The thus determined AMR is about a factor of 10 lower than usually observed in elemental conductive ferromagnets [168]. The AMR ratio was independent of I in the range of $0.1\,\mathrm{mA} \leq I \leq 2\,\mathrm{mA}$, ruling out thermoelectric effects due to Joule heating as the cause of the magnetoresistance.

We attribute the magnetoresistance to induced magnetic moments in the Pt layer close to the YIG/Pt interface. This proximity effect is expected for clean interfaces within the first few monolayers (≈ 1 nm) of Pt [153,167], explaining the small AMR, as only a fraction of the Pt is magnetized and thus contributes to the magnetoresistance. Because of the identical symmetry of the longitudinal SSE and the ANE, one needs to consider a possible ANE contribution of the magnetized Pt to the measured voltage. Assuming that the entire Pt layer is magnetized with a magnetization identical to YIG, ($M_{\mathrm{s}}^{\mathrm{YIG}} = 127\,\mathrm{kA/m}$ obtained by Matthias Althammer using SQUID magnetometry), and using the calculated mean temperature gradient in the Pt film, $\nabla T = -0.6\,\mathrm{K/\mu m}$

(cf. Fig. 3.7a), an anomalous Nernst coefficient $N_{\mathrm{Pt}} = 5.3 \times 10^{-6}\,\mathrm{V/KT}$ needs to be assumed to explain $V_{\mathrm{ISHE}} = 640\,\mathrm{nV}$ (cf. Fig. 3.4c) based on an ANE in magnetized Pt alone. This coefficient is more than one order of magnitude larger than the ANE coefficient of Ni and Co_2FeAl determined above - even with the unrealistic assumption of an entirely magnetized Pt film (as detailed above, only a fraction of the Pt thin film is expected to be magnetized due to the proximity effect, in accordance to the small AMR). Furthermore this Nernst coefficient would be two orders of magnitude larger than the Nernst coefficient of Pt, $N_{\mathrm{Pt}} = 1.3 \times 10^{-8}\,\mathrm{V/KT}$ [169], ruling out a Nernst effect in the Pt layer in the stray field of the YIG thin film as the origin of V_{ISHE}. Assuming $N_{\mathrm{Pt}} = N_{\mathrm{Ni}} = 1.3 \times 10^{-7}\,\mathrm{V/KT}$ and that only half of the Pt film is magnetized to $M_{\mathrm{s}}^{\mathrm{YIG}}$ and with $\nabla T = -0.7\,\mathrm{K/\mu m}$ averaged in the first 3.5 nm of Pt at the YIG interface (cf. Fig. 3.7a), we can calculate the expected maximum voltage due to an ANE as $V_{\mathrm{ANE}} \approx 9\,\mathrm{nV}$ for our YIG/Pt measurement, as opposed to $V_{\mathrm{ISHE}} \approx 640\,\mathrm{nV}$ actually measured. Hence, we conclude that Nernst effects due to the proximity effect in Pt are at most a small contribution ($< 2\%$) to V_{ISHE} and we thus attribute V_{ISHE} to the longitudinal spin Seebeck effect. This is furthermore supported by the calculated spin Seebeck coefficient $S_{\mathrm{SSE}} = 5.9 \times 10^{-8}\,\mathrm{V/K}$ which is in accordance to literature [135]. Clearly, further detailed experiments as a function of, e.g., Pt thickness and using other normal metals will be mandatory to fully address this issue. Moreover, element specific magnetometry studies of the proximity effects in Pt/ferromagnet samples are needed to establish a full quantitative understanding of spin Seebeck effects detected via the inverse spin Hall effect. This is particularly important as even in the conventional spin Seebeck geometry, spurious temperature gradients exist and are known to give rise to anomalous Nernst effects [136].

3.4 Conclusions and outlook

In this chapter, we have demonstrated that both, well established charge current-based, as well as novel spin current-based magnetothermal effects, are sensitive to magnetic microstructure. The local anomalous Nernst effect was exploited to image magnetic texture in conductive ferromagnetic thin films and it was shown that such measurements allow for a spatially resolved determination of the magnetization orientation. Thus, the local anomalous Nernst effect (LANE) is a complementary approach to the magneto-optic Kerr effect [170, 171] (MOKE) and scanning laser mi-

croscopy [172–174] (SLM) for the investigation of magnetic domains in ferromagnetic conductors. Key differences of these approaches are, e.g, that different material properties are relevant for the signal generation. While MOKE measurements rely on high Kerr rotation angles and high optical reflectivities, SLM measurements require a pronounced temperature dependence of the magnetoresistance. In contrast, LANE measurements profit from high Nernst coefficients and high optical absorptions. Furthermore, the LANE measurements introduced in this chapter offer the advantage of full 360° confidence of the magnetization orientation determined by means of two simultaneous "orthogonal" voltage measurements.

In a complimentary set of experiments, we took advantage of the longitudinal spin Seebeck effect in ferromagnetic insulator/normal metal hybrids and performed local spin-current caloritronic measurements. The local spin Seebeck effect (LSSE) allows for an electrical detection of magnetic domains even in a ferromagnetic insulator such as YIG. Thus, using one and the same setup, magnetic microstructure can be investigated in fundamentally different ferromagnets, based on fundamentally different physical phenomena.

Our setup allows for the generation of a local, magnetically controllable, electric field via the anomalous Nernst effect in conductive ferromagnets. Our results furthermore suggest that in magnetic insulator/normal metal hybrids, a spatially confined temperature gradient gives rise to local, pure spin currents with magnetically selectable spin polarization due to the longitudinal spin Seebeck effect.

We furthermore quantitatively evaluated the Nernst coefficients of Ni and Co_2FeAl thin films as well as the spin Seebeck coefficient of a YIG/Pt thin film bilayer. This evaluation was carried out by taking into account the locality of the caloritronic effects and sample geometry. Moreover, the thermal gradient induced by a scanning laser beam in our samples was quantitatively calculated based on a heat flow model taken from literature. The Nernst and spin Seebeck coefficients of Ni and YIG/Pt were found to be in accordance to values reported in literature and the unpublished Nernst coefficient of Co_2FeAl was derived. These findings strongly corroborate the interpretation of our experimental data based on the local anomalous Nernst and spin Seebeck effects and opens exciting perspectives for the generation and use of pure spin currents, both in basic research and in applications.

Note that the investigated caloritronic effects are based on either charge or spin current flow and thus are fundamentally different. However, the voltages observed in

the experiment to detect said effects share a common signature owing to the identical symmetry of the anomalous Nernst effect and the inverse spin Hall effect. This implies that these two effects cannot be separated by their symmetry with respect to magnetization orientation or thermal gradient. We excluded a possible anomalous Nernst effect in magnetically polarized Pt in our ferromagnet/Pt bilayers based on a quantitative evaluation of magnetotransport data.

For future experiments, simultaneously acquisition of the spatially resolved MOKE and LANE/LSSE is an important goal, as this would allow for a direct comparison of optically and thermoelectrically detected magnetic microstructure. The experimental setup is currently being modified to this end as part of the Diploma thesis of Michael Schreier.

Even more importantly, the proximity polarization of Pt in ferromagnet/Pt bilayers and the clear separation of anomalous Nernst and spin Seebeck effects needs to be addressed. This is a key issue for phonon-spin interactions, as Pt is used as a spin current detector in the vast majority of publications concerning spin pumping and the spin Seebeck effect. However, a possible proximity-induced spin polarization in Pt so far has been neglected in the discussion of these experiments. Furthermore, thermal distributions in thin film/substrate hybrids are dominated by the thermal properties of the substrate [175] which may lead to spurious thermal gradients. These may in turn give rise to anomalous Nernst effects that are superimposed on the inverse spin Hall signal. Hence, a quantitative evaluation of the magnitude and orientation of the thermal gradients is essential for experiments concerning caloritronic effects. To separate charge and spin current driven contributions to the experimentally determined voltages, samples with several different bilayer compositions on one and the same substrate would be advantageous. In a sample consisting, e.g., of a Ni thin film Hall bar which is partially covered by Pt, one could investigate the ANE for itself by illuminating only the Ni as well as a combination of SSE and ANE by illuminating Ni/Pt. Temperature-dependent measurements in such samples may furthermore provide a way to separate ANE and SSE driven contributions to the magnetothermal voltage. To this end, the optical fiber and appropriately miniaturized scanning electronics could be transferred into the variable temperature inset of a magnet cryostat.

Besides these experiments that address a more thorough understanding of the physical mechanisms behind the results presented in this thesis, one may transfer the concepts introduced here using a quasi-static thermal gradient to a dynamic thermal

perturbation. Using pulsed laser heating in ferromagnetic thin films, it should be possible to generate heat waves up to the radio frequency regime. Measuring the spin-current generation as a function of lattice excitation frequency should allow to study the transition between the static spin Seebeck effect and dynamic spin pumping. Furthermore, time-resolved studies of the generated spin currents are a so far unexplored experimental field that may provide a significant contribution towards establishing a fundamental understanding of magnon-phonon interactions.

Chapter 4

Summary and outlook

In this thesis, we investigated both resonant and non-resonant magnon-phonon interaction phenomena in ferromagnetic thin films. We conclude with a brief summary of the main results obtained. Inspired by these results, we then give an outlook on future experiments that combine and expand the concepts applied in this thesis to establish a more complete picture of the fundamental physics behind magnon-phonon interactions.

4.1 Summary

In Chapter 1, we demonstrated that the radio frequency, magnetoelastic interaction of coherent phonons with the magnetization of a ferromagnet can be exploited to excite acoustically driven ferromagnetic resonance (FMR). In our experiments, a radio frequency surface acoustic wave (SAW) propagates through a ferromagnetic thin film. We prepared ferroelectric substrate/ ferromagnetic thin film samples by means of photolithography and electron beam evaporation and devised and assembled an experimental setup allowing for fully automated vector network analysis of these samples in a rotatable electromagnet. Using this setup, we measured the SAW transmission as a function of the external magnetic field magnitude and orientation. We found that the SAW is resonantly absorbed at characteristic external magnetic field configurations. Corresponding model calculations based on a modified Landau-Lifshitz-Gilbert approach revealed that the SAW absorption is caused by the excitation of resonant magnetization precession in the ferromagnetic thin film. Experiments and simulation were in full quantitative agreement. From our simulations, we found that the purely virtual magnetoelastic driving field of the acoustic FMR bears a characteristic sym-

metry with respect to equilibrium magnetization orientation and phonon propagation direction. This "fingerprint" of the elastic FMR results in characteristic differences and similarities to conventional, photon-driven FMR. The acoustically driven FMR opens the path for a detailed investigation of the physical principles of the resonant magnon-phonon interaction. In particular, the relaxation of the magnetoelastically excited magnetization can take place via the emission of a spin current. In this fashion, phonons can be used as a spin current source.

The observation of such a resonant phonon-driven spin current generation is the key result of Chapter 2. In the experiments discussed in this chapter, we used radio frequency SAW pulses to elastically excite FMR in a ferromagnetic thin film. A normal metal thin film was deposited on top of the ferromagnet and we used the dc voltage arising due to the inverse spin Hall effect in the normal metal as a spin-current detector. The experimental setup already introduced in Chapter 1 was modified to allow for pulsed radio frequency SAW generation and voltage detection using an oscilloscope. In our time-resolved experiments, we were able to clearly separate photon- and phonon-driven contributions to the dc voltage. We found conclusive evidence for all-elastic spin current generation in the exclusive presence of an acoustic excitation. Corresponding calculations that took into account the SAW amplitude and the magnetoelastic properties of the ferromagnet showed that the magnitude and magnetic field dependence of the measured dc voltage complies with the present understanding of the spin pumping effect. Thus, our experiments demonstrate that spin pumping is a general phenomenon that is independent of the mechanism driving the resonant magnetization precession.

The spin Seebeck effect is a recently discovered and highly attractive way for phonon-driven spin current generation. It expands the field of thermomagnetic effects so that not only charge but also spin currents can be driven by a thermal gradient. In Chapter 3, we investigated the interplay of magnetic microstructure and the charge and spin currents arising due to the anomalous Nernst and the spin Seebeck effect. We conceived and assembled a setup that employs a scanning laser beam to induce local out-of-plane temperature gradients in samples of conductive ferromagnetic thin films and insulating ferromagnet / normal metal thin film bilayers. An external magnetic field can be applied in the film plane by means of a home-built 2D vector magnet. In our room temperature experiments, we found that both, charge and spin currents, are sensitive to magnetic texture, while their integral caloritronic properties are in accor-

dance to literature. Our experimental results suggest that magnetothermal landscapes can be used to establish local, bipolar charge and spin current sources. In this sense, our findings expand the integral investigation of spin caloritronic properties in the literature towards spatially resolved approaches.

4.2 Outlook

The results presented in this thesis provide the basis for further intriguing experiments concerned with magnon-phonon interactions. As all experiments discussed in this work were performed at room temperature using a small selection of materials, studies of the investigated phenomena as a function of temperature and material will reveal further details of the coupling mechanisms between magnetic properties and lattice excitations. In the following, we discuss possible next experimental steps that go beyond these variations of experimental parameters.

Our experiments with surface acoustic waves and ferromagnetic thin films showed that ferromagnetic resonance can be driven all elastically. We exclusively used Rayleigh-type SAWs to elastically drive FMR. This yielded a characteristic, four-fold symmetry of the virtual magnetoelastic tickle field and implies that other types of acoustic waves, e.g., shear horizontal surface acoustic waves (SHSAW), show distinctly different symmetries of the internal acoustic tickle field with respect to magnetization orientation [53]. Using $LiTaO_3$ as a substrate material, SHSAWs can be generated and detected. Thus, repeating our experiments using, e.g., SHSAWs is an appealing approach to verify the predictive power of our phenomenological model.

In the phenomenological model just mentioned, the magnetoelastic driving field replaces the conventionally applied, external rf magnetic field in the Landau-Lifshitz-Gilbert equation. However, while the magnetization dynamics hence can be described in a unified model regardless of the nature of the excitation mechanism, the back-action of the precessing magnetization on the SAW needs to be investigated in more detail. As we detect the acoustically driven FMR by a change in SAW amplitude and phase, such a back-action is measurable. Fundamentally, as discussed in Chapter 1, the power absorbed from the SAW in FMR can be measured and quantitatively modeled. Phenomenological models for the back-action of the acoustically driven FMR on the elastic properties of the ferromagnet [27,28,53,176] suggests that in FMR the elastic constants of the ferromagnet change. This needs to be verified experimentally. To

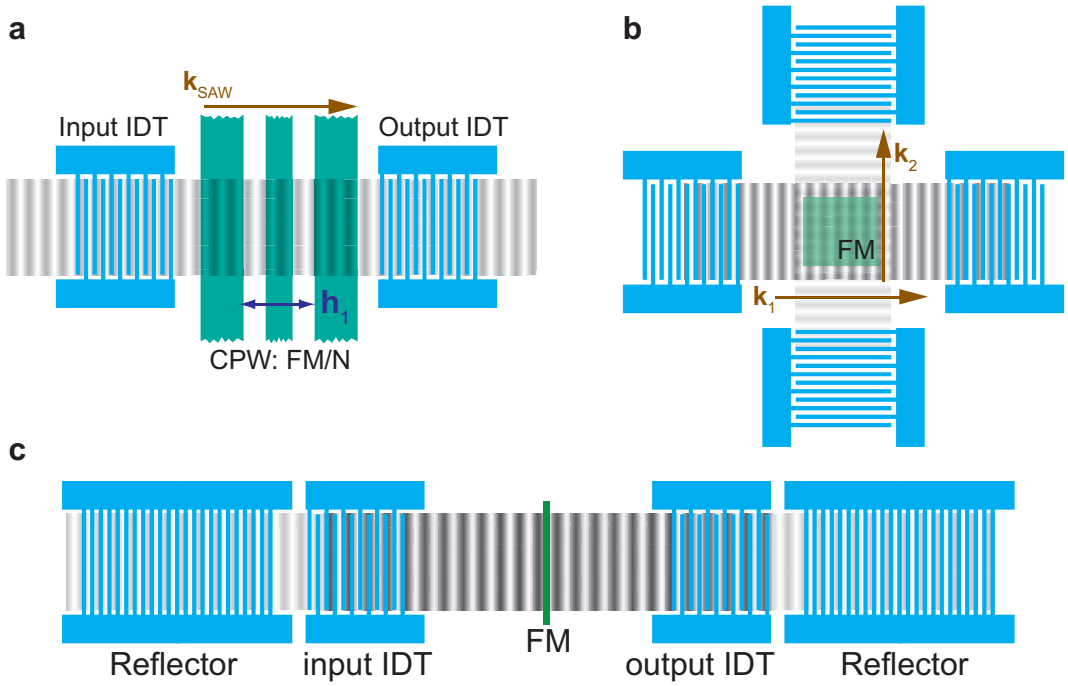

Figure 4.1: **a** Sample illustration featuring a coplanar wave guide (CPW) made of a ferromagnet / normal metal (FM/N) bilayer. **b** Sample design for a four-port SAW dual delay line. **c** Schematic illustration of a SAW resonator loaded with a ferromagnetic strip.

this end, we propose performing SAW magnetotransmission experiments on samples as schematically sketched in Fig. 4.1a and b. In samples where a coplanar wave guide (CPW) made of a ferromagnetic thin film / normal metal bilayer is positioned within the SAW propagation path (cf. Fig. 4.1a), FMR can be excited in two ways. One may either use the virtual magnetoelastic driving field from the SAW or the Oersted field $\boldsymbol{h}_1$ stemming from a rf current through the center line of the CPW to drive FMR. In the configuration shown in Fig. 4.1a, $\boldsymbol{k}_{\mathrm{SAW}} \parallel \boldsymbol{h}_1$. Let us assume that a static external magnetic field $\boldsymbol{H}$ is applied perpendicular to $\boldsymbol{h}_1$ so that FMR can be driven by the latter. For this orientation of $\boldsymbol{H}$, no acoustic FMR can be driven by the Rayleigh SAW (see Chapter 1 for details). However, FMR can be driven by the rf current through the CPW in a broad range of frequencies [60, 177]. Simultaneously to the excitation of FMR one could now measure the transmission of a SAW through the ferromagnetic thin film. As the SAW velocity and damping depends on the elastic constants of the material it propagates within [45], the SAW transmission should reflect changes in the elastic moduli of the ferromagnetic thin film. In these experiments, the frequency of

the SAW can be either identical or different from that of the rf current in the CPW. It should thus be possible to reveal whether the elastic moduli of a ferromagnet actually change in FMR for a conventional, rf external magnetic field drive. Furthermore, due to the ability to freely tune SAW and $\boldsymbol{h}_1$ frequency, a detailed investigation of the frequency dependence of this effect is possible.

In a complimentary set of experiments, one could employ a sample as depicted in Fig. 4.1b. Here, two acoustic delay lines are arranged orthogonally on one and the same substrate. A ferromagnetic thin film is positioned in the mutual SAW propagation area. One may now acoustically drive and detect FMR by exciting and detecting a SAW with wave vector $\boldsymbol{k}_1$. Simultaneously, one can now determine the transmission of a SAW with wave vector $\boldsymbol{k}_2$ through the ferromagnet. The two SAWs do not need to have the same frequency. Thus, a resonant excitation of the ferromagnet by one SAW and simultaneous non-resonant interaction with the second SAW is possible. By comparing the results obtained in this 4 IDT configuration to those obtained in the IDT-CPW-IDT configuration discussed above, one can investigate whether a magnetoelastic drive is beneficial for a resonant control of elastic properties in ferromagnetic thin films.

We now address another crucial point. The lateral dimensions of the ferromagnetic thin films used in this thesis were much greater than the acoustic wavelength. To study the acoustic FMR in the limit of a homogeneous virtual driving field, one thus needs to reduce the dimensions of the ferromagnet. To attain a sufficiently high signal-to-noise ratio to detect the acoustically driven FMR by means of a SAW transmission measurement, the amplitude of the driving field should then be increased to compensate the degradation of the filling factor. This could be achieved in SAW resonators [178] as schematically sketched in Fig. 4.1c. Here, the use of SAW reflectors can dramatically increase the Q-factor of the resonator. The reflectors can either consist of metal gratings or of grooves in the substrate material. In the literature, unloaded SAW resonator Q-factors up to 30 000 have been reported [179]. Note that already the simple delay line structures used in this thesis act as a poor resonator ($Q \approx 10$), as shown by the observation of a triple transit signal in Chapter 1. In a proper SAW resonator (cf. Fig. 4.1c), the SAW forms a standing wave [44] with wavelength λ. Now, by depositing a ferromagnetic strip with width $w \ll \lambda$ at the position of a standing wave antinode, the magnetoelastic driving field can be greatly enhanced. This should allow for new, intriguing experiments. For instance, one

may reach the limit of strong driving of the FMR [180, 181]. In this regime, the precession cone angle enclosed by the magnetization and the effective magnetic field is greatly enhanced. This in turn should allow for the generation of a large spin current density if ferromagnetic thin film/metal bilayers are studied and may eventually reveal saturation effects in spin pumping experiments to demonstrate the physical limit of the pumped spin current source. Furthermore, the acoustic resonator may provide a viable experimental approach to study a possible anticrossing of strongly coupled [182] elastic and magnetic dispersions [27].

In the experiments discussed so far, SAWs are launched and detected by IDTs. From a fundamental point of view, the SAW is an elastic excitation that manifests itself in lattice displacement. These lattice displacements should be directly observable using laser interferometry. Several approaches for the investigation of SAWs by means of interferometry exist in the literature [183–187]. At the Walther-Meißner-Institut, preliminary work to establish a scanning Michelson interferometer for spatially resolved SAW amplitude measurements has been carried out [188]. Such a setup should allow to quantify the SAW amplitude in, e.g., the SAW resonators discussed above. This will be furthermore helpful in positioning the ferromagnetic thin film strip in either an antinode or node of the standing wave. Moreover, by exploiting the spatial and temporal resolution of the interferometry, one may record the damping of a SAW pulse as it passes through a ferromagnetic thin film (or a series of ferromagnetic strips) in and out of ferromagnetic resonance. This allows to measure the backaction of the FMR on the elastic properties *directly*, i.e., without the additional complications involved by the conversion of the acoustic wave into an electrical signal at the IDT.

SAWs can not only be detected but as well excited optically [189–192]. In this approach, laser pulses are used to induce a time-varying local temperature rise at the surface of a solid. This can be seen as the high-frequency counterpart to the static laser-induced temperature profile discussed in Chapter 3. Due to thermal expansion, the application of laser pulses results in a periodic displacement of surface lattice atoms, so that a SAW is launched. Using a thin film grating on the crystal surface [193], the absorption of the laser power can be spatially modulated. With this approach, SAW frequencies in excess of 10 GHz can be excited [194] with a laser spot diameter which can be much larger than the acoustic wavelength. As this optical drive uses thermal gradients to generate the SAW it should be applicable in virtually

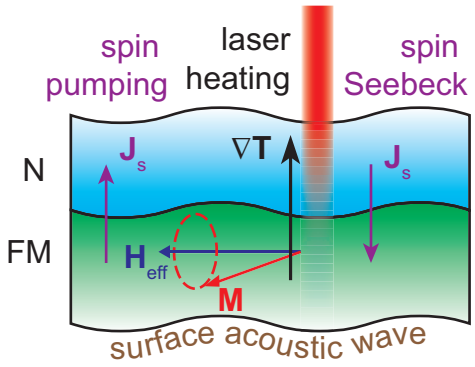

Figure 4.2: A SAW is used for resonant spin current generation by acoustically driven spin pumping in a ferromagnet / normal metal (FM/N) bilayer. Simultaneous laser heating yields a spin current due to the spin Seebeck effect. The net spin current can be detected via the inverse spin Hall effect in N.

any material. This is a very intriguing approach for acoustically driven FMR as it allows for SAW generation in substrates that are *not* piezoelectric. For instance, this approach should allow to excite radio frequency SAWs in epitaxial $Y_3Fe_5O_{12}$ thin films grown on $Gd_3Ga_5O_{12}$ substrates. Such experiments are very appealing for spin pumping, since in the absence of piezoelectricity, the SAW is a purely elastic wave with no electric field component. This simplifies signal analysis as SAW electric field induced microwave rectification effects can be excluded. Optical SAW launching and detection with ultrashort laser pulses furthermore gives access to acoustic pump-probe experiments [195]. On may pump a SAW pulse that magnetoelastically drives a spin wave, the backaction of which on the elastic deformation is probed optically with temporal and spatial resolution.

From our results presented in Chapter 3, we have learned that a spin current can be generated by non-resonant laser heating in ferromagnet/normal metal (FM/N) bilayers. Complimentary, a spin current in such bilayers can be driven by resonantly coupling a SAW to the magnetization precession as shown in Chapter 2. A combination of these two findings is a very intriguing approach to compare resonant and non-resonant phonon-driven spin current generation. In the outlook to Chapter 2, we already proposed to investigate the rf component of the spin current in spin pumping experiments. This rf spin current should be absent in the non-resonant spin Seebeck configuration. By combining spin Seebeck and spin pumping measurements, the dc spin currents arising due to these two effects can be experimentally compared. A possible experimental realization is sketched in Fig. 4.2. The sample introduced in

Chapter 2 is used, but additionally a continuous laser beam induces a vertical temperature gradient in the bilayer (cf. Chapter 3). This should result in the generation of two spin currents, a resonant and a non-resonant one. Using either SAW or laser excitation, one can check the polarization of the SAW driven and thermally driven spin currents (the direction of $\boldsymbol{J}_\mathrm{s} = \boldsymbol{J}_\mathrm{s}^{\uparrow} - \boldsymbol{J}_\mathrm{s}^{\downarrow}$ in Fig. 4.2) by determination of the polarity of the inverse spin Hall effect voltage. Assuming that the two spin currents are oriented antiparallel, the laser-generated spin current should now provide a driving force for magnetization precession by counteracting the damping [84], similar to the spin-torque effect. This should be experimentally observable by determining the linewidth of the acoustically driven FMR with and without additional continuous wave laser heating. The SAW may thereby be generated and detected either by IDTs or by ultrashort laser pulses. Furthermore, the net spin current can be detected via the inverse spin Hall effect in the normal metal. Performing this kind of experiments in insulating ferromagnet/N bilayers is particularly appealing to exclude contributions to the dc voltage in N due to the anomalous Nernst effect. Experiments in this spirit are a promising way to provide insight into the differences and similarities of the off-resonant spin Seebeck effect and the resonant spin pumping for spin current generation.

Taken together, a wealth of new, intriguing experiments related to magnon-phonon-spin-current coupling can be envisaged. By moderate adjustments to the sample design and experimental setups, the concepts established in this thesis can be extended to allow for the direct observation of magnetization and spin current dynamics, access the strong FMR driving regime, and demonstrate a unified model for spin pumping and the spin Seebeck effect.

List of publications

- A. Brandlmaier, S. Geprägs, M. Weiler, A. Boger, M. Opel, H. Huebl, C. Bihler, M. S. Brandt, B. Botters, D. Grundler, R. Gross, and S. T. B. Goennenwein, *In situ manipulation of magnetic anisotropy in magnetite thin films*, Phys. Rev. B **77**, 104445 (2008).

- C. Bihler, M. Althammer, A. Brandlmaier, S. Geprägs, M. Weiler, M. Opel, W. Schoch, W. Limmer, R. Gross, M. S. Brandt, and S. T. B. Goennenwein, *$Ga_{1-x}Mn_xAs$/piezoelectric actuator hybrids: A model system for magnetoelastic magnetization manipulation*, Phys. Rev. B **78**, 045203 (2008).

- M. Weiler, A. Brandlmaier, S. Geprägs, M. Althammer, M. Opel, C. Bihler, H. Huebl, M. S. Brandt, R. Gross, and S. T. B. Goennenwein, *Voltage controlled inversion of magnetic anisotropy in a ferromagnetic thin film at room temperature*, New J. Phys. **11**, 013021 (2009).

- R. Huber, P. Klemm, S. Neusser, B. Botters, A. Wittmann, M. Weiler, S. Goennenwein, C. Heyn, M. Schneider, P. Böni, and D. Grundler, *Advanced techniques for all-electrical spectroscopy on spin caloric phenomena*, Solid State Commun. **150**, 492 (2010).

- M. Kemmler, M. Weides, M. Weiler, M. Opel, S. T. B. Goennenwein, A. S. Vasenko, A. A. Golubov, H. Kohlstedt, D. Koelle, R. Kleiner, and E. Goldobin, *Magnetic interference patterns in 0-π superconductor / insulator / ferromagnet / superconductor Josephson junctions: Effects of asymmetry between 0 and π regions*, Phys. Rev. B **81**, 054522 (2010).

- M. Weiler, F. D. Czeschka, A. Brandlmaier, I.-M. Imort, G. Reiss, A. Thomas, G. Woltersdorf, R. Gross, and S. T. B. Goennenwein, *Magnetic microstructure and magnetotransport in Co_2FeAl Heusler compound thin films*, Appl. Phys. Lett. **98**, 042501 (2011).

- M. Weiler, L. Dreher, C. Heeg, H. Huebl, R. Gross, M. S. Brandt, and S. T. B. Goennenwein, *Elastically Driven Ferromagnetic Resonance in Nickel Thin Films*, Phys. Rev. Lett. **106**, 117601 (2011).

- R. Werner, M. Weiler, A. Y. Petrov, B. A. Davidson, R. Gross, R. Kleiner, S. T. B. Goennenwein, and D. Koelle, *Local tunneling magnetoresistance probed by low-temperature scanning laser microscopy*, Appl. Phys. Lett. **99**, 182513 (2011).

- F. D. Czeschka, L. Dreher, M. S. Brandt, M. Weiler, M. Althammer, I.-M. Imort, G. Reiss, A. Thomas, W. Schoch, W. Limmer, H. Huebl, R. Gross, and S. T. B. Goennenwein, *Scaling Behavior of the Spin Pumping Effect in Ferromagnet-Platinum Bilayers*, Phys. Rev. Lett. **107**, 046601 (2011).

- M. Opel, S. Geprägs, E. P. Menzel, A. Nielsen, D. Reisinger, K.-W. Nielsen, A. Brandlmaier, F. D. Czeschka, M. Althammer, M. Weiler, S. T. B. Goennenwein, J. Simon, M. Svete, W. Yu, S.-M. Hühne, W. Mader, and R. Gross, *Novel multifunctional materials based on oxide thin films and artificial heteroepitaxial multilayers*, Phys. Status Solidi A **208**, 232 (2011).

- A. Brandlmaier, M. Brasse, S. Geprägs, M. Weiler, R. Gross, and S. T. B. Goennenwein, *Magneto-optical imaging of elastic strain-controlled magnetization reorientation*, Eur. Phys. J. B, **85**, 124 (2012).

- M. Weiler, H. Huebl, F. S. Goerg, F. D. Czeschka, R. Gross, and S. T. B. Goennenwein, *Spin pumping with coherent elastic waves*, Phys. Rev. Lett. **108**, 176601 (2012).

- M. Weiler, M. Althammer, F. D. Czeschka, H. Huebl, M. S. Wagner, M. Opel, I.-M. Imort, G. Reiss, A. Thomas, R. Gross, and S. T. B. Goennenwein, *Local charge and spin currents in magnetothermal landscapes*, Phys. Rev. Lett. **108**, 106602 (2012).

Bibliography

[1] A. Volta, Phil. Trans. R. Soc. London **90**, 403 (1800).

[2] G. S. Ohm, *Die galvanische Kette: mathematisch bearbeitet* (T. H. Riemann, Berlin, 1827).

[3] J. C. Maxwell, Phil. Trans. R. Soc. London **155**, 459 (1865).

[4] S. Murakami, N. Nagaosa, and S.-C. Zhang, Science **301**, 1348 (2003).

[5] G. Binasch, P. Grünberg, F. Saurenbach, and W. Zinn, Phys. Rev. B **39**, 4828 (1989).

[6] M. N. Baibich, J. M. Broto, A. Fert, F. N. Van Dau, F. Petroff, P. Etienne, G. Creuzet, A. Friederich, and J. Chazelas, Phys. Rev. Lett. **61**, 2472 (1988).

[7] N. A. Spaldin and M. Fiebig, Science **309**, 391 (2005).

[8] H. Zheng, J. Wang, S. E. Lofland, Z. Ma, L. Mohaddes-Ardabili, T. Zhao, L. Salamanca-Riba, S. R. Shinde, S. B. Ogale, F. Bai, D. Viehland, Y. Jia, D. G. Schlom, M. Wuttig, A. Roytburd, and R. Ramesh, Science **303**, 661 (2004).

[9] W. Eerenstein, M. Wiora, J. L. Prieto, J. F. Scott, and N. D. Mathur, Nat. Mater. **6**, 348 (2007).

[10] A. Brandlmaier, S. Geprägs, M. Weiler, A. Boger, M. Opel, H. Huebl, C. Bihler, M. S. Brandt, B. Botters, D. Grundler, R. Gross, and S. T. B. Goennenwein, Phys. Rev. B **77**, 104445 (2008).

[11] C. Bihler, M. Althammer, A. Brandlmaier, S. Geprägs, M. Weiler, M. Opel, W. Schoch, W. Limmer, R. Gross, M. S. Brandt, and S. T. B. Goennenwein, Phys. Rev. B **78**, 045203 (2008).

[12] A. W. Rushforth, E. De Ranieri, J. Zemen, J. Wunderlich, K. W. Edmonds, C. S. King, E. Ahmad, R. P. Campion, C. T. Foxon, B. L. Gallagher, K. Výborný, J. Kučera, and T. Jungwirth, Phys. Rev. B **78**, 085314 (2008).

[13] M. Weiler, A. Brandlmaier, S. Geprägs, M. Althammer, M. Opel, C. Bihler, H. Huebl, M. S. Brandt, R. Gross, and S. T. B. Goennenwein, New J. Phys. **11**, 013021 (2009).

[14] L. Dreher, T. A. Hilker, A. Brandlmaier, S. T. B. Goennenwein, H. Huebl, M. Stutzmann, and M. S. Brandt, Phys. Rev. Lett. **106**, 037601 (2011).

[15] B. W. Lovett, Physics **4**, 6 (2011).

[16] C. Kittel, Phys. Rev. **73**, 155 (1948).

[17] D. Polder, Philos. Mag. **40**, 99 (1949).

[18] J. H. Van Vleck, Phys. Rev. **78**, 266 (1950).

[19] N. Bloembergen and R. W. Damon, Phys. Rev. **85**, 699 (1952).

[20] R. W. Damon, Rev. Mod. Phys. **25**, 239 (1953).

[21] T. Kasuya and R. C. LeCraw, Phys. Rev. Lett. **6**, 223 (1961).

[22] V. Kambersky, Czech. J. Phys. **26**, 1366 (1976).

[23] R. Naik, C. Kota, J. S. Payson, and G. L. Dunifer, Phys. Rev. B **48**, 1008 (1993).

[24] M. Farle, Rep. Prog. Phys. **61**, 755 (1998).

[25] X. Liu, Y. Sasaki, and J. K. Furdyna, Phys. Rev. B **67**, 205204 (2003).

[26] H. F. Tiersten, J. Math. Phys. **5**, 1298 (1964).

[27] T. Kobayashi, R. C. Barker, J. L. Bleustein, and A. Yelon, Phys. Rev. B **7**, 3273 (1973).

[28] T. Kobayashi, R. C. Barker, and A. Yelon, Phys. Rev. B **7**, 3286 (1973).

[29] P. A. Fedders, Phys. Rev. B **9**, 3835 (1974).

[30] R. F. Wiegert, J. Appl. Phys. **91**, 8231 (2002).

[31] H. Bömmel and K. Dransfeld, Phys. Rev. Lett. **3**, 83 (1959).

[32] A. K. Ganguly, J. Appl. Phys. **47**, 2696 (1976).

[33] I. Feng, M. Tachiki, C. Krischer, and M. Levy, J. Appl. Phys. **53**, 177 (1982).

[34] R. F. Wiegert and M. Levy, J. Appl. Phys. **61**, 4270 (1987).

[35] R. F. Wiegert and M. Levy, IEEE Trans. Magn. **37**, 2708 (2001).

[36] M. Weiler, H. Huebl, F. S. Goerg, F. D. Czeschka, R. Gross, and S. T. B. Goennenwein, Phys. Rev. Lett. **108**, 176601 (2012).

[37] M. Weiler, L. Dreher, C. Heeg, H. Huebl, R. Gross, M. S. Brandt, and S. T. B. Goennenwein, Phys. Rev. Lett. **106**, 117601 (2011).

[38] S. Chikazumi, *Physics of Ferromagnetism* (Oxford University Press, Oxford, 1997), 2nd ed.

[39] J. Fidler and T. Schrefl, J. Phys. D: Appl. Phys. **33**, R135 (2000).

[40] M. J. Pechan, R. L. Compton, D. Bennett, L. C. Chen, C. J. Palmstrom, and S. J. Allen, J. Appl. Phys. **89**, 7514 (2001).

[41] L. Landau and E. M. Lifshitz, Phys. Z. Sowjet. **8**, 153 (1935).

[42] T. Gilbert, IEEE Trans. Magn. **40**, 3443 (2004).

[43] L. Rayleigh, Proc. London Math. Soc. **s1-17**, 4 (1885).

[44] C. Campbell, *Surface Acoustic Wave Devices and Their Signal Processing Applications* (Academic Press, San Diego, 1989), 1st ed.

[45] S. Datta, *Surface Acoustic Wave Devices* (Prentice Hall, Englewood Cliffs, 1986).

[46] D. P. Morgan, *Surface Acoustic Wave Filters* (Academic Press, London, 2007), 2nd ed.

[47] J. H. Collins, Appl. Phys. Lett. **13**, 312 (1968).

[48] H. Söde, *Surface Acoustic Waves at Ferromagnetic-Piezoelectric Interfaces*, Bachelor's thesis, TU München (2009).

[49] F. Goerg, *Herstellung ferroelektrisch/ferromagnetischer Hybridstrukturen*, Bachelor's thesis, TU München (2011).

[50] M. Hiebel, *Grundlagen der vektoriellen Netzwerkanalyse* (Rohde & Schwarz GmbH, Munich, 2006), 1st ed.

[51] K.-Y. Hashimoto, *Surface Acoustic Wave Devices in Telecommunications: Modelling and Simulation* (Springer, Berlin, 2000), 1st ed.

[52] C. Heeg, *Spin Mechanics at Radio Frequencies*, Diploma thesis, TU München (2010).

[53] L. Dreher, M. Weiler, M. Pernpeintner, C. Heeg, H. Huebl, R. Gross, M. S. Brandt, and S. T. B. Goennenwein, *Surface Acoustic Wave Driven Ferromagnetic Resonance in Nickel Thin Films* (2012), in preparation.

[54] W. Robbins, IEEE T. Son. Ultrason. **24**, 339 (1977).

[55] D. Sander, Rep. Prog. Phys. **62**, 809 (1999).

[56] A. J. P. Meyer and G. Asch, J. Appl. Phys. **32**, S330 (1961).

[57] E. Schlömann, Phys. Rev. **182**, 632 (1969).

[58] R. Arias and D. L. Mills, Phys. Rev. B **60**, 7395 (1999).

[59] Z. Frait and H. MacFaden, Phys. Rev. **139**, A1173 (1965).

[60] M. Radlmeier, *Breitbandspektroskopie ferromagnetischer Mikrostrukturen bei tiefen Temperaturen*, Diploma thesis, TU München (2010).

[61] D. D. Stancil and A. Prabhakar, *Spin Waves: Theory and Applications* (Springer, New York, 2009), 1st ed.

[62] R. H. Nelson, J. Appl. Phys. **35**, 808 (1964).

[63] T. D. Rossing, J. Appl. Phys. **34**, 995 (1963).

[64] D. O. Smith, J. Appl. Phys. **29**, 264 (1958).

[65] J. F. Cochran, R. W. Qiao, and B. Heinrich, Phys. Rev. B **39**, 4399 (1989).

[66] M. J. Hurben and C. E. Patton, J. Appl. Phys. **83**, 4344 (1998).

[67] L. R. Bickford, Phys. Rev. **78**, 449 (1950).

[68] J. C. Slonczewski, J. Magn. Magn. Mater. **159**, L1 (1996).

[69] E. B. Myers, D. C. Ralph, J. A. Katine, R. N. Louie, and R. A. Buhrman, Science **285**, 867 (1999).

[70] J. A. Katine, F. J. Albert, R. A. Buhrman, E. B. Myers, and D. C. Ralph, Phys. Rev. Lett. **84**, 3149 (2000).

[71] M. D. Stiles and A. Zangwill, Phys. Rev. B **66**, 014407 (2002).

[72] S. Zhang, P. M. Levy, and A. Fert, Phys. Rev. Lett. **88**, 236601 (2002).

[73] G. Cambon, A. Saïssy, and M. Rouzeyre, J. Appl. Phys. **47**, 4800 (1976).

[74] A. A. Kovalev, G. E. W. Bauer, and A. Brataas, Phys. Rev. Lett. **94**, 167201 (2005).

[75] O. Mosendz, J. E. Pearson, F. Y. Fradin, G. E. W. Bauer, S. D. Bader, and A. Hoffmann, Phys. Rev. Lett. **104**, 046601 (2010).

[76] Y. Kajiwara, K. Harii, S. Takahashi, J. Ohe, K. Uchida, M. Mizuguchi, H. Umezawa, H. Kawai, K. Ando, K. Takanashi, S. Maekawa, and E. Saitoh, Nature **464**, 262 (2010).

[77] K. Uchida, J. Xiao, H. Adachi, J. Ohe, S. Takahashi, J. Ieda, T. Ota, Y. Kajiwara, H. Umezawa, H. Kawai, G. E. W. Bauer, S. Maekawa, and E. Saitoh, Nat. Mater. **9**, 894 (2010).

[78] P. Sharma, Science **307**, 531 (2005).

[79] S. Takahashi and S. Maekawa, Sci. Tech. Adv. Mater. **9**, 014105 (2008).

[80] K. Ando, S. Takahashi, J. Ieda, Y. Kajiwara, H. Nakayama, T. Yoshino, K. Harii, Y. Fujikawa, M. Matsuo, S. Maekawa, and E. Saitoh, J. Appl. Phys. **109**, 103913 (2011).

[81] Y. K. Kato, R. C. Myers, A. C. Gossard, and D. D. Awschalom, Science **306**, 1910 (2004).

[82] V. Sih, W. H. Lau, R. C. Myers, V. R. Horowitz, A. C. Gossard, and D. D. Awschalom, Phys. Rev. Lett. **97**, 096605 (2006).

[83] R. Urban, G. Woltersdorf, and B. Heinrich, Phys. Rev. Lett. **87**, 217204 (2001).

[84] Y. Tserkovnyak, A. Brataas, and G. E. W. Bauer, Phys. Rev. Lett. **88**, 117601 (2002).

[85] Y. Tserkovnyak, A. Brataas, and G. E. W. Bauer, Phys. Rev. B **66**, 224403 (2002).

[86] M. V. Costache, M. Sladkov, S. M. Watts, C. H. van der Wal, and B. J. van Wees, Phys. Rev. Lett. **97**, 216603 (2006).

[87] F. D. Czeschka, L. Dreher, M. S. Brandt, M. Weiler, M. Althammer, I.-M. Imort, G. Reiss, A. Thomas, W. Schoch, W. Limmer, H. Huebl, R. Gross, and S. T. B. Goennenwein, Phys. Rev. Lett. **107**, 046601 (2011).

[88] B. Heinrich, C. Burrowes, E. Montoya, B. Kardasz, E. Girt, Y.-Y. Song, Y. Sun, and M. Wu, Phys. Rev. Lett. **107**, 066604 (2011).

[89] K. Uchida, S. Takahashi, K. Harii, J. Ieda, W. Koshibae, K. Ando, S. Maekawa, and E. Saitoh, Nature **455**, 778 (2008).

[90] K. Uchida, H. Adachi, T. An, T. Ota, M. Toda, B. Hillebrands, S. Maekawa, and E. Saitoh, Nat. Mater. **10**, 737 (2011).

[91] K. Uchida, T. An, Y. Kajiwara, M. Toda, and E. Saitoh, Appl. Phys. Lett. **99**, 212501 (2011).

[92] J. E. Hirsch, Phys. Rev. Lett. **83**, 1834 (1999).

[93] E. Saitoh, M. Ueda, H. Miyajima, and G. Tatara, Appl. Phys. Lett. **88**, 182509 (2006).

[94] G. E. Bauer and Y. Tserkovnyak, Physics **4**, 40 (2011).

[95] S. I. Kiselev, J. C. Sankey, I. N. Krivorotov, N. C. Emley, R. J. Schoelkopf, R. A. Buhrman, and D. C. Ralph, Nature **425**, 380 (2003).

[96] Y. Ji, C. L. Chien, and M. D. Stiles, Phys. Rev. Lett. **90**, 106601 (2003).

[97] K. Ando, S. Takahashi, K. Harii, K. Sasage, J. Ieda, S. Maekawa, and E. Saitoh, Phys. Rev. Lett. **101**, 036601 (2008).

[98] M. Dyakonov and V. Perel, JETP Lett. **13**, 467 (1971).

[99] M. I. Dyakonov, *Spin Physics in Semiconductors* (Springer, Berlin, 2008).

[100] T. Dietl, D. Awschalom, M. Kaminska, and H. Ohno, *Spintronics* (Academic Press, Amsterdam, 2008).

[101] S. Maekawa, *Concepts in Spin Electronics* (Oxford University Press, New York, 2006).

[102] R. Winkler, *Spin-orbit Coupling Effects in Two-Dimensional Electron and Hole Systems* (Springer, Berlin, 2003), 1st ed.

[103] N. F. Mott, Proc. R. Soc. Lond. A **124**, 425 (1929).

[104] L. Berger, Phys. Rev. B **2**, 4559 (1970).

[105] R. Karplus and J. M. Luttinger, Phys. Rev. **95**, 1154 (1954).

[106] J. M. Luttinger, Phys. Rev. **112**, 739 (1958).

[107] F. D. Czeschka, *Spin Currents in Metallic Nanostructures*, Ph.D. thesis, TU München (2011).

[108] H. Y. Inoue, K. Harii, K. Ando, K. Sasage, and E. Saitoh, J. Appl. Phys. **102**, 083915 (2007).

[109] Y. S. Gui, N. Mecking, X. Zhou, G. Williams, and C.-M. Hu, Phys. Rev. Lett. **98**, 107602 (2007).

[110] X. F. Zhu, M. Harder, J. Tayler, A. Wirthmann, B. Zhang, W. Lu, Y. S. Gui, and C. Hu, Phys. Rev. B **83**, 140402 (2011).

[111] P. H. Carr and A. J. Slobodnik, Jr., J. Appl. Phys. **38**, 5153 (1967).

[112] A. Yamaguchi, H. Miyajima, T. Ono, Y. Suzuki, S. Yuasa, A. Tulapurkar, and Y. Nakatani, Appl. Phys. Lett. **90**, 182507 (2007).

[113] L. H. Bai, Y. S. Gui, A. Wirthmann, E. Recksiedler, N. Mecking, C. Hu, Z. H. Chen, and S. C. Shen, Appl. Phys. Lett. **92**, 032504 (2008).

[114] W. Gil, D. Görlitz, M. Horisberger, and J. Kötzler, Phys. Rev. B **72**, 134401 (2005).

[115] T. Gutjahr-Löser, D. Sander, and J. Kirschner, J. Magn. Magn. Mater. **220**, 1 (2000).

[116] M. Nishikawa, E. Kita, T. Erata, and A. Tasaki, J. Magn. Magn. Mater. **126**, 303 (1993).

[117] R. L. Comstock, Proceedings of the IEEE **53**, 1508 (1965).

[118] T. Seebeck, Abh. K. Akad. Wiss. Berlin pp. 265–373 (1823).

[119] W. Nernst, Annalen der Physik **267**, 760 (1887).

[120] M. Weiler, M. Althammer, F. D. Czeschka, H. Huebl, M. S. Wagner, M. Opel, I.-M. Imort, G. Reiss, A. Thomas, R. Gross, and S. T. B. Goennenwein, Phys. Rev. Lett. **108**, 106602 (2012).

[121] R. Myers and J. Heremans, Physics **5**, 29 (2012).

[122] T. Harman and J. M. Honig, *Thermoelectric and Thermomagnetic Effects and Applications* (McGraw-Hill, New York, 1967).

[123] R. Gross, Einführung in die Festkörperphysik, unpublished.

[124] L. Onsager, Phys. Rev. **37**, 405 (1931).

[125] L. Onsager, Phys. Rev. **38**, 2265 (1931).

[126] E. Kondorsk, R. Vasileva, Y. Arkhipov, and A. Cheremus, JETP Lett. **10**, 49 (1969).

[127] A. Asamitsu, T. Miyasato, N. Abe, T. Fujii, Y. Onose, S. Onoda, N. Nagaosa, and Y. Tokura, J. Magn. Magn. Mater. **310**, 2000 (2007).

[128] R. Vasil'eva, Phys. of Metals and Metallography **90**, 27 (2000).

[129] T. Miyasato, N. Abe, T. Fujii, A. Asamitsu, S. Onoda, Y. Onose, N. Nagaosa, and Y. Tokura, Phys. Rev. Lett. **99**, 086602 (2007).

[130] R. P. Vasil'eva and B. Akmuradov, Russ. Phys. J. **15**, 814 (1972).

[131] R. Suryanarayanan, V. Gasumyants, and N. Ageev, Phys. Rev. B **59**, R9019 (1999).

[132] W.-L. Lee, S. Watauchi, V. L. Miller, R. J. Cava, and N. P. Ong, Phys. Rev. Lett. **93**, 226601 (2004).

[133] N. Hanasaki, K. Sano, Y. Onose, T. Ohtsuka, S. Iguchi, I. Kézsmárki, S. Miyasaka, S. Onoda, N. Nagaosa, and Y. Tokura, Phys. Rev. Lett. **100**, 106601 (2008).

[134] Y. Pu, D. Chiba, F. Matsukura, H. Ohno, and J. Shi, Phys. Rev. Lett. **101**, 117208 (2008).

[135] K. Uchida, H. Adachi, T. Ota, H. Nakayama, S. Maekawa, and E. Saitoh, Appl. Phys. Lett. **97**, 172505 (2010).

[136] S. Bosu, Y. Sakuraba, K. Uchida, K. Saito, T. Ota, E. Saitoh, and K. Takanashi, Phys. Rev. B **83**, 224401 (2011).

[137] C. M. Jaworski, J. Yang, S. Mack, D. D. Awschalom, J. P. Heremans, and R. C. Myers, Nat. Mater. **9**, 898 (2010).

[138] L. Gravier, S. Serrano-Guisan, and J.-P. Ansermet, J. Appl. Phys. **97**, 10C501 (2005).

[139] L. Gravier, S. Serrano-Guisan, F. Reuse, and J.-P. Ansermet, Phys. Rev. B **73**, 024419 (2006).

[140] J. C. Slonczewski, Phys. Rev. B **82**, 054403 (2010).

[141] H. Yu, S. Granville, D. P. Yu, and J.-P. Ansermet, Phys. Rev. Lett. **104**, 146601 (2010).

[142] A. Slachter, F. L. Bakker, J. Adam, and B. J. van Wees, Nat. Phys. **6**, 879 (2010).

[143] J.-C. Le Breton, S. Sharma, H. Saito, S. Yuasa, and R. Jansen, Nature **475**, 82 (2011).

[144] M. Weiler, F. D. Czeschka, A. Brandlmaier, I.-M. Imort, G. Reiss, A. Thomas, G. Woltersdorf, R. Gross, and S. T. B. Goennenwein, Appl. Phys. Lett. **98**, 042501 (2011).

[145] M. Reichling and H. Grönbeck, J. Appl. Phys. **75**, 1914 (1994).

[146] R. P. Huebener and A. Seher, Phys. Rev. **181**, 701 (1969).

[147] R. P. Huebener and A. Seher, Phys. Rev. **181**, 710 (1969).

[148] V. A. Rowe and R. P. Huebener, Phys. Rev. **185**, 666 (1969).

[149] M. Zeh, H.-C. Ri, F. Kober, R. P. Huebener, A. V. Ustinov, J. Mannhart, R. Gross, and A. Gupta, Phys. Rev. Lett. **64**, 3195 (1990).

[150] Y. Wang, N. P. Ong, Z. A. Xu, T. Kakeshita, S. Uchida, D. A. Bonn, R. Liang, and W. N. Hardy, Phys. Rev. Lett. **88**, 257003 (2002).

[151] R. Bel, K. Behnia, Y. Nakajima, K. Izawa, Y. Matsuda, H. Shishido, R. Settai, and Y. Onuki, Phys. Rev. Lett. **92**, 217002 (2004).

[152] H.-C. Ri, R. Gross, F. Gollnik, A. Beck, R. P. Huebener, P. Wagner, and H. Adrian, Phys. Rev. B **50**, 3312 (1994).

[153] F. Wilhelm, P. Poulopoulos, G. Ceballos, H. Wende, K. Baberschke, P. Srivastava, D. Benea, H. Ebert, M. Angelakeris, N. K. Flevaris, D. Niarchos, A. Rogalev, and N. B. Brookes, Phys. Rev. Lett. **85**, 413 (2000).

[154] W. Limmer, M. Glunk, J. Daeubler, T. Hummel, W. Schoch, R. Sauer, C. Bihler, H. Huebl, M. S. Brandt, and S. T. B. Goennenwein, Phys. Rev. B **74**, 205205 (2006).

[155] C. Meola and G. M. Carlomagno, Meas. Sci. Technol. **15**, R27 (2004).

[156] E. D. Palik, editor, *Handbook of Optical Constants of Solids* (Academic Press, San Diego, 1985), 5th ed.

[157] C. Kittel, *Introduction to Solid State Physics* (Wiley, New York, 1995), 7th ed.

[158] G. A. Slack and D. W. Oliver, Phys. Rev. B **4**, 592 (1971).

[159] E. W. Slocum, editor, *Tables of thermal properties of gases* (National Bureau of Standards, Washington, 1956), 1st ed.

[160] N. B. Vargaftik, *Handbook of Thermal Conductivity of Liquids and Gases* (CRC Press, Boca Raton, 1993), 1st ed.

[161] T. Farrell and D. Greig, J. Phys. C: Solid State Phys. **2**, 1465 (1969).

[162] K. Itatani, T. Tsujimoto, and A. Kishimoto, J. Eur. Ceram. Soc. **26**, 639 (2006).

[163] D. R. Lide, editor, *CRC Handbook of Chemistry and Physics* (CRC Press, Boca Raton, 2003), 84th ed.

[164] H. Watanabe, Thermochim. Acta **218**, 365 (1993).

[165] A. W. Smith, Phys. Rev. (Series I) **33**, 295 (1911).

[166] A. D. Avery, R. Sultan, D. Bassett, D. Wei, and B. L. Zink, Phys. Rev. B **83**, 100401 (2011).

[167] F. Meier, S. Lounis, J. Wiebe, L. Zhou, S. Heers, P. Mavropoulos, P. H. Dederichs, S. Blügel, and R. Wiesendanger, Phys. Rev. B **83**, 075407 (2011).

[168] T. R. McGuire and R. I. Potter, IEEE Trans. Magn. **11**, 1018 (1975).

[169] R. Lück and T. Ricker, phys. status solidi (b) **7**, 817 (1964).

[170] J. Kerr, Philos. Mag. **3**, 321 (1877).

[171] Z. J. Yang and M. R. Scheinfein, J. Appl. Phys. **74**, 6810 (1993).

[172] R. Gross and D. Koelle, Rep. Prog. Phys. **57**, 651 (1994).

[173] M. Wagenknecht, H. Eitel, T. Nachtrab, J. B. Philipp, R. Gross, R. Kleiner, and D. Koelle, Phys. Rev. Lett. **96**, 047203 (2006).

[174] R. Werner, M. Weiler, A. Y. Petrov, B. A. Davidson, R. Gross, R. Kleiner, S. T. B. Goennenwein, and D. Koelle, Appl. Phys. Lett. **99**, 182513 (2011).

[175] S. Y. Huang, W. G. Wang, S. F. Lee, J. Kwo, and C. L. Chien, Phys. Rev. Lett. **107**, 216604 (2011).

[176] V. Okulov, E. Pamyatnykh, V. Slovikovskaya, and V. Ustinov, J. Magn. Magn. Mater. **198-199**, 608 (1999).

[177] C. Bilzer, T. Devolder, P. Crozat, C. Chappert, S. Cardoso, and P. P. Freitas, J. Appl. Phys. **101**, 074505 (2007).

[178] J. Bell, D.L.T. and R. Li, Proc. IEEE **64**, 711 (1976).

[179] R. C. M. Li, Applied Physics Letters **31**, 407 (1977).

[180] H. Suhl, J. Phys. Chem. Solids **1**, 209 (1957).

[181] M. V. Costache, S. M. Watts, M. Sladkov, C. H. van der Wal, and B. J. van Wees, Appl. Phys. Lett. **89**, 232115 (2006).

[182] S. Gröblacher, K. Hammerer, M. R. Vanner, and M. Aspelmeyer, Nature **460**, 724 (2009).

[183] A. Holm, R. Weigel, P. Russer, and W. Ruile, *IEEE MTT-S International Microwave Symposium Digest*, vol. 3, 1541 –1544 (1996).

[184] J. V. Knuuttila, P. T. Tikka, and M. M. Salomaa, Opt. Lett. **25**, 613 (2000).

[185] J. E. Graebner, B. P. Barber, P. L. Gammel, D. S. Greywall, and S. Gopani, Appl. Phys. Lett. **78**, 159 (2001).

[186] K. Kokkonen, J. Knuuttila, V. Plessky, and M. Salomaa, *IEEE Symposium on Ultrasonics*, vol. 2, 1145–1148 (2003).

[187] O. Holmgren, J. V. Knuuttila, T. Makkonen, K. Kokkonen, V. P. Plessky, W. Steichen, M. Solal, and M. M. Salomaa, Appl. Phys. Lett. **86**, 024101 (2005).

[188] R. Holländer, *Spatially Resolved Investigation of Nano-Mechanical Objects*, Bachelor's thesis, TU München (2011).

[189] R. E. Lee and R. M. White, Appl. Phys. Lett. **12**, 12 (1968).

[190] C. Thomsen, H. T. Grahn, H. J. Maris, and J. Tauc, Phys. Rev. B **34**, 4129 (1986).

[191] A. Neubrand and P. Hess, J. Appl. Phys. **71**, 227 (1992).

[192] J. A. Rogers, A. A. Maznev, M. J. Banet, and K. A. Nelson, Annu. Rev. Mater. Sci. **30**, 117 (2000).

[193] B. Bonello, A. Ajinou, V. Richard, P. Djemia, and S. M. Chérif, J. Acoust. Soc. Am. **110**, 1943 (2001).

[194] D. H. Hurley and K. L. Telschow, Phys. Rev. B **66**, 153301 (2002).

[195] C. Giannetti, B. Revaz, F. Banfi, M. Montagnese, G. Ferrini, F. Cilento, S. Maccalli, P. Vavassori, G. Oliviero, E. Bontempi, L. E. Depero, V. Metlushko, and F. Parmigiani, Phys. Rev. B **76**, 125413 (2007).

Acknowledgment

This thesis was only possible with the amicable and professional support of numerous friends and colleagues. I am particularly grateful towards:

- Prof. Dr. Rudolf Gross, for giving me the opportunity to work at the Walther-Meißner-Institut and for sharing his broad knowledge. For all the support and freedom of choice that I experienced at all times at the WMI.
- Dr. Sebastian T. B. Goennenwein, for a great number of great ideas, most of which worked great. For his enthusiastic and profound contributions to countless discussions of new measurement ideas as well as the obtained results. For being a fantastic supervisor in every respect. For his valuable comments on all manuscripts and my thesis.
- Dr. Hans Hübl, for sharing a wealth of high-frequency knowledge and equipment. For conceiving several successful measurement schemes, taking part in writing manuscripts and for numerous fruitful discussions.
- Prof. Dr. Martin S. Brandt, for several discussions and campus-tales in the course of the Walt(h)er seminar and for his valuable contributions to the analysis of measurements results and manuscripts.
- Lukas Dreher, for all the headaches that his models for acoustically driven FMR cured and caused. For the countless hours we spent with fitting the simulations to our data (or vice-versa) and the physical insight that I gained in that process.
- Matthias Althammer, for being a great roommate and friend in good times and bad (Light Hall effect) and for preparing state-of-the-art YIG samples.
- Dr. Matthias Opel, for his cheerful nature and his contributions to the preparation of manuscripts.

- Prof. Dr. Dirk Grundler and Rupert Huber for stimulating discussions.
- All members of the Magnetiker group for their support, inspiring discussions and helping hands.
- The diploma and bachelor students Christian Heeg, Hajo Söde, Martin Wagner, Frederik Görg, Michael Schreier and Matthias Pernpeintner, for their indispensable contributions to this thesis in form of sample preparation, measurements and simulations.
- Elisabeth Hoffmann, Matthias Althammer, Zolli, Franz Czeschka, Hans-Martin Eiter and Johannes Büttner for keeping up the tradition of the Freitagsbier and the good times we had inside and outside the WMI.
- Inga-Mareen Imort, Dr. Andy Thomas and Prof. Dr. Günter Reiss from Bielefeld University for preparing the Heusler samples.
- Dr. Georg Woltersdorf, for sharing his deep physical understanding in several discussions.
- Ludwig Ossiander and Emel Dönertas for helping me out with all administrative issues.
- Thomas Brenninger as well as Robert Müller and all other members of the mechanical workshop for designing and fabricating all those indispensable parts of my experimental setups.
- Wilhelm Holderied, for being a good friend and for setting back all his pressing issues.
- Astrid, Reto and Simon, the best imaginable family, for their unlimited support and the little, but great time we spend together.
- Susann, for her love and support and for being a constant source of joy.